



**SAPIENZA**  
UNIVERSITÀ DI ROMA

**Univeristà degli Studi di Roma "La Sapienza" Corso di Dottorato in Fisica XXVI ciclo**

**Scanning Probe Microscopies for the Study at Nanoscale of  
Nanomaterials and Nanosystems:  
Magnetic Properties for Bio-applications**

**Candidato**

Chunhua Dong

**Relatore**

Marco Rossi

**Correlatore**

Daniele Passeri

**Anno Accademico 2013/10**

## **List of Figures**

## **List of Tables**

## **Introduction**

### **1 Magnetic Nanomaterials**

- 1.1 General Properties of Magnetic Materials
- 1.2 Magnetic Nanoparticles
  - 1.2.1 Basics of Nanomagnetism
  - 1.2.2 Classification of Magnetic Nanoparticles
  - 1.2.3 Characteristics of Magnetic Nanoparticles
- 1.3 Biomedical Application of Magnetic Nanoparticles

### **2 Magnetic Force Microscopy**

- 2.1 Background of Magnetic Force Microscopy
- 2.2 Principle of Operation of Magnetic Force Microscope
  - 2.2.1 Theory of Magnetic Force Microscopy
  - 2.2.2 Magnetic Interaction between Tip and Nanoparticles
  - 2.2.3 Operation of Magnetic Force Microscopy
- 2.3 Research Progress of Magnetic Force Microscopy

### **3 Magnetic Force Microscopy for Soft Thin Films**

- 3.1 Introduction
- 3.2 Materials and Methods
  - 3.2.1 Equipments
  - 3.2.2 Sample Preparation
  - 3.2.3 Technique Theory

### 3.3 Results and Discussion

#### 3.3.1 Analysis of the Substrates

#### 3.3.2 Thickness Measurement

#### 3.3.3 Further Consideration

### 3.4 Conclusion

## **4 Magnetic Force Microscopy for Vesicular Systems**

### 4.1 Introduction

### 4.2 Materials

### 4.3 Magnetic Force Microscopy of Magnetic Nanoparticles

### 4.4 Magnetic Force Microscopy of Niosomes

#### 4.4.1 Dynamic Light Scattering

#### 4.4.2 Entrapment Efficiency Measurement

#### 4.4.3 Transmission Electron Microscopy

#### 4.4.4 Magnetic Force Microscope Imaging Analysis

### 4.5 Quantification of MNPs into Niosomes

### 4.6 Conclusion

## **5 Magnetic Force Microscopy for Materials of Biological Interest**

### 5.1 Introduction

### 5.2 Investigated Nanomaterials

### 5.3 Equipment

### 5.4 Magnetic Force Microscopy Imaging of Biological Samples

#### 5.4.1 Study of Magnetoferritin

#### 5.4.2 Analysis of Fe<sub>3</sub>O<sub>4</sub>-APTES Nanoparticles

#### 5.4.3 Study of Leukocytes Labeled with Fe@Au Nanoparticles

#### 5.4.4 Study of CCRF-CEM Cells Labeled with Fe<sub>3</sub>O<sub>4</sub>@Cu@Au Nanoparticles

## 5.5 Conclusion

# Conclusion & Outlook

## Publications

A.1 Thickness measurement of soft thin films on periodically patterned magnetic substrates by phase difference magnetic force microscopy (*accepted by Ultramicroscopy, ULTRAM-D-13-00005R2*)

A.2 Visualization and quantification of magnetic nanoparticles into vesicular systems by combined atomic and magnetic force microscopy (in preparation)

A.3 Magnetic force microscopy for biological samples--quantitative issues (in preparation)

A.4 Other works still going on

A.4.1 Quantitative characterization of the magnetic properties of individual magnetic nanoparticles

A.4.2 Further investigation of cellular system labeled with magnetic nanoparticles

A.4.3 MFM Characterization of core-shell magnetic nanoparticles labeled with fluorescence

## Appendix

## References

## Acknowledgment

# List of Figures

**Figure 1.1** M-H curve for ferromagnetic materials and its variations in hysteresis curves towards superparamagnetic behavior (M: magnetization; B: magnetic flux density)

**Figure 2.1** Scheme of magnetic force microscopy

**Figure 2.2** A change of the magnetic force on the tip results in a change in resonance frequency of the cantilever, which can be detected in two ways.

**Figure 2.3** Two pass scanning method for MFM

**Figure 2.4** Surface topography image (floppy) with tapping mode obtained in first pass of MFM (left); corresponding magnetic image with lift height mode in second pass of MFM (right)

**Figure 2.5** Tip-sample geometric model

**Figure 3.1** General view of Slover Pro measurement module

**Figure 3.2** Biological thin film production on floppy disk

**Figure 3.3** MFM characterization of floppy disk: (a) surface morphology; (b) magnetic phase contrast image with lift height  $\Delta z = 100$  nm; (c) sections of the line in (b) obtained from the phase images with three different values of  $\Delta z$ ; (d) phase contrast  $\Delta\phi$  of the different distance  $z$  between the tip and magnetic substrate (symbols) together with the corresponding theoretical fit using Eq. (3.6).

**Figure 3.4** MFM characterization of a colony of *S. aureus* on floppy disk (a) topographical image; (b) corresponding magnetic phase image with  $\Delta z = 100$  nm; (c) profiles of the floppy (line A) and of the bacteria (line B) extracted from the magnetic phase image together with the profile of line A and line B extracted from the topographic image ; (d) phase contrast  $\Delta\phi$  of the substrate and of the bacteria ( $\Delta\phi_A$  and  $\Delta\phi_B$ ) for different values of  $z$  (symbols) together with the theoretical fit of  $\Delta\phi_A$  using Eq. (3.6).

**Figure 3.5** MFM characterization of a part of the *S. aureus* colony on floppy (a) detailed topographical image; (b) corresponding phase image with  $\Delta z = 100$  nm; (c) the absolute phase of the points A, B, C, D as a function of  $z$ ; (d) phase contrast as a function of  $z$  (symbols) together with the theoretical fit of  $\Delta\phi_{AB}$  versus  $z$  using Eq. (3.6).

**Figure 3.6** Functional relation between the relative error in the thickness determination  $e_n$  and the tip-substrate distance  $\Delta z + h$  normalized for the decay length  $\xi_0$ , calculated with data in Figure 3.4 - 3.5.

**Figure 4.1** Example of AFM/MFM characterization of SPIO NPs on a Si flat substrate:(a) topographical reconstruction of an area featuring two NPs and (b) height profile of a NP, corresponding to the dashed line in (a), from which the

diameter of the NP ( $d_{NP}$ ) is evaluated; (c) corresponding MFM phase image and (d) phase shift ( $\Delta\phi$ ) profile, corresponding to the dashed line in (c), from which the MFM phase shift of the NP ( $\Delta\phi_{NP}$ ) is evaluated.

**Figure 4.2** Calibration curves from MFM images of SPIO NPs: (a) NPs phase shift ( $\Delta\phi_{NP}$ ) as a function of the NPs diameter ( $d_{NP}$ ) at fixed tip-sample distance  $\Delta z = 100.5$  revealing a linear dependence between  $\Delta\phi_{NP}$  and  $d_{NP}$ ; (b)  $\Delta\phi_{NP}$  as a function of  $\Delta z$  for four NPs with different  $d_{NP}$ ; (c) calibration curve obtained by evaluating the  $\Delta\phi_{NP}=d_{NP}$  ratio from data in (b) as a function of  $\Delta z$ .

**Figure 4.3** TEM images of niosome: left) empty niosome without MNPs; right) niosome containing MNPs

**Figure 4.4** AFM topography (a) and MFM phase shift image (b) of an empty niosome, the latter revealing a small positive phase shift in correspondence of the niosome.

**Figure 4.5** AFM topography (a) and corresponding MFM phase shift image (b) of three vesicular systems (labeled with A, B and C, respectively) encapsulating SPIO NPs, two of them composed by two distinct niosomes (labeled with A1, A2, B1, and B2, respectively). AFM topography (c) and MFM phase shift (d) of one of the B vesicular system.

**Figure 4.6** (a) Sketch illustrating the proposed model for analyzing MFM data: the magnetic nanoparticle (MNP) with diameter  $d_{NP}$  is at the bottom of the vesicle with height  $h_v$ , the image is acquired at lift height  $\Delta h$  and the distance between the tip apex and the top of the MNP is  $\Delta z$ . (b) Family of curves  $\Delta\phi_{NP}$  versus  $\Delta z$  calculated for values of  $d_{NP}$  ranging from 50 to 130 nm. (c) Detail of the region in the dashed rectangle in (b): in correspondence of the measured value of  $\Delta\phi_{NP}$ , two values are obtained on each curve (open circle and open square, respectively). (d) Values of  $\Delta z + \Delta\phi_{NP} = \Delta h + h_v$  versus  $d_{NP}$  calculated in correspondence of  $\Delta\phi_{NP}$  in (b): the arrows indicate how the diameter of the NP incorporated into the niosome ( $d_{NP}$ ) is inferred from the  $\Delta h + h_v$  measured value.

**Figure 5.1** Cell incubation with magnetic nanoparticles

**Figure 5.2** Schematic representation of the reaction during APTES coating of magnetite nanoparticles

**Figure 5.3** AFM detection with magnetoferritin molecules: (a) Topographical reconstruction of magnetoferritin molecules ( $3 \times 3 \mu m^2$ ); (b) Size histogram of magnetoferritin molecules (data extracted from the topographical image).

**Figure 5.4** AFM topography image (a), standard phase image (b), and MFM phase image (c) of a selected area with certain magnetoferritin molecules ( $2 \times 2 \mu m^2$ ); corresponding further zoom-in area measured with AFM/MFM, reported as AFM topography image (d), standard phase image (e), and MFM phase image (f).

**Figure 5.5** Figure 5.5 MFM images of magnetoferritin molecules for  $\Delta z = 15 \text{ nm}$  (a); histogram of MFM phase shift with Gaussian fit (b); experimental values of the magnetic phase shift for different values of the tip-molecule distance together with the corresponding theoretical fit using Eq. (5.2).

**Figure 5.6** Topographical image of  $Fe_3O_4$ -APTES nanoparticles on Si substrate (a) and the corresponding phase shift image acquired at  $z = 100.5 \text{ nm}$  (b).

**Figure 5.7** Size histogram of  $Fe_3O_4$ -APTES nanoparticles

**Figure 5.8** (a) topographical image of empty cells; (b) corresponding MFM phase shift image of empty cells; (c) topographical reconstruction of an area featuring the cells incubated with Fe@Au nanoparticles; (d) corresponding magnetic phase shift profile ( $20 \times 20 \mu\text{m}^2$ ), in which the MFM phase shift of the cellular system is evaluated.

**Figure 5.9** AFM topography and the corresponding MFM phase shift image of CCRF-CEM cellular system (a) topographical image of empty cells ( $20 \times 20 \mu\text{m}^2$ ); (b) corresponding MFM phase shift image of empty cells; (c) topographical reconstruction of an area featuring the cells surface modified with  $\text{Fe}_3\text{O}_4@\text{Cu}@Au$  nanoparticles ( $20 \times 20 \mu\text{m}^2$ ); (d) corresponding magnetic phase shift profile, in which the MFM phase shift of the cellular system is evaluated.

**Figure 5.10** AFM/MFM characterization of  $\text{Fe}_3\text{O}_4@\text{Cu}@Au$  nanoparticles on a Si flat substrate: (a) topographical reconstruction of an area featuring certain nanoparticles; (b) the corresponding MFM phase image.

**Figure 5.11** Size histogram of  $\text{Fe}_3\text{O}_4@\text{Cu}@Au$  nanoparticles

**Figure 5.12** (a) profiles of dash line in Figure 5.9b and 5.9d extracted from the magnetic phase image together with the profile extracted from the corresponding topographic image; (b) nanoparticles phase shift as a function of the diameter at fixed tip-sample distance  $\Delta z = 100.5 \text{ nm}$  with a linear dependence between them.

# List of Tables

**Table 1.1** General properties of magnetic materials

**Table 1.2** Classification of magnetic nanoparticles

**Table 3.1** Apparatus and parameters

**Table 4.1** Experimentally determined values of the vesicle height ( $h_v$ ) and the phase shift in the magnetic image ( $\Delta\phi_v$ )

with the corresponding calculated values of effective diameter of the incorporated MNPs ( $d_{NP}^{eff}$ ) for the niosomes visualized in Figure 4.4

**Table 5.1** Experimental parameters for the reaction of APTES coating



# Introduction

Magnetic nanomaterials due to their various features different from the ordinary bulk matter in their mechanical, thermal, magnetic, optical properties, are attracting more and more attention in both theoretical research and practical applications in various fields.

Magnetic nanoparticles (MNPs) are a very important branch of magnetic nanomaterials due to their nanoscale sizes, being relatively long *in vivo* half-life and limited agglomeration. These make them ideal for biomedical applications such as magnetic labeling, hyperthermia cancer treatment, targeted drug delivery, and contrast enhancement agents in magnetic resonance imaging (MRI). In drug delivery applications, MNPs can be determined with high accuracy [1]. It would be of interest to localize and characterize MNPs at the nanoscale for biological applications. However, very limited studies exist on detecting and characterizing the magnetic signals of nanoparticles in biological science.

Many methods in surface structure analysis are used as nano-characterization techniques, such as transmission electron microscopy (TEM), scanning electron microscopy (SEM), field electron microscopy (FEM), field ion microscope (FIM), low energy electron diffraction (LEED), Auger electron spectroscopy (AES), photoelectron spectroscopy (ESCA) and electron probe. These techniques detect the surface or interface to show the physical and chemical properties at the nanoscale. But any kind of these techniques has the limitations of one kind or another. For example, LEED and X-ray diffraction method require that the sample has a periodic structure; the resolution of optical microscopy and SEM are insufficient to distinguish surface atoms; high-resolution TEM is mainly used for thin bulk samples and interfacial studies to detect the magnetic properties, but the sample preparation process to get cell sections for TEM analysis is time consuming, and only a small part of cell section can be analyzed; FEM and FIM can only detect the tip radius of less than 100 nm of the atomic structure in two-dimensional geometry. Most commonly, studies which analyze the magnetic nature of MNPs use a superconducting quantum interference device (SQUID) and vibrating sample magnetometer (VSM). But due to low sensitivity and ultimately poor accuracy neither is an

appropriate technique to measure the magnetic moment of individual MNPs, whatever in air or in liquid environment.

Proper characterization and monitoring the properties of MNPs system are important for their potential applications. Currently, one of the most common methods for intracellular imaging of magnetic nanoparticles is fluorescence microscopy [2]. A disadvantage of this technique is that nanoparticles must first be labeled with fluorescent probes in order to be visualized. Due to the inherent limitations, the resolution of optical instruments is restricted by the wavelength of the light [3]. In 2010, Sun *et al.* conjugated fluorescent probes to the surface of magnetic nanoparticles to map cellular uptake pathways [4]. Relative to fluorescence microscopy, two-photon microscopy (TPM) offers improved resolution to study cellular interactions with magnetic nanoparticles, requiring the particles to be labeled with a two-photon fluorescent dye [5]. However it has been known that the imaging depth in TPM cannot be increased indefinitely, meanwhile optimization of the two-photon excitation efficiency is limited by the degree of damage the specimen can tolerate [6]. Due to the relatively poor resolution and reliability of these techniques, scanning probe microscopes (SPM) emerged out. SPM is a generation of scanning tunneling microscope based on a variety of new probe microscopes, such as atomic force microscopy (AFM), lateral force microscopy (LFM) and electrostatic force microscope (EFM). Among these techniques magnetic force microscope (MFM), a label-free *in vitro* detection method for magnetic materials, has the capability to detect nanoscale magnetic domains and simultaneously obtain atomic force microscopy topography images. Due to its ability to localize, characterize and distinguish magnetic materials from other materials at the nanoscale, as well as the advantage of three-dimensional information, MFM offers the great potential for the *in vivo* research.

The scope for MFM lies in detecting the presence of magnetic nanomaterials and spatially localizing magnetic domains. It is likely that magnetic nanomaterials (occur in clusters or aggregates) are embedded in a biological matrix to different depth, and surrounded by bio-molecules. The development and application of MFM for detecting MNPs hold great promise in biology. Spatially localizing magnetic plaques, at nanometer

resolution in ambient atmospheric environment, will provide a better understanding of the deposition mechanism of magnetic material derivatives in the biological tissues.

The background on magnetic materials and nanoparticles is presented in chapter 1 and AFM/MFM experimental apparatus and technique is illustrated in chapter 2. In the last three chapters of the thesis the results of three different typologies of experiments are reported. The studies I have conducted are developed in the framework of the research activities of the laboratory of Scanning Probe Microscopy of EMiNaLab (coordinator prof. Marco Rossi), at the Department of Basic and Applied Sciences for Engineering of Sapienza University of Rome.

In particular, in Chapter 3, we investigate bacterial biofilms at the first time, which are colonies of microbes embedded in a self-produced exopolysaccharides extracellular matrix presenting a major concern in health care. We will demonstrate an approach based on magnetic force microscopy to perform accurate measurement of the thickness of soft thin films - although it may easily extended even to stiff films - deposited on periodically patterned magnetic substrates. By detecting the biofilm thickness MFM will provide a novel method to study the thin film.

In the second part of the thesis, MFM is applied to visualize and quantitatively measure magnetically labeled vesicular system. Vesicles containing magnetic nanoparticles as magnetic target carrier can be used for a wide range of biological application. The encapsulation of drugs in vesicles can minimize drug degradation and inactivation by increasing drug bioavailability and targeting to the pathological area. Many different non-contact techniques have been proposed. Nevertheless, MFM has never been used to study vesicular systems embedding MNPs, either qualitatively or quantitatively. MFM will be illustrated to evaluate the amount of MNPs incorporated in single vesicle, together with discussion on its merits and possible sources of uncertainty.

In the last part of the thesis, we developed the capability of AFM/MFM to detect magnetically labeled materials of biological interest, which are magnetoferritin, APTES functionalized  $\text{Fe}_3\text{O}_4$  nanoparticles and

cells labeled Fe@Au nanoparticle. AFM/MFM will allow us to detect magnetic nanoparticles within submembranes and without severe deformation of samples. In our study, We expect to demonstrate the potential of MFM for the study of magnetic properties of different nano-biosystems, illustrating our approaches which aim at deducing quantitative information from MFM characterizations. Such a research is useful for future applications of MFM, indicating the potential to image magnetic nanoparticles unlabelled and unmodified in living cellular systems.

The overall target of the thesis is to develop and standardize reliable innovative protocols, using scanning probe microscopy-based techniques that could be implemented in rapid and early theranostic methods.

# Chapter 1

## Magnetic Nanomaterials

This chapter provides introduction on magnetic nanomaterials, which are the objects of the magnetic characterization performed in this study. Three aspects are discussed, namely, magnetic materials, magnetic nanoparticles and their biomedical applications.

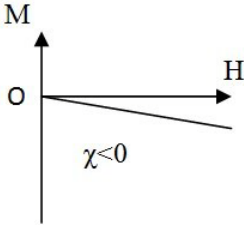
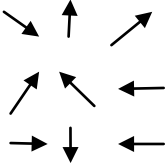
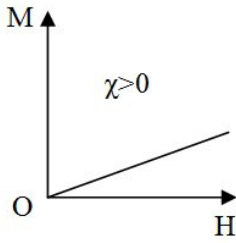
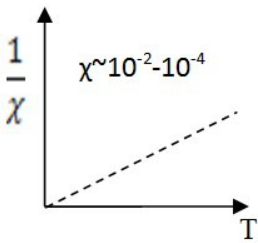
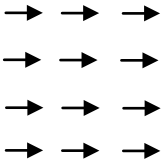
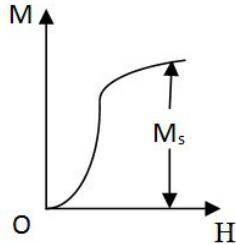
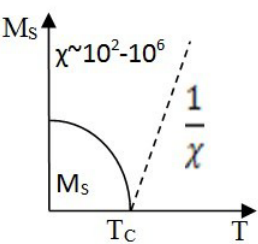
Nanomaterials are significantly different from the corresponding bulk materials, because they exhibit new characteristics (such as increased mechanical strength, chemical reactivity or thermal conductivity). These are mainly due to the large area to volume ratio and quantum effects of nanomaterials. Nanomaterials find applications in a wide number of fields, from optical, electronic, chemical microsystems, as well as in biological systems. Among the wide variety of nanomaterials, magnetic nanomaterials have a wide range of applications. Magnetic nanomaterials are different from the conventional magnetic materials mainly due to the characteristics associated with the physical properties at nanoscale, i.e. single magnetic domains and superparamagnetism.

Before the introduction of magnetic nanomaterials, let us have a look at the basic characteristics of magnetic materials.

### 1.1 General Properties of Magnetic Materials

Magnetic materials, in general, are classified into three types: diamagnetic, paramagnetic and ferromagnetic materials. The first has a diamagnetic magnetic susceptibility  $\chi$  negative and the value is very small in the order of  $10^{-6}$ - $10^{-5}$ . The middle type is characterized by a paramagnetic susceptibility positive and the order is about  $10^{-2}$ - $10^{-4}$ . A relatively small number of substances, ferromagnetic materials, present values of  $\chi$  very high, in the order of tens of thousands.

Table 1.1 General properties of magnetic materials

Classification	Magnetic Moment	M-H Curve	$\frac{1}{\chi}$ $M_s$ , $\frac{1}{\chi}$ curve versus temperature	Typical Materials
Diamagnetism	orbital electron's motion of Larmor gyration		$M_s$ and magnetic susceptibility do not change with temperature.	Cu, Ag, Au C, Si, Ge N, P, As, Sb, Bi S, Te, Se F, Cl, Br He, Ne, Ar, Kr, Xe, Rn etc.
Paramagnetism				Pt, Rh, Pd Li, Na, K Be, Mg, Ca etc.
Ferromagnetism				Fe, Co, Ni, Gd, Tb, Dy FeSi, NiFe, CoFe, SmCo, NdFeB, CoCr, CoPt etc.

M: magnetization;  $M_s$ : saturation magnetization; H: magnetic field strength;  $\chi$ : magnetic susceptibility; T: temperature;  $T_c$ : Curie temperature.

The following briefly introduces the three magnetic properties.

**a) Diamagnetism** - It arises from changes in the orbital motion of the electrons in the presence of an applied magnetic field. An induced magnetic moment is directed anti-parallel to the magnetic field applied, which is known as Larmor precession. In a demagnetized material, the directions of magnetization of the individual domains are all the various possible. All substances have a diamagnetic behavior, since all atoms have electrons belonging to the outer shell that encases the action of an applied magnetic field. The diamagnetic behavior is quantitatively very small, but not masked by other possible effects preponderant. The magnetic susceptibility of

this type of material (diamagnetic susceptibility) is therefore negative, small and being independent of the temperature.

**b) Paramagnetism** - It occurs for a non-zero magnetic moment due to unpaired electrons in partially filled orbital. Paramagnetic materials have a small, positive susceptibility to magnetic fields. These materials are slightly attracted by a magnetic field and the material does not retain the magnetic properties when the external field is removed. Paramagnetic properties are due to the presence of some unpaired electrons, and from the realignment of the electron paths caused by the external magnetic field. Unlike ferromagnets, paramagnets do not retain any magnetization in the absence of an externally applied magnetic field to manifest the rotation of the magnetic moments in the direction of the field. The paramagnetic substances are therefore characterized by a positive susceptibility, such phenomenon is counteracted by thermal agitation which tends to restore the orientation random. Such behavior is summarized in the experimental Curie law. The magnetization of a paramagnetic material, therefore, for field shortly intense and temperatures not very low, grows proportionally with the applied field and tends to a constant value. When in fact all the elementary magnetic moments are aligned with the external field, the magnetization intensity reaches the saturation value and may not further increase. The magnetic susceptibility of this kind of material is therefore paramagnetic positive ( $\chi > 0$ , in the order of  $10^{-2}$ - $10^{-4}$ ) and temperature dependent.

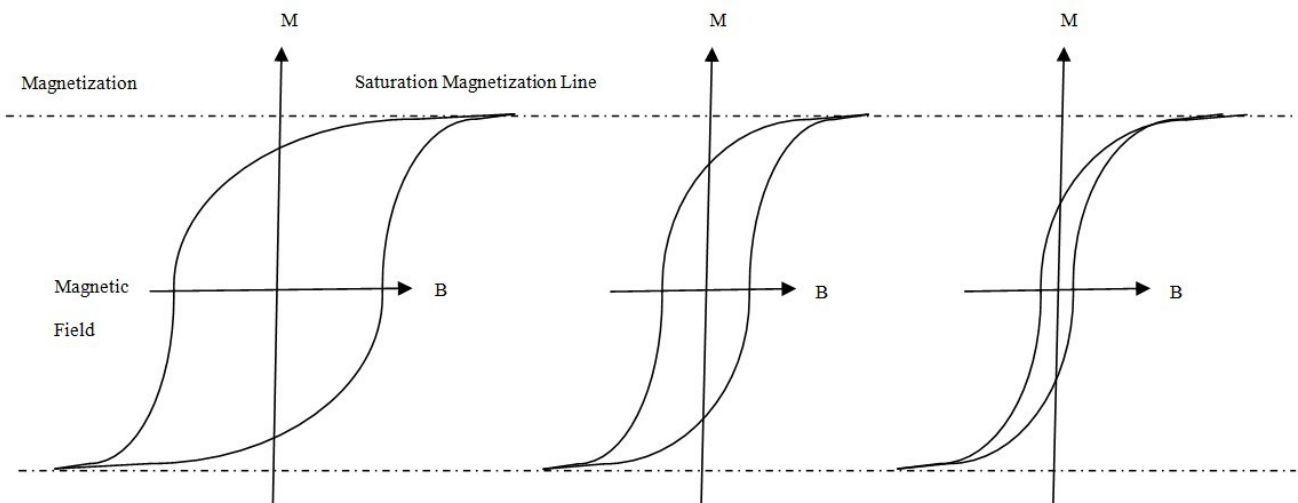


Figure 1.1 M-H curve for ferromagnetic materials and its variations in hysteresis curves towards superparamagnetic

behavior (M: magnetization; B: magnetic flux density)

**c) Ferromagnetism** - Ferromagnetic materials are usually made up of several regions called Weiss domains or regions, spontaneously magnetized. In the absence of an external magnetic field, the individual domains are oriented along directions of easy magnetization; magnetic materials are sorted in fact by magnetocrystalline anisotropy, which is derived from the coupling spin-orbit. The alignment of the dipoles along specific crystallographic directions, defined as "preferential axes of magnetization", is energetically favored over other possible directions of orientation. This property is an intrinsic characteristic of the material.

The spontaneous magnetization within the domains is due to the presence of strong interactions between the atomic moments. These interactions are produced by exchange forces between the electrons and result in an alignment of elementary magnetic moments of the material even in the absence of an applied magnetic field from the outside. The postulation of the interaction between the magnetic moments is due to Weiss, which, in 1907, suggested that such an interaction could be represented by a field of magnetic induction internal  $B_m$ , proportional to the intensity of magnetization, and the hypothesized existence of domains.

The phenomenological theory of Weiss is an explanation in quantum theory, which shows the existence of another type of interactions between the electrons, in particular of electrostatic type, by virtue of their spin. These interactions are called "exchange interaction" and are derived from the limitations imposed by the Pauli exclusion principle in respect of the spins of electrons when the charge distributions associated with the states occupied by two electrons begin to overlap.

The introduction of molecular field postulated by Weiss makes a more generalized version of the Curie law, that is law of Curie-Weiss:  $\chi=C/(T-T_c)$  where the term  $T_c$  indicates the "Curie temperature", which is an intrinsic feature of each substance. This law describes the phenomenon experimentally, that a ferromagnetic material heated to a temperature above the temperature of Curie ( $T > T_c$ ) loses its ferromagnetic properties and behaves as a paramagnet. That happens because the energy of thermal agitation becomes predominant compared to the energy of interaction between the dipoles which facilitates the alignment, thereby producing a random



orientation.

Figure 2.1 shows a first magnetization curve for a sample and the relative polycrystalline ferromagnetic hysteresis loop and its variations towards superparamagnetic behavior. Each region of the curve can be associated with a different process responsible for the growth of the intensity of magnetization and energy loss, whose overall contribution gives rise to hysteresis. In the first section of curve (low values of the applied field) the increase of magnetization is due to the movement of the Bloch walls. These displacements have irreversible character, linked to the fact that the Bloch wall moving. The movement of the wall "barriers to high-energy" is associated with phenomena of dissipation. Therefore it is substantially reversible. The maximum magnetization reached by the material is called saturation magnetization. The increase of magnetization is only due to the process of rotation of dipoles towards the direction of the applied magnetic field. The energy expended is the energy required to overcome the energy barrier magnetocrystalline.

## **1.2 Magnetic Nanoparticles**

### **1.2.1 Basics of Nanomagnetism**

Magnetic nanomaterials have many interesting properties respect to the bulk magnetic materials, such as quantum size effects, small size effects, macroscopic quantum tunneling effect, surface effect, etc.. Magnetic nanoparticles are very attractive among investigated nanomaterial systems, owing to the fact that their magnetic properties dramatically depend upon their size and their shape. Concerning size effects, the magnetic properties of magnetic nanoparticles are dominated by two important features----single domain and superparamagnetic property, both features will be discussed briefly here.

**a) Single-domain Particle** - The microscopic interpretation of magnetic properties lies in the orbital and spin motions of electrons, which are associated with a magnetic moment. The interaction between the atoms causes magnetic order below a certain critical temperature. Bulk materials can be classified on the basis of these interactions and their influence on the materials behavior at different temperatures. In bulk magnetic particles, it is well known that their structures are multidomains in magnetism. The magnetization regions in which all

magnetic moments of the constituent atoms are pinned in the same direction, and are separated by domain walls. The reason for such an arrangement arises from the decreasing of magnetostatic energy of the materials when a large domain is broken up into several smaller domains. The formation of the domain walls is a process driven by the balance between the magnetostatic energy, which increases proportionally to the volume and the domain-wall energy. If the sample size reduced, there is a critical volume. This critical diameter typically lies in the range of a few tens of nanometers and depends on the material. It is influenced by the contribution from various anisotropy energy terms. A single-domain particle is uniformly magnetized with all the spins aligned in the same direction. The magnetization will be reversed by spin rotation since there are no domain walls to move. Consequently, this means that a magnetic nanoparticle with a diameter lower than the size of the possible smallest magnetic domain, could only consist of a single domain, which, in turn, results in a narrowing of the magnetic hysteresis curve compared to the bulk material, also the process is shown in Figure 1.1.

**b) Superparamagnetism** - Superparamagnetism means that the thermal energy may be enough to change the magnetization spontaneously by exceeding the energy barrier in a single domain structure of the magnetic particle. Since superparamagnetic nanoparticles do not have a permanent magnetic moment they will have no hysteresis loop. In a study by Schreiber *et al.* in 2008, the superparamagnetic nature of those magnetic nanoparticles being studied was confirmed and demonstrated by showing that the superparamagnetic nanoparticles could possess a stable dipole moment at room temperature in externally applied magnetic fields on the order of a few hundred gauss [7]. In general, the smaller the size of the magnetic particles is, the lower its transition temperature from ferromagnetic to superparamagnetic behavior will be. A paramagnet with very low net magnetic moment shows even in the absence of an external magnetic field, though a giant magnetic moment develops inside of the particle due to individual atomic magnetic moments. When the particle size decreases, the ambient thermal energy  $k_B T$  can overcome the energy barrier  $K_{\text{eff}} V$  and the magnetization of the particle can be easily flipped [8]. Theoretically, magnetic anisotropy energy  $E(\theta) = K_{\text{eff}} V \sin^2 \theta$ , where  $V$  is the particle volume,  $K_{\text{eff}}$  is the anisotropy constant and  $\theta$  is the angle between the magnetization and the easy axis. The magnetic moment of each magnetic particles can rotate randomly. The lack of magnetization after removal of external

fields maintains the colloidal stability and agglomeration resistance, resulting in its important role in biomedical applications.

### 1.2.2 Classification of Magnetic Nanoparticles

Magnetic nanoparticles are a class of particular magnetic nanomaterial that can be manipulated under the influence of an external magnetic field. Such particles commonly consist of magnetic elements such as iron, nickel and cobalt and their chemical compounds like magnetite ( $\text{Fe}_3\text{O}_4$ ), Maghemite ( $\gamma\text{-Fe}_2\text{O}_3$ ) etc. Magnetic nanoparticles are of great interest for researchers from a wide range of disciplines nowadays. In most cases, the particles range from 1 to 100 nm in size and may display as single domain particles and superparamagnetism, meanwhile the properties in chemical and biological aspects. Depending on the structure of magnetic nanoparticles, they can be classified into four groups, as summarized in Table 1.2.

Table 1.2 Classification of magnetic nanoparticles

Classification	Features	Examples	Application
Magnetic Monometallic Nanoparticles	1) larger magnetization; 2) unstability ( easy to be oxidized ); 3) nanocrystalline ferromagnet is extremely sensitive to its shape.	1) zero valent iron in permeable reactive barrier ; 2) iron nanoparticles; 3) soft magnetic material like Co; 4) six of the nine rare earth elements are ferromagnetic.	1) applied in catalysis and other chemical processes, biology, microelectronics or nanoelectronics; 2) applied ultrahigh density magnetic recording media, exchange coupled nanocomposite magnets, microwave devices, and biomedicines; 3) used in magnetic cooling systems.
Magnetic Oxide Nanoparticles	1) high saturation magnetization; 2) high magnetic susceptibility; 3) low toxicity.	1) nanoscale oxide particles of transition metals; 2) magnetite ( $\text{Fe}_3\text{O}_4$ ) and maghemite ( $\gamma\text{-Fe}_2\text{O}_3$ ).	1) used in magnetic resonance tomography; 2) used in designing ceramic, magnetic, electrochromic and heterogeneous catalytic materials.
Magnetic Alloy Nanoparticles	1) chemical stability and high magnetocrystalline anisotropy; 2) high saturation magnetization and resistance against oxidation.	FePt, FeNi, FeCo, CoCr etc.	1) used as magnetic storage media and permanent magnets; 2) used in high density information storage.
Magnetic Core-shell Nanoparticles	1) enhanced colloidal stability and biocompatibility; 2) higher magnetic moment and surface function.	Fe/ $\text{Fe}_3\text{O}_4$ @Au/Ag; Fe/ $\text{Fe}_3\text{O}_4$ @Si/SiO <sub>2</sub> ; Fe/ $\text{Fe}_3\text{O}_4$ @C	biomedical applications, catalysis, environment protection etc.

**a) Magnetic Monometallic Nanoparticles** - They display optical, electronic, catalytic properties and larger magnetization compared to metal oxides. Recent studies have demonstrated the effect of zero valent iron nanoparticles for the transformation of halogenated organic contaminants and heavy metals. Ferromagnetic nanoparticles with controlled size and shape have potential applications in advanced materials and devices. But there is a very vital disadvantage of monometallic nanoparticles, that is they are not stable in ambient atmospheric condition as well as in liquid environment since of its easy oxidation.

**b) Magnetic Oxide Nanoparticles** - They have extensive applications, such as used as magnetic recording media, catalysts, pigments, gas sensors, optical devices and degenerator of pollution [9-10]. Nanoscale oxide particles of transition metals are gaining continuous importance for various applications these years. Cobalt monoxide has played an important role in the discovery of the exchange shift of the hysteresis curve. Studies of  $\text{Co}_3\text{O}_4$  nanoparticles have been undertaken by a few groups [11-13]. The distribution and resulting contrast of these particles are highly dependent on their synthetic route, shape, and size. Regarding the choice of magnetic particle for biomedical application, the iron oxides magnetite ( $\text{Fe}_3\text{O}_4$ ) and maghemite ( $\gamma\text{-Fe}_2\text{O}_3$ ) are the most studied to date because of their generally appropriate magnetic properties and biological compatibility. Among all iron oxides,  $\text{Fe}_3\text{O}_4$  nanoparticles possess the most interesting properties due to the presence of iron cations in two valence states,  $\text{Fe}^{2+}$  and  $\text{Fe}^{3+}$ , in the inverse spinel structure.  $\text{Fe}_3\text{O}_4$  nanoparticles have attracted much interest not only in the field of magnetic recording media but also in the areas of drug delivery systems, medical applications [14-18]. In 2011, superparamagnetic  $\text{Fe}_3\text{O}_4$  nanoparticles were used as the stabilizer to prepare magnetic pickering emulsions [19].  $\text{Fe}_3\text{O}_4$  nanocrystals confined in mesocellular carbon foam (MSU-F-C) are synthesized by a “host–guest” approach and tested as an anode material for lithium-ion batteries (LIBs) [20]. A report of  $\text{Fe}_3\text{O}_4$  nanoparticles synthesized for application in wastewater purification was demonstrated in 2009 [21]. Its potential application to biomedical field will get more attention in the future research. And with nanocharacterization techniques,  $\text{Fe}_3\text{O}_4$  has been detected by different methods, like transmission electron microscopy (TEM), electron spectroscopy for chemical analysis (ESCA), ultraviolet visible spectroscopy (UV–Vis), and X-ray diffraction (XRD) [22]. However, the characteristics images are not developed enough to

get more information. In this thesis, magnetite  $\text{Fe}_3\text{O}_4$  nanoparticles will be studied by a novel technique----MFM, as will be discussed in the following chapters.

**c) Magnetic Alloy Nanoparticles** - Co or Fe nanoparticles are difficult to obtain because of their sensitivity to oxidation in the atmosphere, which diminishes their magnetic properties. This makes magnetic alloy nanoparticles particularly interesting. Alloy nanoparticles present compositionally ordered structures with two or more metals coaggregate, with properties that differ from those of bulk alloys or nanoparticles of the individual components. Such as the ordered Co–Fe alloys are soft magnetic materials with negligible magnetocrystalline anisotropy. Fe–Ni nanoparticles have a much lower saturation magnetization than the corresponding bulk samples over the whole concentration range.

**d) Magnetic Core–shell Nanoparticles** - They have a special advantage of biocompatibility with functionalized shell. The magnetic core usually is coated with a layer of a nonmagnetic, antiferromagnetic, or ferro/ferri-magnetic shell [23]. The shell has mostly disordered structural, while the core is magnetically ordered. A nonmagnetic coating is used routinely for magnetic core stabilization and surface functionalization for biomedical applications. An antiferromagnetic coating over a ferromagnetic core leads to exchange bias (a shift of the hysteresis loop along the field axis), and improvement in the thermal stability of the core.

The magnetic core usually discussed in reports are Fe (0) and iron oxide in common, synthesized with single shell [24] or mutishell structures [25]. They are coated with different materials from nonmetallic covering [26-31] to metallic shell [32-35]. Core-shell magnetic nanoparticles have a range of attractive properties like optical, microwave absorbing and tunable plasmonic figures and so on, which are very interesting for characterization and biological applications [36-39]. Graphene with  $\text{Fe}_3\text{O}_4$  was studied with different nanoforms like nanosheets [40], nanoparticles [41]. Dumbbell-like Au- $\text{Fe}_3\text{O}_4$  nanoparticles can be used in catalyzing  $\text{H}_2\text{O}_2$  reduction [42] and delivering nanocarriers for highly sensitive diagnostic and therapeutic applications [43]. Besides Fe(0) and iron oxide acting as the magnetic core Nickel and Cobalt were studied too [44-45]. Among these reports, many characterization techniques are adopted such as X-ray diffraction (XRD), scanning electron

microscopy(SEM), field emission SEM (FE-SEM), transmission electron microscopy (TEM), high resolution TEM, Fourier transform infrared spectra (FTIR), thermal gravimetric analysis (TGA), UV–visible absorption and fluorescence emission, X-ray photoelectron spectra (XPS), N<sub>2</sub> adsorption/desorption, photoluminescence (PL) spectra, superconducting quantum interference device (SQUID), electrochemical impedance spectroscopy, cyclic voltammetry, X-ray absorption spectrum (XAS), fluorescent microscopy, confocal laser scanning microscopy (CLSM), atomic force microscopy (AFM). However, there is no characterization with only one method to interpret the characters of core-shell nanoparticles. Core-shell Fe@Au and Fe<sub>3</sub>O<sub>4</sub>@Cu@Au nanoparticles attract more attention since of their unique properties in optics, stability *in vivo* and functionalizable property [46-47]. We expect to explore the capability of magnetic force microscopy in the biological applications with the two types of magnetic nanoparticles, corresponding studies will be shown in the chapter 5.

### 1.2.3 Characteristics of MNPs

The magnetic moment of individual MNPs is difficult to be determined due to low sensitivity and ultimately poor accuracy. Many methods are available to measure MNPs in a colloidal suspension or dry state [48]. Common techniques include dynamic light scattering (DLS), transmission electron microscopy (TEM), analysis of X-ray diffraction (XRD) and extended X-ray absorption of fine structure (EXAFS). Scanning electron microscopy (SEM) is used to characterize the size and morphology of nanoparticle samples [49]. DLS measures the nanoparticle size in suspension with a large range of particle sizes other than the crystallite size in the dry state, showing high sensitivity for the presence of agglomerated particles. XRD is applied to study the crystalline structure of the nanoparticles, which also can be done using Mossbauer spectroscopy [50]. By showing the difference in electron density of the core and shell materials, TEM is the most powerful technique to determine crystallite size in the dry state and provide insight into the core-shell structure of coated MNPs [51]. Typically, surface charge is characterized by zeta potential analysis with a ZetaMaster and Nanosizer [52], being an important parameter in determining the colloidal stability of a suspension of MNPs. Zero field cool and field cool analyses are used to determine the blocking temperature on superparamagnetism. There are still various tools

and techniques, besides MFM, that can be used to determine the magnetic properties of magnetic nanoparticles. Most commonly, studies which analyze the magnetic nature of MNPs use a superconducting quantum interference device (SQUID) to confirm the superparamagnetism. Iron digestion method is demonstrated by measuring mass or aggregated magnetization of colloidal solutions to determine the iron concentration. Atomic force microscopy (AFM) and, by extension, magnetic force microscopy (MFM), are effective in detecting magnetic nanoparticles both physical characteristics and magnetic properties.

### **1.3 Biomedical Application of Magnetic Nanoparticles**

Magnetic nanoparticles could be used as materials for magnetic recording and microwave absorption in industry, as well as the in water treatment and adsorption desulfurization with magnetic nanoparticles for environment protection. Magnetic nanoparticles, by virtue of their size and magnetic characters, lead themselves to a variety of applications. Here we focus on the application for biomedical science. The large surface area of the magnetic nanoparticles, useful for the attachment of extractable species and selected biological molecules, allows for targeting of selected species or for delivery to a selected location in an applied external magnetic field. The conjugation of biological molecules (amino acids, DNA, simple peptides, polysaccharides, lipids) on the surface of magnetic nanoparticles is of certain interest for the design of magnetic markers in biological and medical experiments.

Magnetic nanoparticles offer many attractive possibilities in biomedical application. Nanoparticles with controllable sizes ranging from a few nanometers up to tens of nanometers can be used as tiny probes without biological interference, since of the small dimension like that of virus, protein or gene. Moreover, functional nanoparticles interact with the inside and the surface of biological molecules, providing a new controllable tagging method. Magnetic nanoparticles, being manipulated by an external magnetic gradient with the intrinsic penetrability of magnetic fields into human tissue, open up many applications involving the transport and immobilization of magnetically tagged biological entities, as well as delivery of anticancer drugs to a targeted region of the body. Magnetic nanoparticles, by responding to a time-varying magnetic field, are related to the

transfer of energy from the exciting field to the nanoparticle, such as hyperthermia agents by delivering thermal energy to targeted tumors. These, and many other potential applications, are available in biomedicine as a result of the special properties of magnetic nanoparticles.

**a) Biocompatibility of Magnetic Nanoparticles** - Magnetic nanoparticles, having a very small size and large surface area, can be easily modified thanks to many reactive functional groups (such as carboxy, amino, mercapto, biotin, monoclonal antibodies). This gives magnetic nanoparticles more special properties. In order to interact with biological target, a coating layer acting as a bioinorganic interface should be attached to the nanoparticle. Coatings with antibodies, biopolymers, or monolayers of small molecules can make the nanoparticles biocompatible, providing a link between the nanoparticle and the target site with increased colloidal stability.

**b) Magnetic Separation** - Magnetic separation technology causes very little mechanical stress. On the other hand, it is nonlaborious, not expensive, and often highly scalable. Being used to separate biological important substances, magnetic separation is fundamentally different from centrifugation and filtration, which rely on physical or chemical differences between the entities being separated. Instead, magnetic separation relies on the tagging of these biological entities with MNPs and the subsequent exposure to magnetic fields suitable to automation and miniaturization. Magnetic separation has been successfully applied to many aspects of medical and biological research, showing sensitive selection of rare tumor cells from blood, and efficient separation of low numbers of target cells. For example, the enhanced detection of malarial parasites in blood samples utilizes the magnetic properties of the parasite or labeled red blood cells with a magnetic fluid. Combining with optical sensing magnetic separation has been used to perform magnetic enzyme-linked immunosorbent assays. Magnetic separation has proven to be successful in research as well as therapeutics, mostly due to its high sensitivity and ability to separate a low number of target entities [53]. In 2007 Jing et al. tested immune-magnetically labeled cells from fresh leukocyte fraction of peripheral blood by magneto-phoresis of magnetic nanoparticles [54].



**c) MRI Contrast Enhancement** - Both quantum dots and magnetic nanoparticles can be targeted to tumors, whose MRI images show different magnetic resonance signals under the applied magnetic field. Small superparamagnetic iron oxide nanoparticles (SPIONs) have been developed into nanometer sizes and can be used in real-time MRI and positron emission tomography (PET) for target drug delivery. These SPIONs contrast agents have been commercially available and approved for use with MRI patients [51]. Typically, SPIONs contrast agents shorten the T2 relaxation rates and allow MRI to differentiate between different organs in the body [55]. Due to their high magnetization, SPIONs cause a critical decrease in the relaxation rate of water protons, thus it can be processed by cells using iron metabolism pathways that are safe for patients [56]. The mononuclear phagocyte system attempts to remove SPIONs injected away from circulation through opsonization and phagocytosis by macrophages [57]. SPIONs of approximately 50 nm are opsonized quickly upon being injected into the body during their phagocytosis by macrophages [58]. Ultra-small SPIONs are progressively taken up by macrophages in healthy lymph nodes and consequently are used for MRI of lymph nodes [59]. Core-shell magnetic nanoparticles have shown great potential as MRI contrast agents due to their functional ligandization with target antigens and receptors. SPIONs coated with a silicon oxide (SiO<sub>2</sub>) shell have applications in therapies and have shown relativity values comparable to those of metal, alloy and spinel magnetic nanoparticle contrast agents [60].

**d) Targeted Drug and Gene Delivery** - The magnetic carriers accumulate not only at the desired site but also throughout the cross section from the external source to the depth. Magnetic drug delivery can concentrate the functional nanoparticles at the target under external magnetic fields. Painkillers, vaccines and antiviral pharmaceuticals have their side effects massively reduced with accurate drug localization in blood vessels and in organs. Much lower amounts of drug are targeted magnetically to localized disease sites, being affected by magnetic field strength, gradient and the volumetric properties of the particles, as well as blood flow rate, circulation time, and physiological conditions like tissue depth to the target site. As the magnetic gradient decreases with the distance to the target, magnetic drug delivery can be regulated with the magnetic gradient and the residence time of nanoparticles in the desired area [59]. Permanent Nd-Fe-B magnets in combination with

magnetic nanoparticles can reach magnetic field depths up to 10-15 cm in the body [61]. Besides external magnetic fields, internal magnets can be located near the target by minimally invasive surgery. Tumors have the potential to outgrow their blood supply, resulting in an area of a vascular necrotic tissue at the center that cannot be reached by the cytotoxic drug/carrier complexes in the blood stream. Concerning the interaction between a magnetic implant and magnetic nanoparticles, it has been demonstrated that external magnets in tumor targeting allowed the cytotoxic drug to reach the vascular tissue, after loading the macrophages with iron oxide nanoparticles [62].

**e) Perspectives** - Many products based on magnetic nanoparticles are in their final development stages with several already on the market. The future of magnetic nanoparticle applications involves multifunctional therapeutic materials and the targeting ability to desirable sites. In general, applying magnetic field in the human body can be used to treat the disease without significant side effects and restricting conditions, except for those patients whose body contains magnetizable material such as medical devices with batteries, vascular or intracranial metallic material. The therapeutic potential of magnetism has attracted more attention, i.e. heat treating in hyperthermia has been recognized as a promising approach of cancer therapy, particularly in synergy with chemo- and/or radio-therapy. Targeting malignant tumors selectively and effectively to make an accurate diagnosis when the disease would be still treatable, is of much importance. Nanomedicine-based magnetic contrast agents offers a great opportunity to develop highly sophisticated devices that can overcome many traditional hurdles of contrast agents. In radioisotope imaging ligand-mediated magnetic resonance contrast agents can be designed in particular for tumor diagnosis. Magnetic nanoparticles are now routinely used as contrast agents for the mononuclear phagocyte system (MPS) organs and very soon for lymph nodes. The future developments of magnetic nanoparticles applied into theranostics may focus on active targeting through molecular imaging and cell tracking. Concerning how the human body interacts with magnetic nanoparticles (from killing cancer cells to healing tissues to reducing infection), magnetic nanoparticles for treating a wide range of diseases may be available in the very near future.

## Chapter 2

# Magnetic Force Microscopy

In this chapter, we will introduce an atomic force microscopy (AFM) based technique, magnetic force microscopy, which is usually used for detecting the magnetic structures of a specimen. The magnetic characterization of nanoparticles normally depends on a specific technique. Techniques such as SQUID (Superconducting Quantum Interference Devices) or VSM (Vibrating Sample Magnetometer) allow the detection of very weak magnetic fields and help to determine the magnetic dipole moment of numerous sets of particles. However, these techniques do not allow the detection of the magnetic properties of the individual particles. Magnetic force microscopy (MFM), a type of scanning probe microscopy derived from the atomic force microscopy, detects local nanoscale magnetic interactions by measuring the magnetic probe deflections and images the magnetic field distribution of a sample on nanoscale.

### 2.1 Background of Magnetic Force Microscopy

Magnetic force microscopy is a techniques based on atomic force microscopy, which is a typical scanning probe microscope for measuring the roughness and topography of the surface. The principle of AFM is based on the measurement of the repulsive or attractive interaction force between the tip and the sample surface. The detection system measures the change of cantilever mechanical state and sends to the scanner control system a signal proportional to this change. The control system moves the probe perpendicular to the surface to bring the parameter back to its original value. Simultaneously the probe displacement value is saved in PC memory and interpreted as sample topography. A good spatial resolution is achieved if the atomic force microscope operates in contact mode where the tip contacts the surface of the specimen as it scans at a constant vertical force. In tapping mode, a cantilever on which the tip is mounted oscillates at its resonant frequency in the vicinity of the surface of the samples to reduce the friction force during scanning largely. In non-contact mode, the tip will

leave far from the sample surface, the forces acting on the tip of atomic force microscope are due to different interaction force.

Martin and Wickramasinghe improved this technique as magnetic force microscope in order to investigate magnetic property of the sample surface with submicron 3D resolution [63]. It was proposed to use a microneedle made of ferromagnetic material as a tip for measuring the magnetic force experienced by this micro-magnet in the vicinity of the surface of a magnetic specimen. When the tip is raised above the surface to a certain height, the universal short range van der Waals attraction almost completely vanishes and the tip is mainly affected by long range magnetic forces. The near-field magnetostatic interaction for a typical probe-sample configuration turns out to be fairly strong and largely independent of surface contamination [64].

The technique MFM is a particular mode of non-contact scanning probe microscope, based on the detection mechanical magnetostatic interaction between probe and magnetic sample. The magnetic sample, in fact, interacts through magnetic dipolar interaction with the apex of the tip of the cantilever. The first MFM applications began in the early 90s. Magnetic storage media and recording heads as well as magnetic domain structures can be investigated with a normal spatial resolution of 50nm. Recently, certain developments are accomplished including magnetic dissipation imaging to investigate magnetization dynamics through studying the energy transfer between the cantilever and the magnetic sample, and low-temperature measurements to investigate magnetic vortices or local variations in the magnetic penetration length in superconductors [65] and colossal magnetoresistance materials [66]. Magnetic resonance force microscopy with electron spins [67] and microcantilever magnetometry [68] with exquisite magnetization sensitivity were applied to measure de Haas–van Alphen oscillations of the magnetization [69] and of hysteresis loops [70] directly. Among these applications, characterizing magnetic microstructures is one that is growing in significance [71]. Small magnetic structures are currently widely studied both from a fundamental research standpoint and for their potential applications in ultrahigh-density storage [72], spintronic devices [73] and biological nanomaterials [74-75]. This booming interest requires techniques to characterize these small structures individually. In general, magnetic

force microscopy is indispensable in the studies of the morphology, structure and properties of nanocomposites with magnetic inclusions. Magnetic force microscopy combines a modern technique of magnetic measurements with the unique potentials of scanning probe microscopy. The scanning probe microscopes make MFM possible to investigate conducting surfaces and to perform their targeted modification at an atomic and molecular level. Due to its high spatial resolution and sensitivity, MFM has become one of the most effective tools for characterizing the magnetic nanostructures in 3D dimensions. The sensitivity of the magnetic force microscope to the magnetic flux is only slightly lower than that of the SQUID-based scanning microscope. However, the potential of the technique MFM have not yet been fully explored in the context of the characterization of magnetic domains at nanoscale. This is mainly due to the complexity of all the numerous parameters such as the environmental conditions and characteristics.

## 2.2 Principle of Operation of Magnetic Force Microscope

### 2.2.1 Theory of Magnetic Force Microscopy

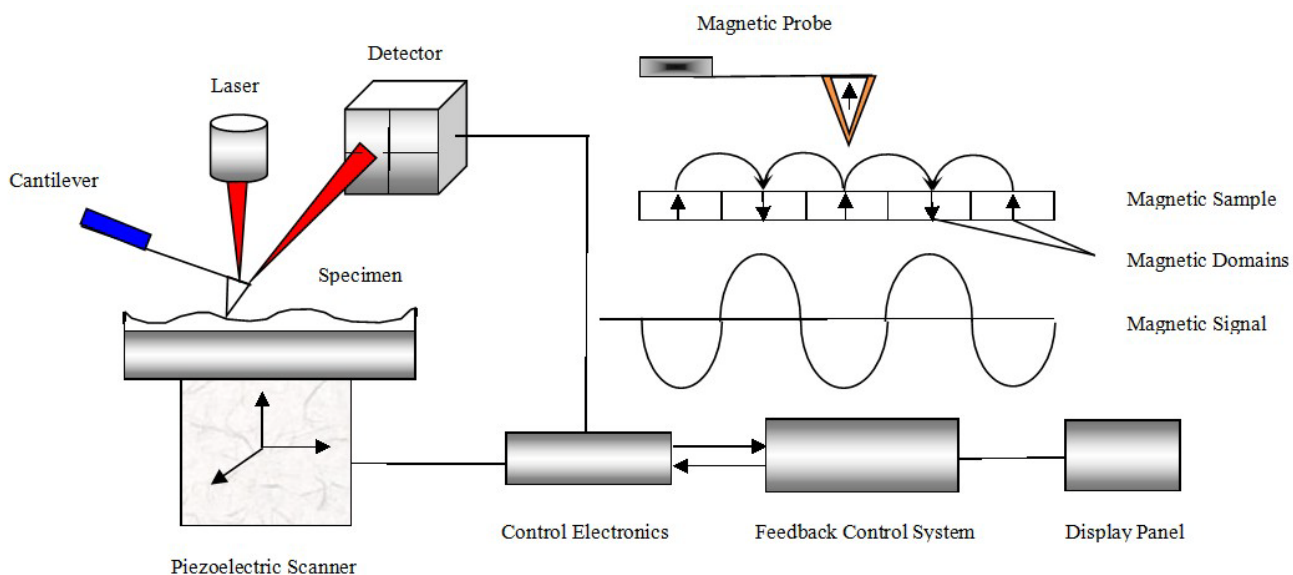


Figure 2.1 Scheme of magnetic force microscope

Magnetic Force Microscopy (MFM) utilizes a flexible lever--cantilever, with a magnetic tip to map force gradients near the surface of a sample. Cantilevers for both magnetic force microscopy and atomic force

microscopy are fabricated by microlithography using a silicon technology, which means that one or several cantilevers at a time are formed at the edges of a silicon plate. Then the surface of the tip is coated with a thin layer of a ferromagnetic material. During scanning the probe displacement value will be saved and interpreted as topography and magnetic phase image of the sample.

A standard two-pass technique is adopted by MFM. At each scan line, the topography is first acquired and then the scan is repeated on the same line. In this way topography cross-talk with the magnetic interaction is prevented, and the cantilever oscillation parameters during the second pass are used to build up maps of the long-range interactions. At each location, measurements are repeated twice to independently collect amplitude, phase and frequency shift. Frequency shift is automatically detected by using the phase shift as error signal for the feedback loop, which is used to track the variation of the resonance frequency by changing the dither frequency by means of the microscope control instrument. Phase is previously set with zero in correspondence of the maximum of the first free resonance peak to compensate false phase shifts since of the setup, while microscope parameters such as feedback loop gain and scanning speed are optimized to keep the phase signal to zero during second pass. During both the topographic tracking (first) pass and the second pass, the cantilever was dithered in high oscillation amplitude to prevent tip sticking to the particles capping layer by means of high elastic force. Due to both the long distance from the magnetic features and the tip blunting which resulted from its magnetic coating, the lateral resolution is significantly reduced with respect to standard AFM. Since the typical radius of curvature of commercial MFM probes lies in the range of 20–100nm, a comparable lateral resolution is expected to be within a certain scale. For nanocomposite samples, the MFM measurement will be carried out under a weak external magnetic field with orientation perpendicular to the stripes in-plane, giving prominence to magnetic texture in the sample. Both force gradient and a good signal-to-noise ratio can be found where is consistent with theoretical expectations, indicating that these signals are magnificent also for long-range forces in lift mode. Concerning the MFM interaction far from the surface, the force gradient image, which is local derivative, is more sensitive to noise than the oscillation phase and amplitude which is used in the energy loss images. Therefore, by using the energy loss signals, quantitative magnetic data is derived with the

same resolution as the phase images without detrimental effects of mathematical calculations [76]. Previous studies have demonstrated how energy loss imaging in tapping mode can provide high compositional sensitivity [77]. The Nèel-Brown model for uniaxial spherical particles describes physical process by a spin relaxation time, representing the average time for a nanoparticle magnetic moment to flip along the easy magnetization axis. This process is thermally activated with exponential dependence on the particle magnetization, thereby on its volume, which is described in the Arrhenius law. As a result, small changes in nanoparticle size can lead to very different magnetic properties at room temperature. The non-magnetic particles can still be magnetized by an external field, which will favor one of the two opposite easy magnetization directions, leading to a stable magnetic configuration as described by the Stoner-Wohlfarth model [78]. The application of the magnetic field during sample preparation will give rise to a cooperative effect of the single crystal magnetic particles that undergo orientation along the easy axis, resulting into a long-range ordering that minimizes their dipole-dipole interaction energy [79]. Due to compositional uniformity, long-range van der Waals forces are expected to give a uniform force gradient across the whole specimen, affecting only the mean value of the signal, while local fluctuations are attributed to the magnetic structure of samples.

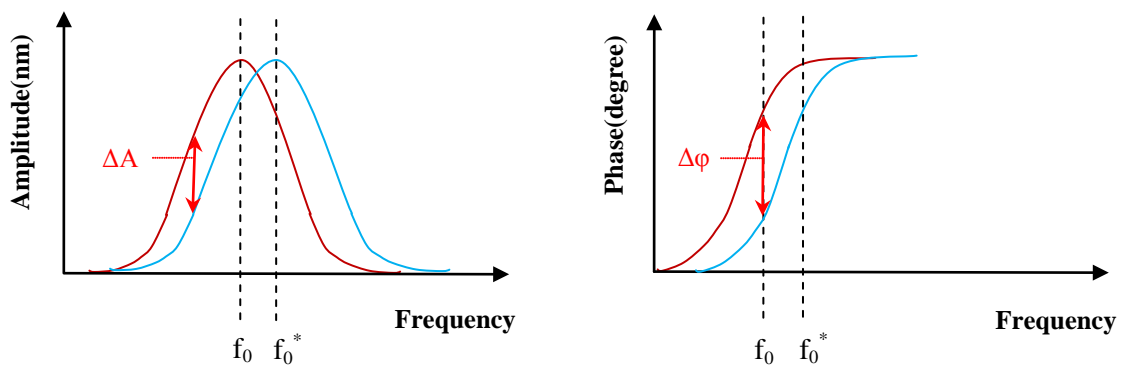


Figure 2.2 A change of the magnetic force on the tip results in a change in resonance frequency ( $f_0$ ) of the cantilever, which can be detected in two ways.

Magnetic Force Microscopy can record magnetic and topography texture simultaneously with both high magnetic sensitivity and nanometer spatial resolution, providing the nanometer resolution typical of atomic force microscopy (AFM). By means of a piezoelectric actuator the cantilever is put into oscillation at a frequency close to its resonant frequency. The action on the system of a force gradient which introduces a

variation of the resonance frequency, then a variation of the amplitude and phase shift. The images of topography are reconstructed by means of a "closed loop" technique, where the signal indicative of the amplitude of oscillation detected by the photodiode which is used as feedback to control the deformations of the scanner to adjust the height of the cantilever with respect to the sample so as to maintain the value of amplitude of oscillation always equal to a predetermined value. When the tip interacts with the sample, there is a change of the phase of the oscillation. The phase difference between the driving signal and the measured cantilever deflection is used to determine a new frequency of the interacting tips, then the topographic image is reconstructed from the assumed value of height at each point.

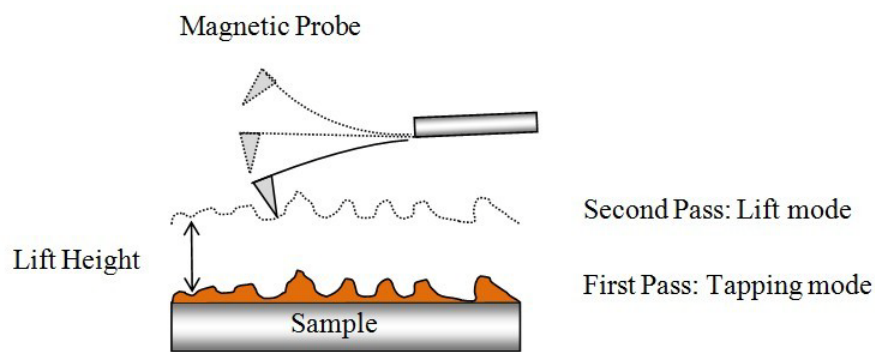


Figure 2.3 Two pass scanning method for MFM

When operating with MFM, one very important issue is to distinguish between the surface topography of the sample and the magnetic signal. It is necessary to minimize the interaction with other nonmagnetic force, such as Van der Waals forces. This is done using the technique of double scanning, each line is scanned in tapping mode or in intermittent contact mode; in which the topography of the sample surface is detected and recorded. During the second scan, the magnetic signal is detected. The tip moves at a certain distance  $\Delta z$  with respect to the surface of the sample and follows a trajectory which repeats the profile of the topography previously stored. This allows to obtain a tip-sample distance constant at all points of the area scanned, and then, heterogeneity in composition of the sample. It has an intensity of the Van der Waals force constant and equal at all points.



However, in order to compensate for the weak magnetic interactions resulting from the smaller magnetization of these super small magnetic nanomaterials, the tip has to be brought near the sample surface. This creates a convolution of the magnetic of surface features by forces acting on the tip.

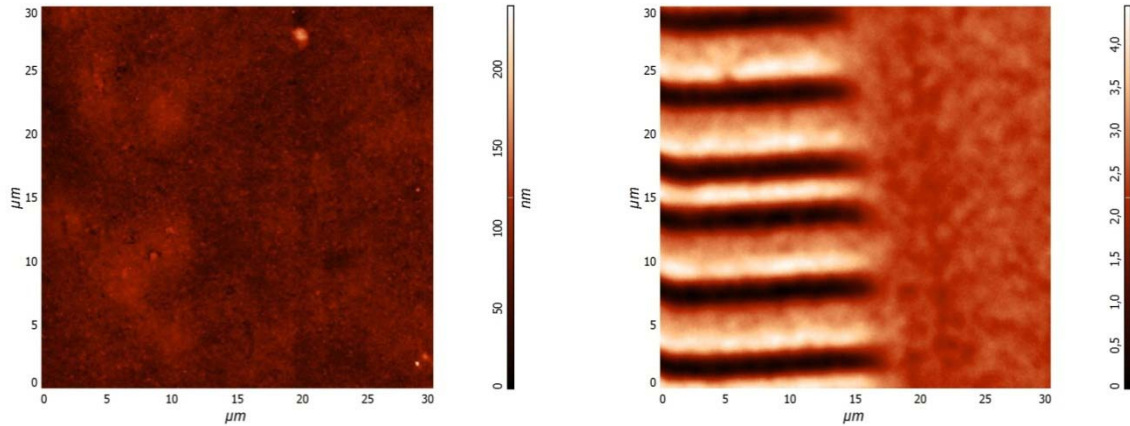


Figure 2.4 Surface topography image (floppy) with tapping mode obtained in first pass of MFM (left); corresponding magnetic image with lift height mode in second pass of MFM (right).

As an example, floppy disk was measured using magnetic force microscopy, the first scan or pass uses the semi-contact (tapping) mode of operation, where the surface topography is recorded to be used in the second scan (Figure 2.4). After the first scan, the cantilever is lifted above the surface at required height  $\Delta z$  and follows the same topographic contour. Because of the height  $\Delta z$ , the cantilever is only affected by long-ranged magnetic forces. In the MFM images, domains oriented according to the magnetization direction of the tip and it will appear as bright or dark regions, corresponding to contrasts phase positive or negative, independent on the direction of orientation. On the contrary, domains oriented in a direction orthogonal to the direction magnetization of the tip and it will give rise to regions of a color image intermediate corresponding to a phase contrast null.

The spatial resolution of MFM is related both to the geometry of the region of magnetized probe that is exposed to the field of the sample, and the distance between the tip and sample surface. In particular, in order to increase the resolution it is necessary that the region of the magnetized probe is reduced to the minimum possible size and that the height  $\Delta z$  is the shortest. The theoretical limit for the lateral resolution of the MFM technique is

5-10 nm, but the actual resolution obtained experimentally is 20-30 nm. Concerning the resolution of MFM the ideal conditions for obtaining high-resolution magnetic images consist with the use of tips of cylindrical shape with an apex spheroid having large ellipticity and a low height of the tip with respect to the sample. Another feature that affects the lateral resolution is the magnetic structure of the probe. It likes a probe in single domain with a high magnetic moment, while the multiple domains may make it extremely complex.

### **2.2.2 Magnetic Interaction between Tip and Nanoparticles**

Theoretical considerations allow for optimum choice of the MFM working parameters. Given the complexity of the physical phenomena that occurs during the measurements of MFM, the tip-sample interaction characteristics that are detected experimentally can be described only by the use of simplified models. In particular, the images obtained by MFM are the results of a convolution of the magnetic properties of the probe and the sample, which, in most cases, cannot be known accurately. Therefore, models describing the tip-sample interaction with simplified assumptions for these characteristics are intended to provide a description not exactly, but rather qualitatively of the processes that determine the formation of the magnetic contrast. Most of the models developed in this field are based on the assumption that both the tip and the sample can be considered as rigid, or that the states of magnetization of the tip and sample do not change during the measurement. We consider to neglect the effects of mutual magnetization time-dependent, both in terms of relative position of tip-sample and in terms of decay of the magnetization. This hypothesis of weak tip-sample interaction, allows us to examine the problem reduced to a simple magnetostatic one.

We know that the signal of MFM images normally is mapped with the phase shift to the image reconstruction. Here if one considers that the probe is modeled as a single dipole point  $\mu_1$ , interacting with a single dipole point of the sample ( $\mu_2$ ) placed at a distance. One can consider the dipole  $\mu_1$  (tip) oriented along the vertical axis: a) If the dipole  $\mu_2$  is oriented in a direction orthogonal to the z axis, the gradient of the force is zero; b) If the dipole  $\mu_2$  of the sample is oriented in a direction parallel to the z axis, the force gradient is maximum, and in particular

negative if the verses of the two dipoles  $\mu_1$  and  $\mu_2$  are concordant and positive if the verses of the two dipoles  $\mu_1$  and  $\mu_2$  is divided. c) For all other possible orientations of the dipole  $\mu_2$  the gradient of the force of interaction takes intermediate values between the maximum value and the null value, with positive or negative depending on the sign of the climb or vertical component of the dipole moment with respect to  $\mu_2, \mu_1$ .

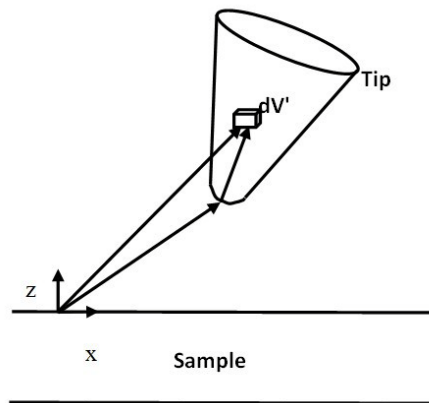


Figure 2.5 Tip-sample geometric model

The magnetic structure of the probe in most cases is not known with accuracy, it is therefore a schematized model. A first model summarizes the probe as a "single domain" characterized by a uniform magnetization, generally in the direction of the axis of the tip normal to the cantilever. In this case the magnetization vector of the tip is independent of the position; it is therefore independent of the magnetostatic energy of the probe in a simple dipolar response.

A more simplified but very representative model summarizes the probe as a single magnetic dipole. Regarding the modeling of the field produced by the tip, it is initially attributed to the sum of the dipole fields generated by all magnetic dipoles constituting the volume of the sample investigated. However, such a model albeit limited to the qualitative behavior of the probe interacting with a generic sample, provides a description that extremely approximates the real experimental situations to verify the analysis of different samples with different magnetic structures. Generally, the actual interaction probe-sample cannot be thought as a simple interaction of dipolar nature. For this reason, we have developed the model to describe the magnetic fields in MFM measurements.

We consider the case of a sample consisting of a sphere uniformly magnetized. Such a model may be indicative of magnetic fields and forces during MFM measurements of magnetic nanoparticles. For a uniform magnetized sphere with radius  $R$ , the magnetic moment is given by:

$$\vec{m}_s = \int_{V_s} \vec{M} dV = \frac{4}{3} \pi R^3 \vec{M} \quad (2.1)$$

The magnetic field in a uniform magnetized sphere turns out to be:

$$\vec{H}_s(\vec{r}) = -\nabla \Phi_s(\vec{r}) = \frac{1}{4\pi} \left[ -\frac{\vec{m}_s}{r^3} + \frac{3(\vec{m}_s \cdot \hat{r})\hat{r}}{r^3} \right] \quad (2.2)$$

Making use of the approximation of single dipole peak point, the strength of magnetostatic interaction between the probe and the uniform magnetized sphere can be expressed as:

$$\vec{F} = \mu_0 \nabla (\vec{m}_{tip} \cdot \vec{H}_s) = \mu_0 \nabla \left( \frac{3(\vec{m}_{tip} \cdot \hat{r})(\vec{m}_s \cdot \hat{r}) - \vec{m}_{tip} \cdot \vec{m}_s}{r^3} \right) \quad (2.3)$$

If both dipoles ( $m_s$  and  $m_{tip}$ ) are directed in the  $z$  direction, and also the joining  $r$  is directed in the same direction, now the force between the tip and sample is:

$$F = -\frac{6m_{tip}m_s}{z^4} \quad (2.4)$$

the gradient of the force is given by:

$$F' = \frac{\partial F}{\partial z} = \frac{24m_{tip}m_s}{z^5} \quad (2.5)$$

Forces between the tip and the sample, such as electrostatic forces (proportional to  $1/z^2$ ), Van der Waals forces (proportional to  $1/z^7$ ) and damping forces, may contribute to the force gradient which is subject to the cantilever and therefore provide additional signals (of variation of amplitude, frequency or phase) with respect to the magnetic signal. In the implementation of MFM technique, if obtained images are purely related to the magnetic properties of the sample, it is necessary to separate the contribution of the signal relative to the coupling

magnetostatic tip-sample and the contribution of all other possible "topographic" interactions. This operation is particularly critical in the case, in order to increase the resolution, when the tip is maintained at very close range with respect to the sample, at which the contributions of the non-magnetic forces to the signal (in particular the electrostatic forces and the Van der Waals forces) may be relevant. Given the rapid decrease of the Van der Waals forces with the tip-sample distance, the elimination of the effect of these forces can be obtained by setting high values of the height of the scan. In this way, however, there is also a decrease of the magnetic signal detected and the resolution of the instrument.

### **2.2.3 Operation of Magnetic Force Microscopy**

A schematic diagram of the magnetic force microscope is shown in Figure 2.1. The specimen is set on a piezoscanner, which provides spatial trajectory of the specimen along the three coordinate axes. The magnetic force which is acting on the tip leads to a bending of the cantilever and a vertical displacement of the tip. The piezoscanner is a thin wall tube made of piezoceramics which are coated with a series of metal electrodes. The electric voltage applied on the electrodes changes the geometric setting of the thin wall tube because of the inverse piezoelectric effects. The piezoscanner has a high mechanical rigidity, thus it is insensitive to seismic and acoustic interferences. Errors of movements resulted from nonlinear properties of the materials are the drawbacks of the piezoscanner. However, these movement errors can be reduced by software control, such as by applying a controlling voltage to the electrodes of the piezoscanner which is consistent with special correcting algorithms. In metrological systems, additional capacitive and optical transducers are adopted; they provide the linear movement of the specimen in the range from 1 to 250 mm in the plane of the specimen (along the x and y coordinates) and from 1 to 15 mm normal to this plane (along the z coordinate) for different piezoscaners [80-82].

In magnetic force microscope, according to Hooke's law, the movement of the cantilever is determined by the mechanical rigidity of the cantilever with the spring constant  $k_c$ , this value is typically in the range from 0.1 to 10 N/m. Bending of the cantilever is detected by a small displacement transducer. A laser beam is fixed on the

reflecting surface of the free end of the cantilever and the position displacement of the reflected light beam indicating bending of the cantilever is determined by the photodiodes. When scanning the specimens, the probe successively scans every of sample surface and the electronics detects the total interaction force in the probe - sample scanning system. After processing of the data results of measurements are displayed, simultaneously three-dimensional (3D) images of the surface will be collected.

As we have shown, the tip scans the same surface area twice. For the first pass, it moves contacting the surface of the specimen and gets the trajectory of the movement of the tip, which corresponds to the profile of the sample surface for research and is stored in a computer. In this step, the magnetic properties of specimen have no effect on the observed results. For the second pass, the magnetic tip moves along the known trajectory above the same surface area without contacting the specimen surface. In this case, the tip is affected by long range forces (mainly magnetic force rather than Van de Waals force in the first scan). The deviation of the tip from the specified trajectory depends on the magnetic properties of the specimen. In actual operations, in order to achieve a maximum sensitivity, oscillations induced by the cantilever are given a natural resonant frequency and the tip also scans the specimen twice, first in tapping mode and second scan in free oscillations mode at a certain distance from the surface. Recording the amplitude, phase or frequency of the oscillations provides more precise information on the magnetic results of the specimen.

Nonmagnetic interactions between an MFM tip and a magnetic sample like electrostatic and van der Waals forces give interference to the magnetic resolution. So how to separate the magnetic signal from the other interactions becomes an essential issue. Attention also needs to be paid to avoid artifacts that result from the unavoidable magnetic tip stray field. Control can be achieved by optimizing the MFM operation mode as well as the tip parameters. It is possible to use the tip stray field to manipulate the magnetic-moment state.

Here we introduce three modes of scanning of MFM. Generally, in order to obtain a magnetic structure image, MFM can be operated in constant-frequency-shift mode, tapping mode and constant height mode. The first one is a profile of constant frequency, which reflects a combination of magnetic, electrostatic, and Van der Waals

forces, therefore, the obtained images usually have overlapping with topography. In order to prevent the MFM tip from crashing into the samples, unavoidable sample slope can be compensated by correction software, which allows the MFM tip to fly over the sample surface following a slope obtained during constant-frequency-shift mode scan. The tapping mode scanning can efficiently separate topography contrast and magnetic interaction. In this mode, the sample is scanned twice. The sample topography is obtained in the tapping mode using the cantilever oscillation amplitude as a feedback signal. The magnetic contrast is subsequently obtained in the tapping mode scan by monitoring the cantilever's frequency or phase shift upon the previously measured topography with a controllable height offset. The typical problem associated with a tapping mode scan is that the MFM tip stray field can produce a substantial distortion of the sample magnetic structures. Tapping mode is complementary in acquiring good images. For magnetic particles with a large coercivity field, tapping mode can be confidently applied. For magnetic particles with small switching fields, constant height mode should be adopted. Irreversible distortion induced by the tip stray field can be substantially reduced by operating the MFM in constant height mode. In this mode, instead of tracking the sample's topography, the tip is scanned across the surface at a predetermined constant height while the cantilever frequency shift is monitored. The constant height mode has the best signal-to-noise ratio and the potential of increased scan speeds, but requiring the sample is flat enough.

### **2.3 Application of Magnetic Force Microscopy**

With magnetic force microscopy it is possible to observe single magnetic domain whose size varies from several nanometers to several tens of nanometers. The most popular application is for creation of materials for magnetic recording media like magnetic tapes, hard disks, magneto-optical disks [83] and recording modes of magnetic heads (stroboscopic imaging of an alternating magnetic field from a perpendicular magnetic recording head by frequency-modulated magnetic force microscopy) [84] in the process of design and quality control of the products. MFM also was applied to the studies of the structure and properties of nanomaterials, the studies of superconductors as well as in biological and geophysical studies [85]. Micromagnets play a significant role not

only in artificial systems, but also in nature. The use of magnetic force microscopy in the studies of magnetic properties of biological application is promising. For instance, bacteria *Aquaspirillum magnetotacticum* can move along the magnetic field lines. These bacteria contain specific organelles called magnetosomes. The magnetosomes are chains of 10 to 25 permanent magnets. Single crystals are clearly seen in nonstained cells using transmission electron microscopy (TEM) [86].

Recent research advances related with magnetic force microscopy can be divided into three groups: a) preparation and characterization of magnetic materials; b) optimization of MFM operation proceedings; c) theoretical study on the mechanism and mathematical simulation. With magnetic force microscopy, nanoparticles such as isolated metal nanoparticles [87-89], Si and MnO nanoparticles [90] are studied. Another form of magnetic nanomaterials - the alloy film - has already been detected using MFM. These materials include  $\text{Co}_{22}\text{Ag}_{78}$  granular film [91],  $\text{Fe}_{81}\text{Ga}_{19}$  film [92], electrodeposited thick film of Co-rich CoPt alloys [93], highcoercivity Nd-Fe-B sintered magnet [94], barium ferrite ( $\text{BaFe}_{12}\text{O}_{19}$ ; BaM) single crystal [95], Co film [96], B-containing PrFe and PrCo based film [97], epitaxial Ni-Mn-Ga film [98], SiCo and GeCo film [99] and Fe-Ga bulk alloy [100]. Witold Szmaja et al. made a detailed magnetic force microscopy study on the domain structure of isotropic nanocomposite  $\text{Nd}_2\text{Fe}_{14}\text{B}/\text{Fe}_3\text{B}$  magnet ribbons prepared by melt-spinning [101]. Ignacio Garcí'a et al. studied the domain structures of a magnetostrictive  $\text{Fe}_{40}\text{Ni}_{38}\text{Mo}_4\text{B}_{18}$  amorphous ribbon at room temperature by MFM [102]. MFM has been used to characterize magnetic nanoparticles, mainly ferromagnetic, and has proven itself to be a useful imaging technique [103]. The biological applications include the detection of iron compounds associated with neurological disorders [104] and magnetic domains in magnetotactic bacteria [105]. There are relative few studies on detecting magnetic nanoparticles, specifically superparamagnetic iron oxide nanoparticles (SPIONs), in vitro [106-108]. With respect to characterization to SPIONs, MFM is an underused technique that shows great potential.

Larger tip magnetic moment of magnetic force microscopy gives better current detection although it raises not only the sensitivity of the magnetic field but also the zero-current MFM signal. Low magnetization tips have



been found appropriate to the magnetic characterization of soft magnetic materials such as “duplex” stainless steels [109]. MFM probe based on an iron filled carbon nanotube in MFM measurements in external fields has been realized [110] too. Using combination of micromagnetic calculations and magnetic force microscopy (MFM) imaging, V. Cambel et al. have explored optimal parameters for novel magnetic tips suitable for switching magnetization MFM [111]. Optimal values of the lift heights were discovered in the range 60 - 80 nm, depending on the nature of the sample and the type of the tip used.

Besides experimental research, simulation and modeling of MFM get developed these years [112]. By comparing the standard images of various types of nanoparticles, it was found that the –monopole and dipole models do not accurately describe the MFM imaging mechanism [87]. A transfer-function approach to calculate the force on a magnetic force microscope tip and the stray field due to a perpendicularly magnetized medium having an arbitrary magnetization pattern was presented by Hans J. Hug [113]. Simulations of magnetic force microscope (MFM) contrast for low-coercive ferromagnetic and superparamagnetic nanoparticles was made. The studies showed that two types of MFM contrast could be in the form of Gaussian and ring distributions because of probe-particle interaction [114].

## Chapter 3

# Magnetic Force Microscopy for Soft Thin Films

In this chapter, we describe phase difference magnetic force microscopy (PD-MFM), which is a MFM based technique we developed in order to measure the thickness of soft thin films. PD-MFM allows one to measure the thickness of soft thin and ultrathin films deposited on periodically patterned magnetic substrates. To demonstrate the technique, standard floppy disks were used to obtain the periodically patterned magnetic substrates, while bacterial cells of *Staphylococcus aureus* were cultivated for the layer formation with limited lateral dimensions. Magnetic signals (the phase contrast) is expressed in Fourier series to get the theoretical interpretation of MFM. Together with the detailed discussion on the relationship between the phase contrast and tip-sample interaction, we demonstrate the feasibility of PD-MFM in detecting the thickness of soft thin films. Depending on the merits of this technique, in order to increase the accuracy, the relative error and the uncertainty of PD-MFM have been discussed as well. The results of this study have been reported in *Ultramicroscopy* 136 (2014) 96–106.

The study is organized as follows. At first, we give research background of thin film technology and details of the sample preparation, as well as the techniques employed for the characterization of the samples. Then, morphological properties and the corresponding magnetic response of a layer of the bacterial cells on periodically patterned magnetic substrates are described using AFM/MFM measurements. The results and discussion of the magnetic characterization are reported to deduce the approach of measuring the thickness accurately. The proposing work in the future and conclusions are drawn at the end.

### 3.1 Introduction

Thin films have been used for more than a half century in making electronic devices, optical coatings, instrument hard coatings, and decorative parts as a low-dimensional material created by condensing species of matter on a substrate. The thickness of the film can be less than several microns. Thin film technology (for nanometer materials and/or a man-made super lattice) are available for minimization of toxic materials with

low energy consumption due to limited surface.

### **a) Bacterial biofilms**

Biofilms are a group of microorganisms in which cells stick to each other and are frequently embedded within a self-produced matrix of extracellular polymeric substance (EPS). Biofilms are involved in a wide variety of microbial infections in the body. Thick and thin biofilms and their resistance to antibiotics have been observed, bacterial biofilms also find applications into wastewater treatment as chemical catalysts. The thickness of thin film affects the mechanical and electrical properties of polymer thin films [128-130], precisely controlled thickness and the accurate measurement of soft film thickness are getting more important.

### **b) Thickness detection with nanocharacterization techniques**

In generally it is versatile to measure the thickness of stiff film by contacting the film surface with scanning probe techniques. Conversely, for soft films these methods will lead to underestimation of the thickness and damaging the samples. Up to now, there are many non-contact techniques have been considered, such as white-light interferometry [131-132], spectroscopic ellipsometry [133], laser triangulation [134], ultrasonic reflectometry [135], Raman spectroscopy [136], siphon effect [137], Compton scattering [138], waveguide fluorescence microscopy [139], quartz microbalance [140] and compression testing [141-142]. However, each of them has limitation on measurable thickness range and special requirement of sample preparation. Atomic force microscopy (AFM) characterizes the morphology and the surface properties for its unique detecting compatibilities and high resolutions. With its unique semi-contact mode (tapping mode), AFM investigates the surface of biological soft samples in air as well as in liquid without destroying the surface. Hong et al. [146] deposited polymeric thin film on mica substrates, obtained a different height measurements between the sample surface and the substrates, but the maximum measurable thickness is limited by the vertical range of AFM. Moreover, other less straightforward methods have been applied to measure the thickness of ultrathin biofilms. The thickness of thiol-modified strands was measured from the difference in the height of edges of microstructured substrates from AFM topography before and after selective

adsorption, both in air and liquid environments [147]. Also thickness of purple membrane layers deposited on conductive substrates retrieved from the tip-film-substrate capacitance measured by AFM-based capacitance imaging [148].

In this work we perform an approach based on magnetic force microscopy (MFM) to measure the thickness of soft thin films (in principle it could be extended to stiff films) deposited on periodically patterned magnetic substrates. Floppy disks have been chosen for this study as they are easy to be procured, cheap and easy to be cut as substrates for the preparation of samples. Moreover, they have been studied with MFM like other recording media such as magnetic tapes [149-156]. The soft thin films were obtained by cultivating bacterial cells of *Staphylococcus aureus*. In the following, the samples and the technique mentioned above are illustrated.

## **3.2 Materials and Methods**

### **3.2.1 Equipments**

#### **a) MFM apparatus**

Experiments were performed using MFM apparatus, the accuracy of the calibration of piezoelectric actuator in the z direction was checked using calibration gratings in advance. The MFM apparatus was equipped with standard Si cantilevers with a 40 nm thick CoCr magnetic coating. The magnetic domains of the tip were vertically oriented by a magnet. In the double scanning method of MFM, the first pass, topographic images were obtained in tapping mode; in the second pass, the magnetic tip was lifted above respect to the surface of sample with different values of distance  $\Delta z$  between the tip and the samples, the tip oscillating at its first resonance frequency with amplitude approximately 15 nm was chosen. Experiments were performed in air and at room conditions.

#### **b) Dynamic light scattering measurement**

Dynamic light scattering (DLS) was used to determine mean size and size distribution of bacterial

suspension. The bacterial dispersions were diluted 100 times with water to avoid multi-scattering phenomena. Water used in DLS experiments was filtered through 0.45  $\mu\text{m}$  cellulose filters to eliminate dust particles. DLS was also used to evaluate zeta potential ( $\zeta$ ) of bacterial suspension appropriately diluted (1:10) in bidistilled water at 25°C. The laser doppler anemometry was used to measure the electrophoretic mobility of bacteria. The  $\zeta$  value was calculated from the electrophoretic mobility in the smoluchowsky approximation. Reported data represent mean value of  $\zeta$  and of the hydrodynamic diameter for bacteria. Results of DLS experiments are given as the average values obtained using samples from three different batches  $\pm$  standard deviation.

Table 3.1 Apparatus and parameters

Items	Manufacturer	Parameters
AFM setting	Solver, NT-MDT, Russia	
Calibration	TGS1, NT-MDT, Russia	TGZ1, 23 $\pm$ 1nm
Magnetic Tip	MESP-RC, Bruker Inc.	$k_c = 5 \text{ N/m}$ $F_0 = 150\text{-}190\text{kHz}$
DLS measurement	Malvern Nano ZS90, Malvern Instruments Ltd., Worcestershire, UK	$T = 25^\circ\text{C}$ scattering angle = 90.0 deg

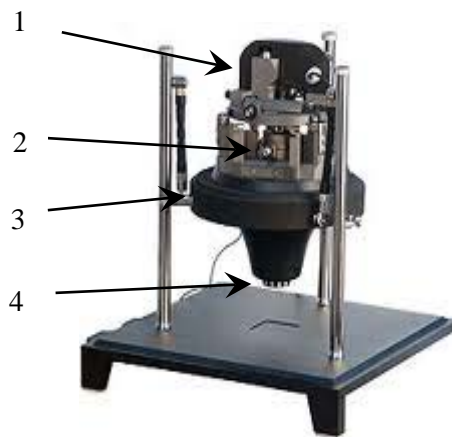


Figure 3.1 General view of Slover Pro measurement module

1-measuring head; 2- position devise; 3-approaching module; 4-knob of hand approaching

### 3.2.2 Sample Preparation

#### a) Bacterial species

*Staphylococcus aureus* is a bacterial specie with spherical shape about 1  $\mu\text{m}$  in diameter arranged in clusters with a robust cell wall made of several layers of peptidoglycan. The bacteria are able to adhere to inorganic surfaces by chemical and physical interaction, subsequently, they can produce a thick layer of organic exopolysaccharides and embed themselves in it.

### b) Substrate and biological thin films

*Staphylococcus aureus* ATCC 6538 was used to create a biological thin film adhering on floppy disk. To obtain a thin layer of organic matter, we induce bacterial adhesion without biofilm production, by cultivating *S. aureus* in Brain Heart Infusion (BHI, Oxoid) broth with pieces of previously sterilized floppy disk for 90 minutes at 37°C. Standard floppy disks with area approximately 2cm<sup>2</sup> were obtained as periodically patterned magnetic substrates. After incubation, colonized floppy disks were gently washed three times with sterile water to remove non-adherent bacteria and then H<sub>2</sub>O<sub>2</sub> sterilized. In this way, on the surface of the floppy disks, we obtained a thin layer of adherent bacterial cells with a thickness corresponding to one (more rarely two) cell diameter.

### c) Dynamic light scattering measurement

The diameters of viable and sterilized *S. aureus* cells were determined by DLS as high as 1160±40 nm and 940±140 nm, respectively, which indicates that the sterilization process does not significantly alter the dimension of bacteria size.

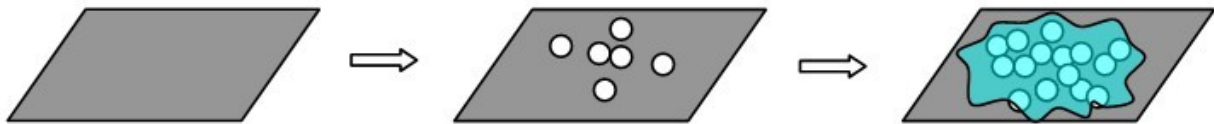


Figure 3.2 Biological thin film production on floppy disk

### 3.2.3 Technique Theory

In the following, we limit the theoretical discussion to the one we used in this study. Firstly, an interpretation of the symbols is given as follows:

$\Delta z$ : distance between the tip and the samples;

$\delta$ : frequency shift in harmonic oscillator of the tip related through the slope of the resonance peak;

$\phi$ : phase used as the magnetic signal in MFM response;

$F_z$ : component of the force vector in the  $z$  direction;

$\partial F_z / \partial z$ : derivative of the tip-sample force  $F(x, y, z)$  in the  $z$  direction, since the phase shift is proportional to the derivative of the tip-sample force  $F(x, y, z)$  in the  $z$  direction;

$k_c$ : cantilever spring constant;

$Q$ : quality factor of the cantilever first resonance [157–159];

$B$ : magnetic field;

$\lambda$ : spatial period of periodically patterned magnetic substrate;

$m_{\text{tip}}$ : magnetic momentum of tip;

$\xi_0$ : decay length of magnetic signal in the direction normal to the sample surface;

$z$ : distance between the tip and substrate;

$h$ : measurable thickness of films.

### a) MFM setting

In MFM, an AFM equipment is set with a tip with a magnetic coating (CrCo) a few tens of nanometers thick. The sample surface defined in the  $x$ - $y$  plane is divided in an array of  $s$ . With the unique double scan method of MFM, the surface profile of each line along the  $x$  direction is recorded in standard tapping mode in the first pass. During the second pass, the scanning is repeated at a fixed lift height  $\Delta z$  between the tip and the sample surface (assuming  $z$  axis normal to the sample surface, the sample surface corresponding to  $z = 0$ ) with the tip oscillating at its first resonance frequency. The deflection signal of phase shift  $\phi$  is used as the magnetic signal and recorded at each of the scanned area. Obtained results are interpreted as the magnetic domains distribution of the sample surface.

### b) Magnetic phase

Supposing the cantilever is driven at its first resonance, the phase shift  $\phi$  is proportional to the force gradient

$\partial F_z/\partial z$ . The relation between them shows here:

$$\varphi = \frac{Q}{k_c} \frac{\partial F_z}{\partial z} = C \frac{\partial F_z}{\partial z} \quad (3.1)$$

The gradient of the tip-sample force  $F(x, y, z)$  in the  $x$  and  $y$  direction is not considered, since it is practically excluded in MFM measurement by restricting the tip movement vertically.

### c) Tip-sample interaction

The magnetic tip can be lift far from the sample surface, that means the choosing parameter  $\Delta z$  is large enough to neglect the short-range tip-sample interaction. Variation of phase shift  $\varphi$  reflects variation in the tip-sample long-range forces, such as electrostatic force and magnetic force. Limiting the discussion to magnetic interaction, in the case of a sample with magnetic domains periodic along one direction in the plane, e.g., the  $y$  direction, with period  $\lambda_0$ , the magnetization within the sample can be expanded in a Fourier series [160]. In this case, it can be deduced that the force gradient  $\partial F_z/\partial z$  can be expanded in Fourier series, where  $n$ -th harmonic contribution has amplitude  $M_n = |M_n|e^{i\delta_n}$ .

### d) Magnetic field in the $y$ and $z$ directions

$B_y$  and  $B_z$  in the vector matrix on the left side indicates the components of magnetic field  $B$  in the  $y$  and  $z$  direction. On the right side, the components are expressed by the  $n$ -th harmonic contribution. Supposing the magnetization constant throughout the thickness of the sample, the magnetic field  $B$  produced by the floppy in air has two components, i.e., along the  $y$  and the  $z$  directions, given by

$$\begin{pmatrix} B_y \\ B_z \end{pmatrix} = \mp \sum_n B_n e^{-nkz} \begin{pmatrix} \cos(nky + \delta_n) \\ \sin(nky + \delta_n) \end{pmatrix} \quad (3.2)$$

Where  $B_n$  depends on  $|M_n|$  and the thickness of the sample and  $k = 2\pi/\lambda$  [160].

### e) Expression for the MFM response

The gradient  $\partial F_z/\partial z$  equals magnetic momentum of the tip  $m_{ip}$  multiplied by the second order derivative of the magnetization force  $B_z$  in the  $z$  direction. If the MFM tip is uniformly magnetized with magnetic momentum  $m_{ip}$  along the  $z$  direction, the force gradient  $\partial F_z/\partial z$  can be evaluated as



$$\frac{\partial F_z}{\partial z} = m_{ip} \frac{\partial^2 B_z}{\partial z^2} = m_{ip} \sum_n (nk)^2 B_n e^{-nkz} \sin(nky + \delta_n) \quad (3.3)$$

Thus, the magnetic phase shift can be expressed into:

$$\varphi = Cm_{ip} \sum_n (nk)^2 B_n e^{-nkz} \sin(nky + \delta_n) = \sum_n A_n e^{-nkz} \sin(nky + \delta_n) \quad (3.4)$$

where  $A_n = Cm_{ip}(nk)^2 B_n$  is the coefficient of the n-th term contribution to  $\varphi$  [160].

#### f) Periodic decaying of the magnetic signal

The expansion in Fourier series is commonly used in theoretical assessment of the contributions of each component. The total effect is expressed by the sum of all n-th harmonic contribution, of which the negligible parts will be deleted in the simplified models with practical applications. Then the magnetic field B is expressed by n-th harmonic contributions.

It is helpful to introduce parameter  $\zeta_0 = 1/k = \lambda/2\pi$  that represents the decay length of the magnetic signal in the direction normal to the sample surface. Thus,  $\varphi$  can be expressed as the sum of the terms periodically varying in one direction of the sample surface like y direction, constant in the other one like x direction, and decaying in the direction normal to the surface like z direction as  $\exp(-nz/\zeta_0)$ . The contribution of higher harmonics decays more rapidly as the index n grows.

Supposing the sum in Eq.(3.4) is limited to the first term, the MFM signal can be given by

$$\varphi = A \sin(ky + \delta) \exp(-kz) = A \sin(ky + \delta) \exp(-z/\zeta_0) \quad (3.5)$$

The phase shift  $\varphi$  will show a trend as periodically changing in y, constant in x, and decaying in the z direction which is normal to the surface. And, the higher n-th harmonic contributions can be neglected due to the more rapid decaying as the index n grows. The deletion of the higher n-th components simplifies the discussion in this study.

#### g) The high n-th components of phase contrast

Eq. (3.5) shows the MFM response as pure sinusoidal magnetization of the sample (which generally does not happen with floppy disks) which is depend on the assumption that the tip-sample distance is large enough to

neglect the terms corresponding to  $n > 1$  in the sum of Fourier series. In this case, experimentally encountered in this work, Eq. (3.5) can be used to describe  $\varphi(z)$  using an "effective" value of  $\xi_0$  provided by MFM, as described before. In this approximation,  $z$  is defined as  $\Delta z$ , the lift height. It can be found that the difference  $\Delta\varphi = \varphi_A - \varphi_B$  between the phase value  $\varphi_A$  and  $\varphi_B$  from Eq. (3.5) at two different  $s$  on the sample surface and  $\Delta\varphi$  can be expressed as

$$\Delta\varphi = A_d \exp(-kz) = A_d \exp(-z/\xi_0) \quad (3.6)$$

where  $A_d = A(\sin(ky_A + \delta) - \sin(ky_B + \delta))$  is a constant depending on the position of the two  $s$  A and B.

### **h) Application of MFM in soft film detection**

In the above showed theory, the MFM signal depends on the tip–substrate distance with neglecting the possible objects with magnetic properties different from those of air/vacuum present on the floppy. Assuming that soft films are diamagnetic or paramagnetic, which can be magnetized by the magnetic field produced by magnetic substrates. They could modify the magnetic field sensed by magnetic tip. For diamagnetic/paramagnetic materials, a reasonable approximation can be made to neglect the magnetic field produced into the material by its magnetization with respect to the external field produced by the magnetic substrates. In such an approximation, an infinitely extended film with magnetic susceptibility  $\chi_m$  lying on the floppy, the additional contribution to the magnetic field sensed by the tip is found to be identically zero (see Appendix A). It can be demonstrated that whether or not the diamagnetic/paramagnetic spheres are present, the relative correction in MFM signals can be neglected as it is smaller than  $10^{-4}$ – $10^{-5}$ , lower than the noise level of the present system. Therefore, in the following the effect of  $\chi_m$  of the film/bacteria is neglected.

## **3.3 Results and Discussion**

### **3.3.1 Analysis of the Substrates**

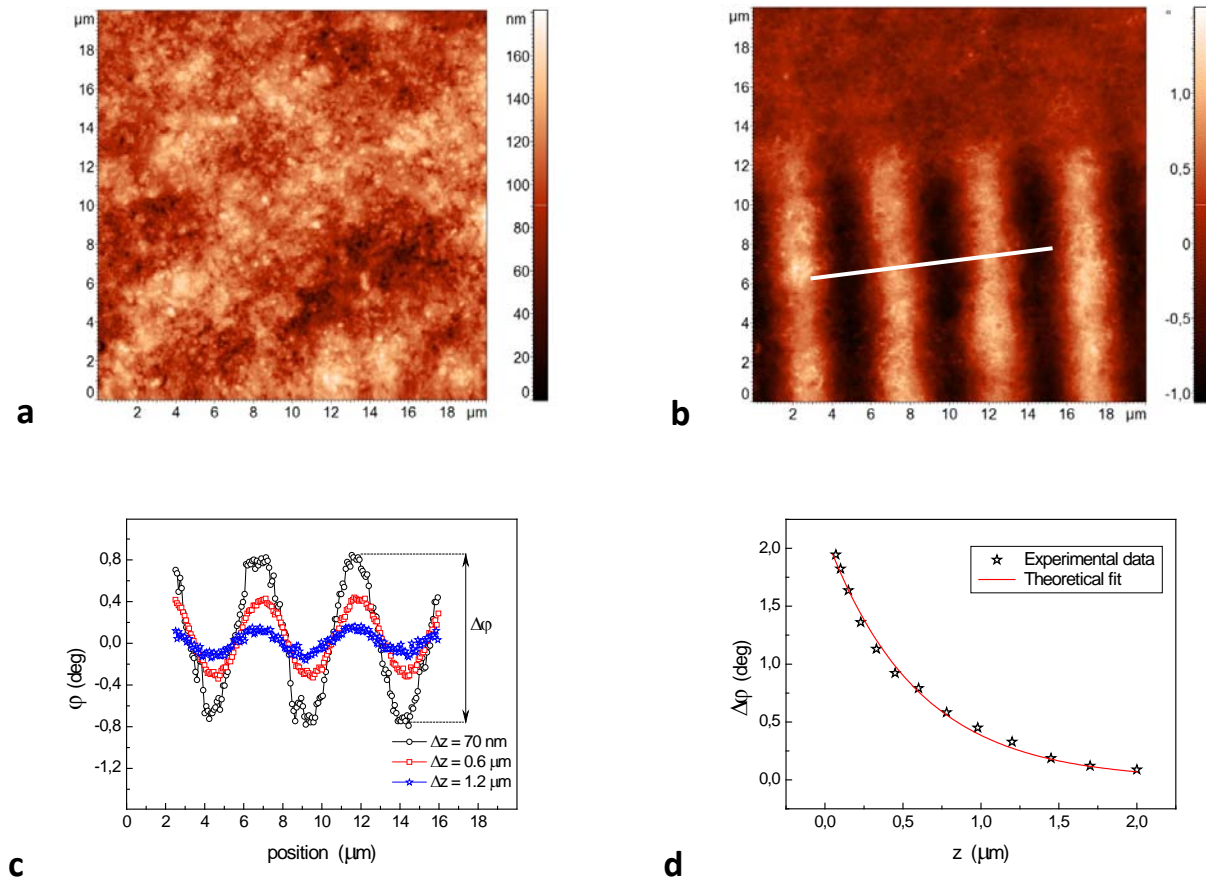


Figure 3.3 MFM characterization of floppy disk: (a) surface morphology; (b) magnetic phase contrast image with lift height  $\Delta z = 100$  nm; (c) sections of the line in (b) obtained from the phase images with three different values of  $\Delta z$ ; (d) phase contrast  $\Delta\phi$  of the different distance  $z$  between the tip and magnetic substrate (symbols) together with the corresponding theoretical fit using Eq. (3.6).

### a) High resolution images

The morphology of a floppy disk and the corresponding magnetic phase image with subtracting of the average plane are shown in Figure 3.3a-b, the images are acquired for  $\Delta z = 100.5$  nm. Analogous images of the same area have been collected for different value of  $\Delta z$  ranging from 70 nm to 2  $\mu\text{m}$ . MFM images reveal clear structure with high resolution of the periodic domains on floppy at low values of the distance between the tip and the samples. Detailed discussion on magnetic phase image is given as follows. Interpretation of the contrast in MFM images in terms of the orientation of the magnetic domains of the sample and of the tip can be found in Ref. [150].

### b) Analysis of phase profiles

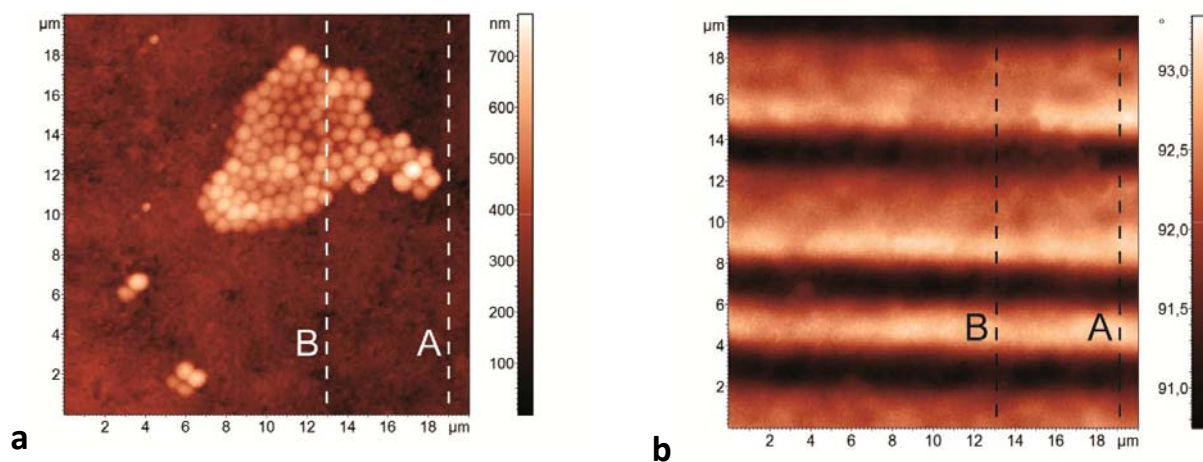
Figure 3.3c shows the profiles of the line in MFM images for different values of  $\Delta z$ . The values of  $\Delta\varphi$  decrease with increasing  $\Delta z$ . For low values of  $\Delta z$  the profile of  $\varphi$  is slightly deformed since of higher harmonics of the periodic magnetization of floppy. Figure 3.3d shows the values of  $\Delta z$  obtained from each MFM image as a function of  $z$  (the distance between the tip and the magnetic substrate).

### c) Theoretical fit of the experimental data

The theoretical fit of experimental data using Eq. (3.6) in Figure 3.3d demonstrates that the simple model of sinusoidal magnetization of the sample. With analysis the exponential fit gives  $\xi_0 = 586$  nm, which is slightly lower than  $\lambda_0 = 3.68$   $\mu\text{m}$  (the calculated spatial period of the magnetic pattern). This difference can be due to the higher harmonics of the floppy magnetization, which contribute to the magnetic response with rapidly decaying terms of the sum in Eq. (3.4). Therefore the value of  $\xi_0$  is an "equivalent" value that is expected to be lower than the experimental one. Thus, the theoretical fit can be considered as an approximation for calibration purposes.

By showing three different values of  $\Delta z$  ( $\Delta z$  is tip-sample distance) in magnetic phase images, phase profiles in the white line reveal the effect of the high harmonics of the sample magnetization during the theoretical exponential fit. This justifies the simple model of sinusoidal magnetization with good theoretical fitness.

### 3.3.2 Thickness Measurement



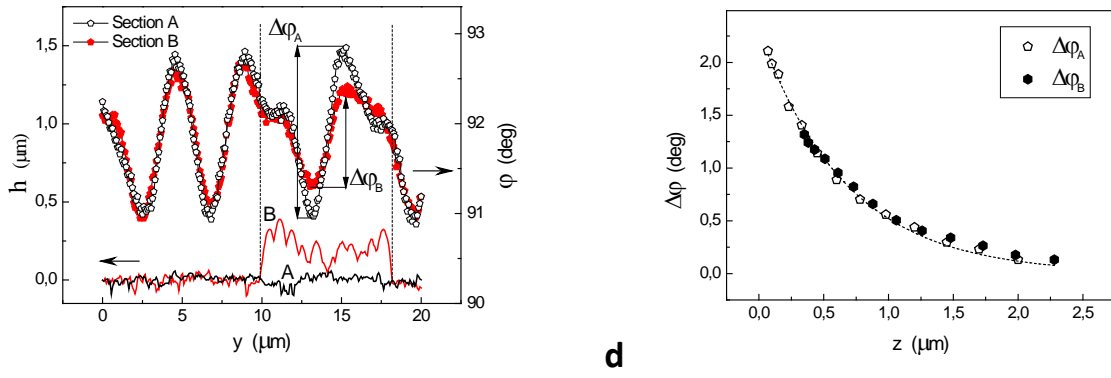


Figure 3.4 MFM characterization of a colony of *S. aureus* on floppy disk (a) topographical image; (b) corresponding magnetic phase image with  $\Delta z = 100.5$  nm; (c) profiles of the floppy (line A) and of the bacteria (line B) extracted from the magnetic phase image together with the profile of line A and line B extracted from the topographic image; (d) phase contrast  $\Delta\phi$  of the substrate and of the bacteria ( $\Delta\phi_A$  and  $\Delta\phi_B$ ) for different values of  $z$  (symbols) together with the theoretical fit of  $\Delta\phi_A$  using Eq. (3.6).

### a) Ellipsoidal bacterial shape and magnetic phase images

Figure 3.4a shows the morphology of a colony of bacteria on floppy disk. Smaller groups with four and two bacteria are also clearly visible. Bacterial cells are shown with roughly ellipsoidal shape, the diameter in-plane is about  $0.8 \mu\text{m}$  and height is not greater than  $400$  nm, which result from the effect of cells dehydration on the substrate. Figure 3.4b shows the corresponding magnetic phase image with tip-sample distance  $\Delta z = 100.5$  nm. Analogous phase images have been obtained in the same area with values of  $\Delta z$  from  $70$  nm to  $2 \mu\text{m}$ . The area with bacteria shows a "shadow" in the magnetic phase image as bright (dark) stripes appear a little dark (bright), because of the distance between the tip and the magnetic substrate being increased by the thickness of bacterial layer  $h$ .

### b) Analysis of phase contrast

In the following discussion, the phase contrast  $\Delta\phi$  measured on a periodically patterned magnetic substrate quantitatively is supposed to reflect the film thickness after calibration. As seen in Figure 3.4c, the magnetic phase contrast from the two profiles of the lines marked with A and B in the magnetic phase image. The phase shift measured where bacteria are not present ( $\Delta\phi_A$ ) is almost constant on the imaged area, while the phase shift of the area covered with bacteria ( $\Delta\phi_B$ ) is significantly reduced correspondingly. Figure 3.4d

shows the functional relation between the phase contrast  $\Delta\phi_A$ ,  $\Delta\phi_B$  and  $z$  for different values of the tip-sample distance  $\Delta z$ , with  $z = \Delta z$  for  $\Delta\phi_A$  and  $z = \Delta z + h$  ( $h = 280$  nm measured from topographical image) for  $\Delta\phi_B$  respectively. Meanwhile, it indicates that the reduction of the contrast in the magnetic phase is corresponding to the increase of  $z$ .

The calibration curve is obtained from theoretical fit of  $\Delta\phi_A(z)$  data is reported in Figure 3.4d.  $\Delta\phi_B(z)$  data lie on the calibration curve for  $\Delta z$  in the range 70 – 300 nm, while a certain deviation is observed for greater values of  $\Delta z$ . Therefore, the phase contrast  $\Delta\phi$  measured on a thin film on a periodically patterned magnetic substrate by MFM can be used to evaluate the film thickness from some hundreds of nanometers up to microns after calibration of the  $\Delta\phi$  signal versus  $z$ .

Compared with the theoretical fitting curve in Figure 3.3d, Figure 3.4d states the high similarity between  $\Delta\phi_A$  and  $\Delta\phi_B$  (the phase contrast of line A and B). Here, the calibration should be performed at different values of  $\Delta z$  (tip-sample distance), whose variation range is commonly adopted in MFM measurement of film thickness.

It is worth noting that magnetically coated tips are generally conductive, so the tip can sense electrostatic force also, the gradient of such nonmagnetic force will attribute to the absolute phase in the magnetic image. Theoretically nonmagnetic signals can be partially separated from the purely magnetic ones, but the procedure requires extra experiments [162]. In addition, subsequent MFM scanings at different  $\Delta z$  require quite a long time to perform, during which drift and abrupt modifications in experimental conditions may occur, limiting the quantitative use of MFM data. Therefore, the proposed phase difference MFM (PD-MFM) technique could overcome some major limitations that prevent accurate quantitative measurements by standard MFM, such as the artifacts induced by nonmagnetic long range forces acting on the tip.

### **c) Example of quantitative measurement**

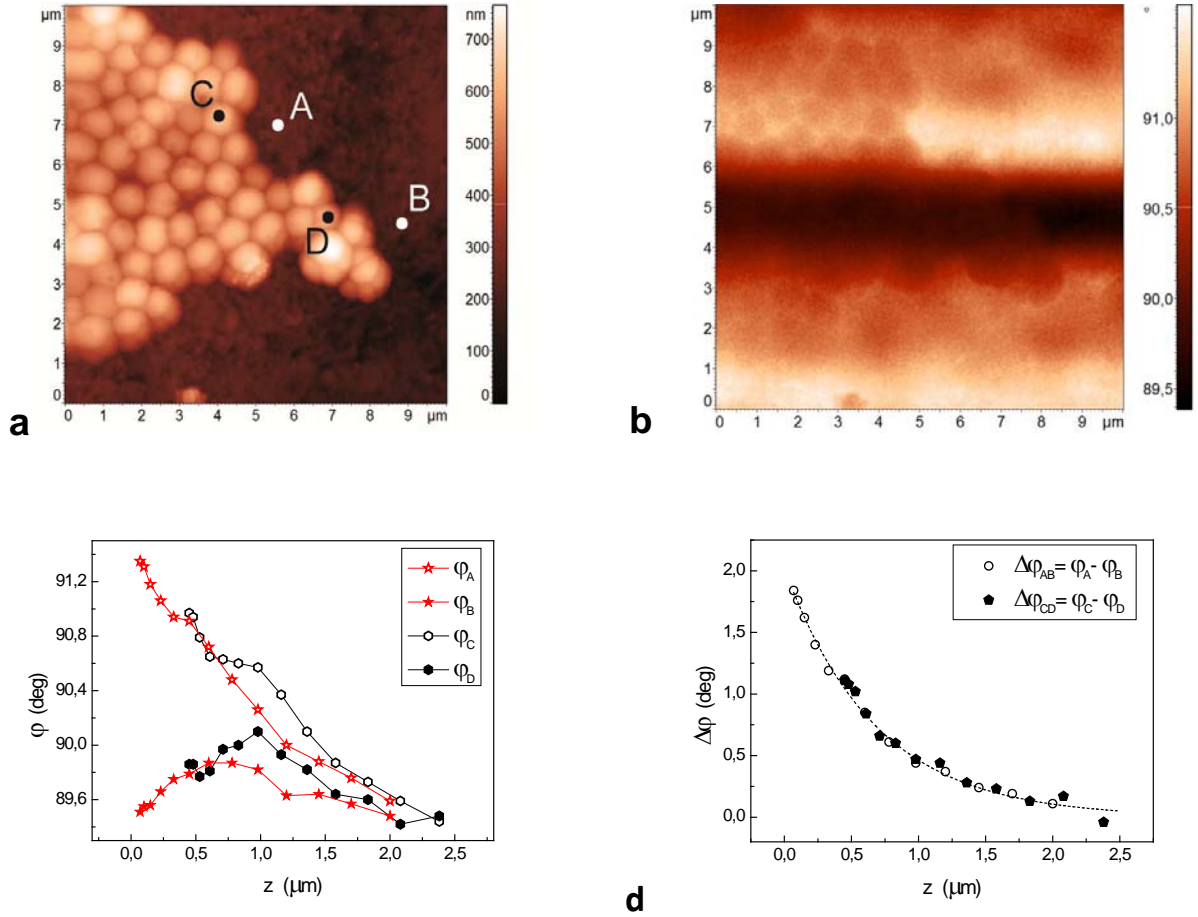


Figure 3.5 MFM characterization of a part of the *S. aureus* colony on floppy: (a) detailed topographical image; (b) corresponding phase image with  $\Delta z = 100.5$  nm; (c) the absolute phase of the s A, B, C, D as a function of  $z$ ; (d) phase contrast as a function of  $z$  (symbols) together with the theoretical fit of  $\Delta\varphi_{AB}$  versus  $z$  using Eq. (3.6).

The PD-MFM technique could accurately measure the thickness of soft thin film, though noisy signals may come from the gradient of nonmagnetic forces. As an example, Figure 3.5a shows a detailed bacteria colony, the corresponding magnetic phase image with  $\Delta z = 100.5$  nm is shown in Figure 3.5b. Two close s A and C are selected in Figure 3.5a in correspondence of a maximum of the magnetic phase, while A was on a location without bacteria and C was on a location with height of bacterium  $h = 380$  nm. Similarly, s B and D were selected in Figure 3.5a in correspondence of a minimum of the phase, while B was on a location free from bacteria and D was on a location where a second bacterium with the same height  $h = 380$  nm. The values of the absolute phase in such four s are reported in Figure 3.5c. But it is hard to retrieve any quantitative information about sample thickness with the absolute values of phase, since of the presence of electrostatic forces. The measurements of zeta potential obtain  $\zeta = -33.6 \pm 0.5$  mV for viable and  $\zeta = -33.6 \pm$

0.4 mV for sterilized bacteria, which indicate that sterilization does not alter the surface charge properties of *S. aureus* cells. Thus, electric charges cannot be excluded also on dried samples. Nevertheless, electrostatic interaction between the tip and the samples is expected to be almost constant for two close s free from bacteria (like s A and B), as well as for two similar and close bacteria (like s C and D). By calculating the difference of the phase contrast  $\Delta\phi$  such a constant term mentioned above can be canceled out. This is definitely demonstrated in Figure 3.5d, which reports the difference  $\Delta\phi_{AB}$  between the values of the phase recorded at s A and B and shows a exponentially functional relation between  $\Delta\phi_{AB}$  with  $z$ , as predicted by Eq. (3.6) that was used to obtain the fitting curve reported in Figure 3.5d. Meanwhile, the same decaying is observed for the difference  $\Delta\phi_{CD}$  between the values of the phase recorded at s C and D as a function of the tip-substrate distance  $z = \Delta z + h$ , where  $h = 380$  nm.

#### **d) The feasibility in thickness measurement**

The result above shows that in order to determine the thickness of sample, firstly calibration curve has to be obtained from the magnetic substrate by measuring  $\Delta\phi(z)$  and determining  $A$  and  $\xi_0$  from Eq. (3.6). Then,  $\Delta\phi$  is measured at certain  $\Delta z$  for the undetermined thickness film. Finally, the calibration curve is used to evaluate the film thickness from the values of  $\Delta\phi$  and  $\Delta z$  using Eq. (3.6) rewritten as

$$\phi = A_d \exp(-(\Delta z + h) / \xi_0) \quad (3.7)$$

Although analytically approximated expression of the diamagnetic properties of bacteria has been reported in Appendix B, it could be useful to analyze the data with a different approach. To this aim, the presence of diamagnetic matter with thickness  $h$  on the floppy could be described with an "equivalent" thickness  $\sigma h$  instead of the true thickness of the film in Eq. (3.7), where  $\sigma$  acts as an equivalent magnetic shielding constant. Thus, Eq. (3.7) can be rewritten as

$$\Delta\phi = A_d \exp(-(\Delta z + \sigma h) / \xi_0) \quad (3.8)$$

As an example, the  $\Delta\phi(z)$  data collected on the area free from bacteria can be fitted using Eq. (3.8) with  $h = 0$  in order to evaluate  $A_d$  and  $\xi_0$ . While  $\Delta\phi(z)$  data collected on the area with bacteria can be fitted using Eq.



(3.8) with the above estimated values of  $A_d$  and  $\xi_0$  and the value of  $h$  measured with AFM ( $h=280$  nm). Thus,  $\sigma = 1.01$  is evaluated, which results from the presence of the thickness of bacteria.  $\sigma < 1$  was also observed by repeating the analysis on other data on the same bacteria, that should be associated with the presence of paramagnetic materials. In summary, PD-MFM as a MFM-based technique can be used to accurately determine the thickness of thin films.

### 3.3.3 Further Consideration

#### a) Advantage of PD-MFM

Depending of a standard AFM instrumentation and expertise, PD-MFM is simple and does not require any additional tool. Disposing the measurement on the sample surface, MFM can be performed not only in air, but also it has been elucidated in liquid [153-164], which can be helpful to observe the *in vivo* growth of bacterial biofilms. In addition, the thickness of the film is not limited by the vertical range of the AFM. The measurable range of values of film thickness depends on  $\xi_0$ , the bigger  $\xi_0$ , the thicker the film that can be measured. Thus, relatively thick films can be explored using substrates with large values of spatial period  $\lambda$  of magnetic pattern.

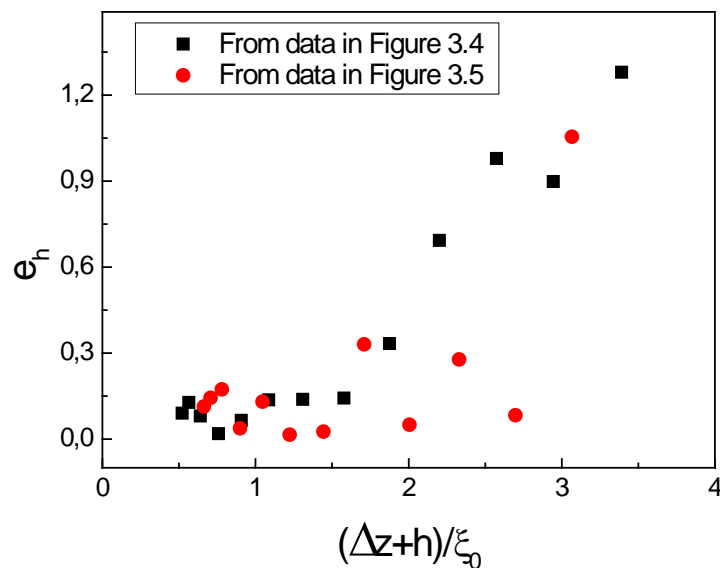


Figure 3.6 Functional relation between the relative error in the thickness determination  $e_n$  and the tip-substrate distance

$\Delta z + h$  normalized for the decay length  $\xi_0$ , calculated with data in Figure 3.4 - 3.5.

### b) Relative error $e_h$ in thickness measurement

In order to evaluate the accuracy of PD-MFM, the relative error  $e_h$  in the determination of film thickness can be calculated as  $e_h = |(h_{PD-MFM} - h)/h|$ , where  $h_{PD-MFM}$  is the thickness evaluated from Eq. (3.7) and  $h$  is the thickness obtained from the AFM topography profile. The value of  $h$  can be considered as the "true" thickness, because the accuracy in the measurements with AFM is much greater than that with PD-MFM. relative error is evaluated for different values of  $\Delta z$  with the two data sets accounted in Figure 3.4d and Figure 3.5d, the thicknesses of them are  $h=280$  nm and  $h=380$  nm correspondingly. Figure 3.6 reveals the values of  $e_h$  calculated from the two data sets as a function of the tip–substrate distance on the film  $(\Delta z+h)$ , which has been normalized by  $\xi_0$ . The error is acceptable for  $(\Delta z+h)/\xi_0 < 1.5$ , while it increases for  $(\Delta z + h)/\xi_0 > 1.5$ . This indicates that an acceptable precision of the method is obtained when the tip–substrate distance is not larger than  $\xi_0$ . That means the spatial period of the magnetic pattern limits both the measurable film thicknesses and the suitable values of lift height. As an example, supposing  $\Delta z = 100$  nm, the maximum value of  $h$  used in this study ( $\xi_0 \approx 680$  nm) is  $1 \mu\text{m}$ . The upper detection limit  $h_{max}$  of PD-MFM can be evaluated with at least one line of maximum and one of minimum of the magnetic phase detected in the MFM image. Standard AFM setups enable one to scan areas with maximum about  $L_{max} = 50\text{--}100 \mu\text{m}$  in  $x$  and  $y$  dimension. Therefore, the substrates can be applied with period  $\lambda = 2L_{max}$  of the magnetic pattern in the range from  $100 \mu\text{m}$  to  $200 \mu\text{m}$ , the decay length  $\xi_0$  is from  $16 \mu\text{m}$  to  $32 \mu\text{m}$  correspondingly. As mentioned above, the error in the determination of the film thickness is acceptable for  $(\Delta z+h)/\xi_0 < 1.5$ . Considering  $\Delta z$  in the range from  $50$  nm to  $100$  nm, the value of  $\Delta z$  can be neglected comparing with  $h$ . Thus  $h < 1.5\xi_0$  can be obtained and correspondingly the detectable maximum of film thickness is in the range from  $24 \mu\text{m}$  to  $48 \mu\text{m}$ . Therefore,  $h_{max}$  in this technique can be assumed in the range from  $25 \mu\text{m}$  to  $50 \mu\text{m}$ .

### c) Accuracy of PD-MFM measurement

The uncertainty of PD-MFM mainly depends on the feature of the periodically patterned magnetic substrates. As an example, it is observed that the absolute phase value of the floppy is not constant along the same stripe

of maxima (minima) and among different stripes of maxima (minima). In order to increase the accuracy of this technique during the measurement of the thickness of films, the phase values can be obtained by averaging those data along a line of maxima (minima). For the images of the magnetic substrate reported in Figure 3.1 with a tip-sample distance of 100.5 nm, a standard deviation of the mean values along a line of maxima (minima) of  $\sigma_\varphi = 0.052^\circ$  is observed. Thus, the standard deviation of the difference between maxima and minima is  $\sigma_{\Delta\varphi} = \sqrt{2} \sigma_\varphi = 0.073^\circ$ . The difference between the maxima and minima  $\Delta\varphi$  equals to  $1.64^\circ$ , this corresponds to a relative standard deviation  $\sigma_{\Delta\varphi}/\Delta\varphi = 4.5\%$ . From Eq. (3.7) the uncertainty in the determination of  $h$  is  $\sigma_h = \xi_0 \times \sigma_{\Delta\varphi}/\Delta\varphi = 30$  nm can be found. Even though this value suggests that the presence of films thicker than 60nm can be detected, with the commonly assumed definition the limit of detection may be estimated as high as  $3 \times \sigma_h = 90$  nm. Thus, we may reasonably assume that our technique allows us to reveal the presence of films on the magnetic substrates with the minimum thickness in the range from 50 nm to 100 nm. In order to increase the accuracy, more suitably realized magnetic substrates may allow one to decrease the limit of detection down to a few nanometers.

### 3.4 Conclusion

In conclusion, PD-MFM, a MFM-based technique that allows one to accurately measure the thickness of soft films deposited on periodically patterned magnetic substrates is demonstrated. Standard floppy disks were used to obtain the periodically patterned magnetic substrates, while bacterial cells of *Staphylococcus aureus* were cultivated for the layer formation with limited lateral dimensions. The thickness is deduced by comparing the phase contrast in magnetic phase images acquired by MFM on biofilm surface with those obtained on the magnetic substrate for different values of the tip-sample distance. The accuracy of the technique depends on the spatial period and the uniformity of the magnetic domains of the periodically patterned magnetic substrates. Disposing suitable substrates applied, thickness of films ranging from tens of nanometers to about 50 microns can be obtained. With the detailed discussion on the relationship between the phase contrast and topography of investigated biofilms, the feasibility of this MFM-based technology in detecting the soft thin films is demonstrated.

## Chapter 4

# Magnetic Force Microscopy for Vesicular Systems

Niosomes are typical non lipidic vesicles functionalized with drugs and magnetic nanoparticles, presently under investigation for actively targeted drug delivery. In this chapter, a MFM based approach is presented for evaluating the dimension of superparamagnetic nanoparticles encapsulated in niosomial systems. The results obtained have been included in poster presentation for a conference and in a paper presently in preparation. The chapter is organized as follows. At first, we give some background and details of the synthetic methods, as well as of the techniques employed for the characterization of vesicles. Then, morphological properties and the corresponding magnetic response of the investigated vesicular system are described using AFM/MFM measurements. The results and analysis of the magnetic characterization are illustrated also to quantify MNPs internalized into single vesicle.

### 4.1 Introduction

During the past few decades, many efforts have been made to improve disease diagnosis and therapy. Lack of clinical efficacy and side-effects of chemotherapeutic agents are caused mainly by their low targeting, insufficient cellular drug uptake or local drug concentration. Various nanoformulations have been developed for the experimental and clinical delivery of therapeutic and diagnostic agents, to improve their site targeting. Commonly, the application and therapeutic outcome of a nanoformulation are determined by nanocarrier properties, while the properties of loaded molecules or reagents are negligible since they are low in quantity and can be isolated or surrounded by carrier matrices [170].

#### a) Common nanoparticulate delivery system

The most commonly used diagnostic/therapeutic nanoformulations include nanoparticulate delivery systems such as liposomes, micelles, dendrimers, nanospheres, nanocapsules, and inorganic nanoparticles (NPs) - e.g.,

gold NPs, superparamagnetic iron-oxide (SPIO) nanocomposites, carbon nanotubes, and quantum dots and macromolecular delivery systems such as antibody-drug conjugates (ADC) and drug-polymer conjugates (e.g., PEG-protein conjugates and PEG-siRNA conjugates) [171]. Besides their nanoscopic scale [172] the architecture and components of nanocarriers/nanoformulations provide extra opportunities for engineering and modification, aimed at controlling their biological properties in a desirable fashion to allow them to perform simultaneously various therapeutic or diagnostic functions. These modifications result in the increased stability, long blood circulation half-life, higher bioavailability, enhanced target ability, as well as the minimization of undesirable protein binding and biodistribution, immunogenicity, and other side-effects [173].

#### **b) Magnetic surfactant vesicles**

Among the delivery systems, surfactant vesicles - known as niosomes or non-ionic surfactant vesicles (NSVs) - have recently acquired growing scientific attention as an alternative potential drug delivery system to conventional liposomes. Liposomes with an internal ferromagnetic iron oxide shell entrapped magnetic particles or lipid-bound paramagnetic ions as magnetic target carrier particles can be used for cancer therapy, magnetic drug targeting (drug entrapped in the liposome lumen), bioanalytics (analytical target signal, imaging), and biophysical experiments. Magnetic liposomes of 80–250 nm size can be used for targeting *in vivo*, i.e., magnetic drug targeting, and magnetic radiation targeting for X-rays, neutrons, and isotopes. Vesicles are the highly investigated delivery and targeting devices designed, the self-assembly of non-ionic surfactants as new generation of liposomes into vesicles was firstly reported in the seventies by researchers in the field of cosmetics [174].

#### **c) Niosomes**

Niosomes are analogous to liposomes and can be prepared following the same procedures, under a variety of conditions, leading to the formation of unilamellar or multilamellar vesicular structures [175]. When compared to phospholipid-based vesicles, NSVs have several advantages such as greater stability, which reduces the care required in handling and storage and results in lower costs, which make them attractive for

industrial applications both in the field of pharmaceuticals and cosmetics [176]. Moreover niosomes, like liposomes, are capable of encapsulating both hydrophilic and lipophilic drugs [177-178]. The encapsulation of drugs in niosomes can minimize drug degradation and inactivation after administration, prevent undesirable side effects, and increase drug bioavailability and targeting to the pathological area.

#### **d) SPIO nanocomposites---interesting nanomaterials for biomedical application**

As far as nanomaterials are concerned, superparamagnetic iron oxides (SPIO) nanocomposites are particularly interesting because of the combination of excellent magnetic properties and good biocompatibility. For in vivo imaging, the existence of the SPIO nanocomposites influences the precession of water hydrogen nuclei within an applied magnetic field, so the SPIO nanocomposites can be used as a superparamagnetic or negative contrast agent. On the other hand, SPIO labeling of drug carriers can target the antitumor drugs to the tumor area under an external magnetic field, resulting in an in vivo tissue-specific targeting and controlled release of drugs. Therefore, the SPIO nanocomposites have been widely used in magnetic resonance imaging (MRI) [179-183], hyperthermia cancer therapy under alternating magnetic field [184-187], and external magnetic targeting and controlled release of drugs [189-191]. In order to confer colloidal suspendability to the particles, additives, typically hydrophilic polymers are added during the particle formation process, which passivate the nanocrystal surface and protect against particle aggregation [192].

#### **e) Importance of characterization of nanocarriers in SPIO theranostic systems**

To design and construct an ideal multifunctional SPIO theranostic system, a fundamental aspect in pharmaceutical nanotechnology lies in the characterization of nanocarriers. In particular dimensions, shape and entrapment efficiency of nanocarriers must be deeply evaluated. It is well known that dimensions [193] and shape [194] can interfere with biodistribution, toxicity and release kinetic of the carrier while the evaluation of entrapment efficiency is important to assure a good amount of entrapped drug in the sample. In

particular, as far as the entrapment efficiency is regarded, it is important to determine the overall amount of Fe entrapped into the NSVs sample, which gives an average macroscopical information. Nevertheless, it would be more desirable to evaluate Fe amount in each single nanocarrier, which would give also information about the uniformity of the sample preparation and encapsulation of SPIO nanomaterials.

#### **f) Varieties of characterization methods used to detect Fe amount**

As for the determination of the global content of Fe, potassium hexacyanoferrate (II) [195] or 1,10-phenantroline [196] methods are available. In addition, mass spectrometry (ICP-MS or optical) or atomic absorption can be employed [197]. Nevertheless, all these methods give information about the mean Fe concentration in the whole sample. Therefore, the content of the single nanocarrier is not accessible, and thus the uniformity of SPIO nanomaterials cannot be evaluated. In addition, even the mean value of Fe amount in each NSV can hardly be inferred due to the difficulties in the evaluation of the effective number of NSVs in the sample. Conversely, transmission electron microscopy (TEM) allows one to visualize the vesicular systems with nanometrical spatial resolution, but the sample are easily damaged as a result of the drying steps and the analysis in vacuum. Cryogenic TEM allows one to overcome such limitations and have been used to visualize with nanometrical spatial resolution NPs embedded in vesicular systems (in their core and/or in the bilayer) [198-199], but the sample preparation is not straightforward. Scanning electron microscopy (SEM) allows one to visualize the exterior of the vesicles and possibly to evaluate the presence of encapsulated NPs formed by atoms with atomic weight higher than that of the atoms of the bilayer using the backscattered electrons, but the sample preparation is not straightforward. Finally, environmental SEM (ESEM) allows the imaging of vesicles in hydrated state [200], but the possibility of imaging the interior of the vesicles is also in this case a major issue. For the sake of completeness, it should be mentioned that both TEM and SEM associated to energy dispersive X-ray (EDX) analysis enable one to verify the presence of Fe atoms in the vesicular system. Nevertheless, data obtained from EDX spectra are relative and it is difficult to obtain quantitative information about the amount of Fe into each vesicle, while EDX elemental mapping does not possess the resolution

required to evaluate the diameter of NPs entrapped into vesicles.

#### **g) The potential of using AFM/MFM to study vesicular systems**

Therefore, innovative approaches are required which give quantitative and local information about the presence of SPIO NPs entrapped in vesicular systems. Such methodologies should require a relatively straightforward sample preparation, in order to analyze a statistically significant number of NSVs, and could be possibly extended to the analysis of SPIO/NSVs systems in liquid environment. Atomic force microscopy (AFM) has been demonstrated to be a versatile technique for the high resolution imaging and characterization of vesicular systems such as liposomes, niosomes, and polymerosomes [201-202]. Firstly, AFM requires relatively straightforward sample preparation. Images can be performed in air as well as in liquid environment [203-206], at room or variable temperature [179]. Moreover, probing the sample with the AFM tip allows one to quantitatively study vesicles formation, morphology, size distribution, as well as their surface elastic and adhesives properties [207-212]. Based on AFM, magnetic force microscopy (MFM) takes advantage of the use of magnetically coated tips to analyze the magnetic properties of the sample simultaneously to its topography. MFM has been used to study magnetic materials such as recording media, MNPs on flat surfaces and on the surface of cells [213], and subsurface magnetic NPs [214]. Nevertheless, MFM has never been used to study vesicular systems embedding MNPs, either qualitatively or quantitatively. As for the latter, the difficulty of modeling the tip-sample interaction severely limits the use of MFM for quantitative and enough accurate measurements. Thus, relatively few works are reported in which quantitative deductions from MFM analysis have been attempted [215].

In this study vesicular system incubated with magnetic nanoparticles was detected at the first time, this research is expected to understand the localization and space distribution quantitatively induced by the technique based on MFM. In the following, the experimental material and technique will be introduced.

## **4.2 Materials**

The thin layer evaporation method was used to prepare non-ionic surfactant vesicles. Briefly, polysorbate 20



(15mM), cholesterol (15mM) and BDP were dissolved in a round bottom flask using 2 ml of a chloroform/methanol mixture (3:1 v/v). The solvent mixture was vacuum evaporated and the resulting dried film was hydrated with 5 ml 0.01 M pH 7.4 Hepes buffer solution. The dispersion was vortexed for 5 min and then sonicated for 5 min at 60°C using a tapered microtip operating at 20 kHz at an amplitude of 16% (Vibracell-VCX 400 Sonics, USA), thus achieving BDP-loaded unilamellar non-ionic surfactant vesicles.

Two different BDP concentrations, i.e. 50 mg/ml (sample BDP-50) and 0.4 mg/ml (BDP-0.4), were used in this investigation for the vesicle preparation. The first concentration led to the maximum possible amount of drug entrapped within the NSVs, while the second concentration led to an amount of entrapped drug similar to that actually present in the most common commercial products. Unilamellar vesicles were obtained from a non-ionic surfactant/MNPs aqueous dispersion (Hepes pH 7.4) by means of the "film" method. Sp20 concentration in the samples was always remarkably above its CMC (in water at 25°C: Span 20 = not detectable). For this purpose, Sp20, Chol (15mM: 15mM) and lipophilic MNPs were dissolved in a CHCl<sub>3</sub>/CH<sub>3</sub>OH (3:1) mixture in around bottomed flask. After evaporation of the solvents, the dried film was hydrated by addition of 5 mL (0.01 M) Hepes pH 7.4 solution. The dispersion was vortexed for about 5 min and then sonicated for 5 min at 60°C using a tapered microtip operating at 20 kHz at an amplitude of 16% (Vibracell-VCX 400-Sonics, USA). In order to separate MNPs-loaded vesicles from untrapped substances, for the evaluation of entrapment efficiency, the untrapped material was eliminated by filtration with 1.2 µm filter and then dialysis method.

### **4.3 Magnetic Force Microscopy of Magnetic Nanoparticles**

AFM/MFM analysis has been performed using a commercial AFM apparatus (Solver, NT-MDT, Russia) equipped with cantilever with a 40 nm thick CoCr magnetic coating (MESP-RC, Bruker Inc.). MNPs, empty niosomes and niosomes incorporating MNPs were prepared for AFM/MFM analysis by depositing a drop of properly stored sample on cleaned single crystal Si substrates and waiting until sufficient drying. AFM/MFM characterizations were performed in air at room conditions. Post experiment image analysis was limited to the subtraction of the average plane and, when necessary, to the polynomial fitting of the profile along the

"slow" scan axis. At first we make a study of the magnetic nanoparticles which are used with vesicular system.

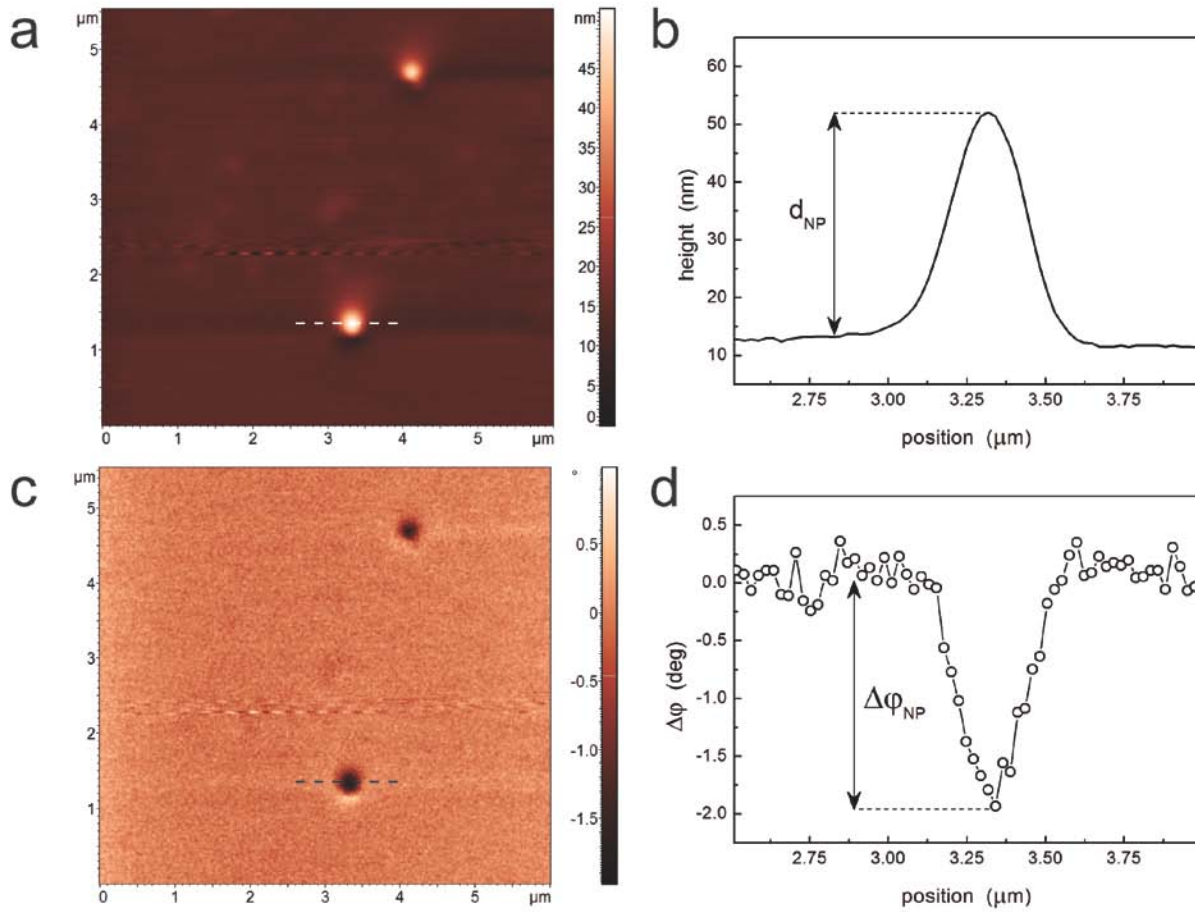


Figure 4.1 Example of AFM/MFM characterization of SPIO NPs on a Si flat substrate:(a) topographical reconstruction of an area featuring two NPs and (b) height profile of a NP, corresponding to the dashed line in (a), from which the diameter of the NP ( $d_{\text{NP}}$ ) is evaluated; (c) corresponding MFM phase image and (d) phase shift ( $\Delta\phi$ ) profile, corresponding to the dashed line in (c), from which the MFM phase shift of the NP ( $\Delta\phi_{\text{NP}}$ ) is evaluated.

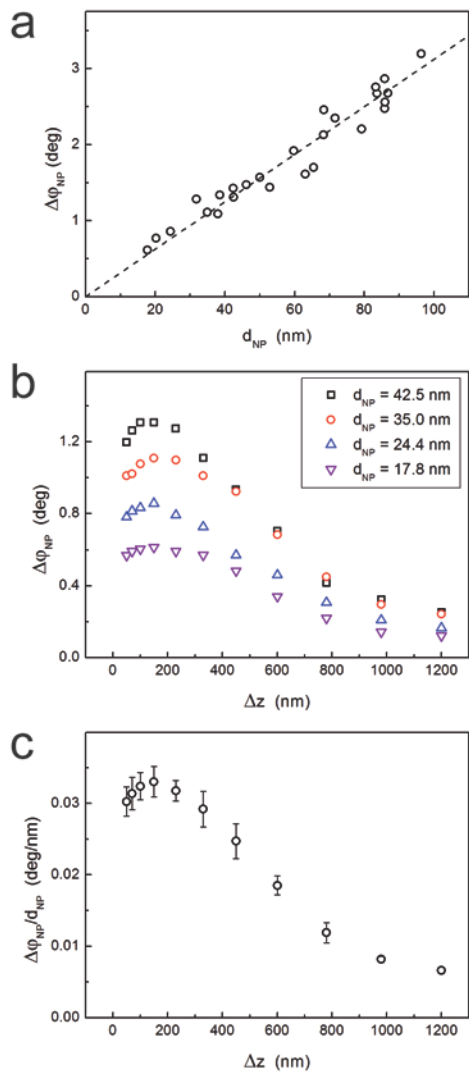


Figure 4.2 Calibration curves from MFM images of SPIO NPs: (a) NPs phase shift ( $\Delta\phi_{NP}$ ) as a function of the NPs diameter ( $d_{NP}$ ) at fixed tip-sample distance  $\Delta z = 100.5$ nm revealing a linear dependence between  $\Delta\phi_{NP}$  and  $d_{NP}$ ; (b)  $\Delta\phi_{NP}$  as a function of  $\Delta z$  for four NPs with different  $d_{NP}$ ; (c) calibration curve obtained by evaluating the  $\Delta\phi_{NP}=d_{NP}$  ratio from data in (b) as a function of  $\Delta z$ .

The use of MFM for the qualitative visualization of MNPs is widely reported in literature. Nevertheless, a few works have been reported where MNPs parameters are quantitatively deduced, due to the lack of comprehensive models of the tip-sample interaction. Therefore, in this work we chose a phenomenological approach to obtain quantitative information from the MFM images. To this aim, at first MNPs were drop-casted on a Si substrate and characterized with MFM. Figure 4.1a shows the topographical reconstruction of an area of such a sample where two MNPs are visible. Since the casting on the substrate

does not lead to any deformation of the stiff MNPs, the diameter of each MNP ( $d_{\text{NP}}$ ) can be evaluate from the profile of the line corresponding to the top of the MNP, as shown in Figure 4.1b. Simultaneously to the morphology, the MFM image of the individual nanoparticle is acquired. As an example, Figure 4.1c shows the MFM image of the area obtained using  $\Delta h = 100.5$  nm. In correspondence of the same profile, the phase shift relative to the MNP ( $\Delta\phi_{\text{NP}}$ ) is measured (Figure 4.1d). Due to the lack of comprehensive theoretical models of the interaction between the AFM tip and the MNPs, we used a phenomenological approach to quantitatively relate  $\Delta\phi_{\text{NP}}$  to  $d_{\text{NP}}$  and to the distance between the tip apex and the top of the MNP ( $\Delta z$ ). Figure 4.2a shows the values of  $\Delta\phi_{\text{NP}}$  measured at fixed value of  $\Delta z$  (note that in this case  $\Delta z = \Delta h$ ) on different NPs as a function of  $d_{\text{NP}}$ . Data are well described by a linear relation, instead of the cubic one generally assumed in literature. Although further study is needed to understand the  $\Delta\phi_{\text{NP}}(d_{\text{NP}})$  dependence, it can be at least partially rationalized considering that the effective distance between the apex and the center of the NP linearly increases with  $d_{\text{NP}}$  as the latter is not negligible with respect to the tip-sample distance. To investigate the relation between  $\Delta\phi_{\text{NP}}$  and  $\Delta z$  the same area of the MNPs sample has been imaged by MFM at different values of  $\Delta z$ . Figure 4.2b reports the values of  $\Delta\phi_{\text{NP}}$  as a function of  $\Delta z$  measured for four MNPs with different  $d_{\text{NP}}$ . To retrieve a phenomenological calibration curve,  $\Delta\phi_{\text{NP}}$  data have been divided by  $d_{\text{NP}}$  for each value of  $\Delta z$  and averaged, thus obtaining the curve reported in Figure 4.2c. Such a curve was eventually used to evaluate  $d_{\text{NP}}$  internalized in niosomes, as described below.

#### **4.4 Magnetic Force Microscopy of Niosomes**

After discussion the magnetic nanoparticles, we have a study on niosomes as vesicular systems. The measurements carried out by DLS show that dimensional changes occur in Sp 20 vesicles loaded with MNPs respect to empty ones. In Sp20 vesicles the insertion of lipophilic MNPs in surfactant bilayer is responsible of a slight increase in vesicle dimension. Apart from providing hydrodynamic diameters and potential values, DLS provides also valuable information on the homogeneity of the suspension. A single sharp peak in the DLS profile implies the existence of a single population of scattering particles. DLS and PDI (polydispersity index) measurements indicated that the empty and MNPs loaded vesicles showed a significant yield of

homogeneous vesicular structures. The empty and MNPs loaded Sp20 vesicles show higher potential (in absolute value); it is important because allow to foresee the stability of the prepared formulations. A high negative value of potential is important in preventing aggregation. It has been reported that a physically stable nanosuspension solely stabilized by electrostatic repulsion will have a minimum potential of 30mV. The Fe entrapment efficiency data show a good capability of the analyzed vesicle of entrap lipophilic MNPs. MNPs show a limited value of entrapment efficiency, probably due to the higher volume occupied by the aqueous core respect to the lipophilic bilayer.

#### **4.4.1 Dynamic Light Scattering**

Dynamic light scattering (DLS) was used to determine mean size and size distribution of non-ionic surfactant vesicles. The vesicle dispersions were diluted 100 times with the same buffer used for their preparation to avoid multiscattering phenomena. Buffer solutions used for dynamic light scattering experiments were filtered through 0.45  $\mu\text{m}$  cellulose filters to eliminate dust particles. Vesicle mean size and size distribution (polydispersity index, PDI) were measured at 25°C using a Malvern Nano ZS90 light scattering apparatus (Malvern Instruments Ltd., Worcestershire, UK) at a scattering angle of 90.0°. The same apparatus was used for the evaluation of potential of vesicles, which were appropriately diluted (1:10) in distilled water at 25°C. The laser Doppler anemometry was used and hence the electrophoretic mobility of non-ionic surfactant vesicles was measured. The potential value was calculated from the electrophoretic mobility in the Smoluchowsky approximation. Reported data represent mean of the potential and of the hydrodynamic diameter for the surfactant vesicles. Results of DLS experiments are given as the average values obtained using samples from three different batches standard deviation (SD).

#### **4.4.2 Entrapment Efficiency Measurement**

Fe entrapment efficiency (Fe e. e.) within nonionic surfactant vesicles was determined using inductively coupled plasma mass spectrometry (ICP-MS) on purified MNPs. Samples were transferred into TFM vessels and digested by means of a microwave oven (Ethos, Milestone, FKV, Sorisole, Bergamo, Italy) equipped

with a probe for the temperature control. The digestion mixture was constituted of 2 mL of H<sub>2</sub>O ultrapure (up), 4 ml of HNO<sub>3</sub> 65% (v/v) (Merck, Darmstadt, Germany), 0.5 mL of HCl and 1 mL of H<sub>2</sub>O<sub>2</sub> 40% (v/v) (Merck, Darmstadt, Germany). The digestion programme was preceded by a soft pre-digestion treatment of the samples in order to avoid any strong reaction during the final dissolution process. After cooling, the digested solutions were quantitatively transferred in 50 mL Falcon tubes by adding high purity deionized water up to 20 mL. These solution was further diluted (1 : 9) before the instrumental analysis. Measurements were performed by means of a dynamic reaction cell (DRC) ICP-MS (Elan DCR II, Perkin Elmer SCIEX, Norwalk, CT, USA) operating in DRC mode with ammonia as reaction gas (purity of 99.999%) so as to overcome the likely interferences on the Fe determination. The cell parameters were the following: gas flow = 0.6 mL/min and RPq = 0.6. <sup>56</sup>Fe was the isotope used for quantification purpose with external calibration approach. Fe e.e. was calculated as the ratio between the mass of the incorporated Fe and that of the Fe used for vesicle preparation. Results are the average of three different batches SD.

#### 4.4.3 Transmission Electron Microscopy

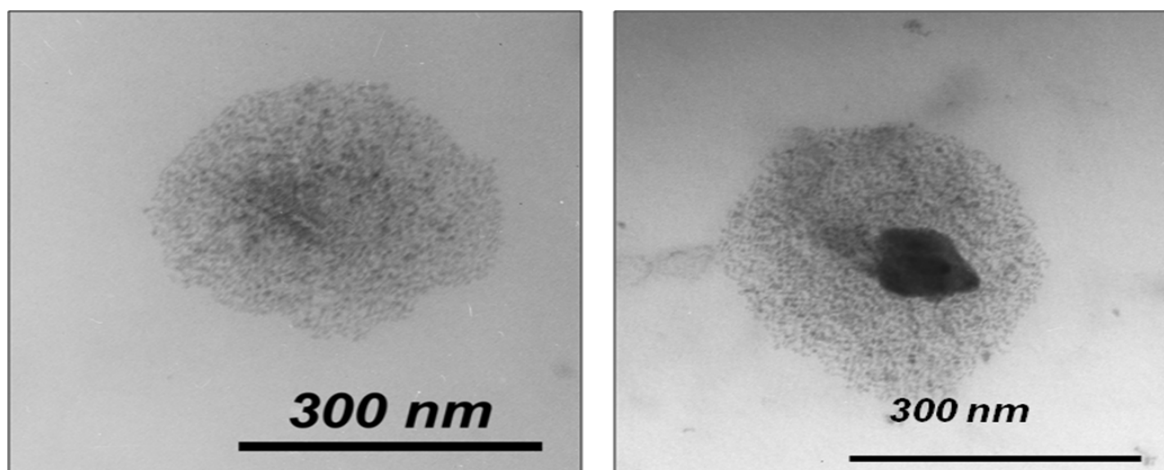


Figure 4.3 TEM images of niosome: left) empty niosome without MNPs; right) niosome containing a MNP.

The samples were observed at nanometer scale using transmission electron microscopy at about 80 kV and were deposited on TEM holder by drop casting of water mixture solution containing niosomes with MNP and niosomes alone. TEM images in Figure 4.3 reveal morphology of vesicles with diameter of around 300nm. The image (right) clearly shows magnetic nanoparticles of dark contrast embedded into niosome

with 100 nm in size. In order to study the dimension of the nanoparticles integrated in the vesicle MFM technique have been applied. The following research is going to detect magnetic nanoparticles internalized in individual vesicle using MFM qualitatively and quantitatively.

#### 4.4.4 Magnetic Force Microscope Imaging Analysis

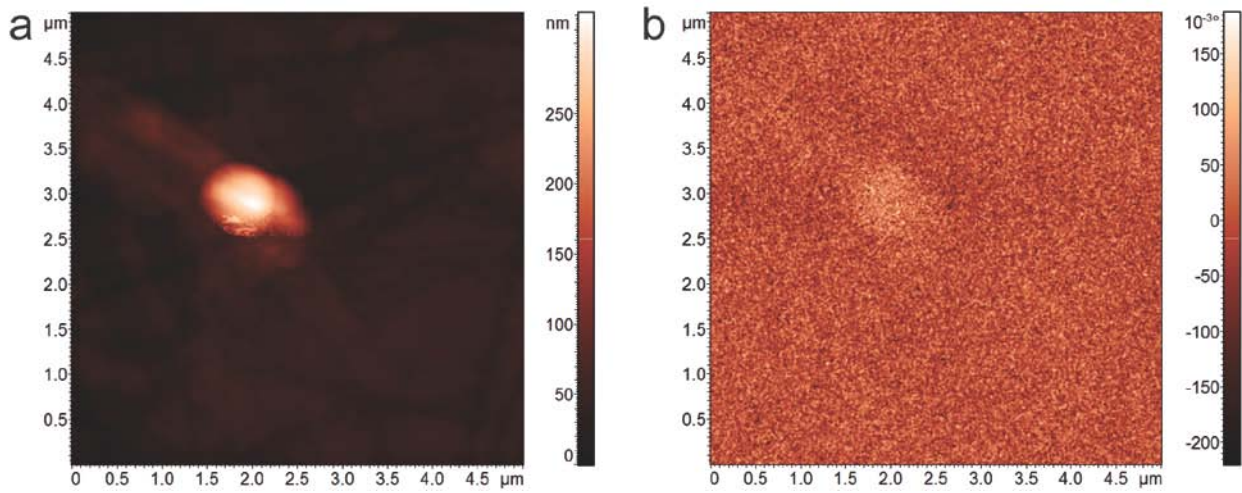


Figure 4.4 AFM topography (a) and MFM phase shift image (b) of an empty niosome, the latter revealing a small positive phase shift in correspondence of the niosome.

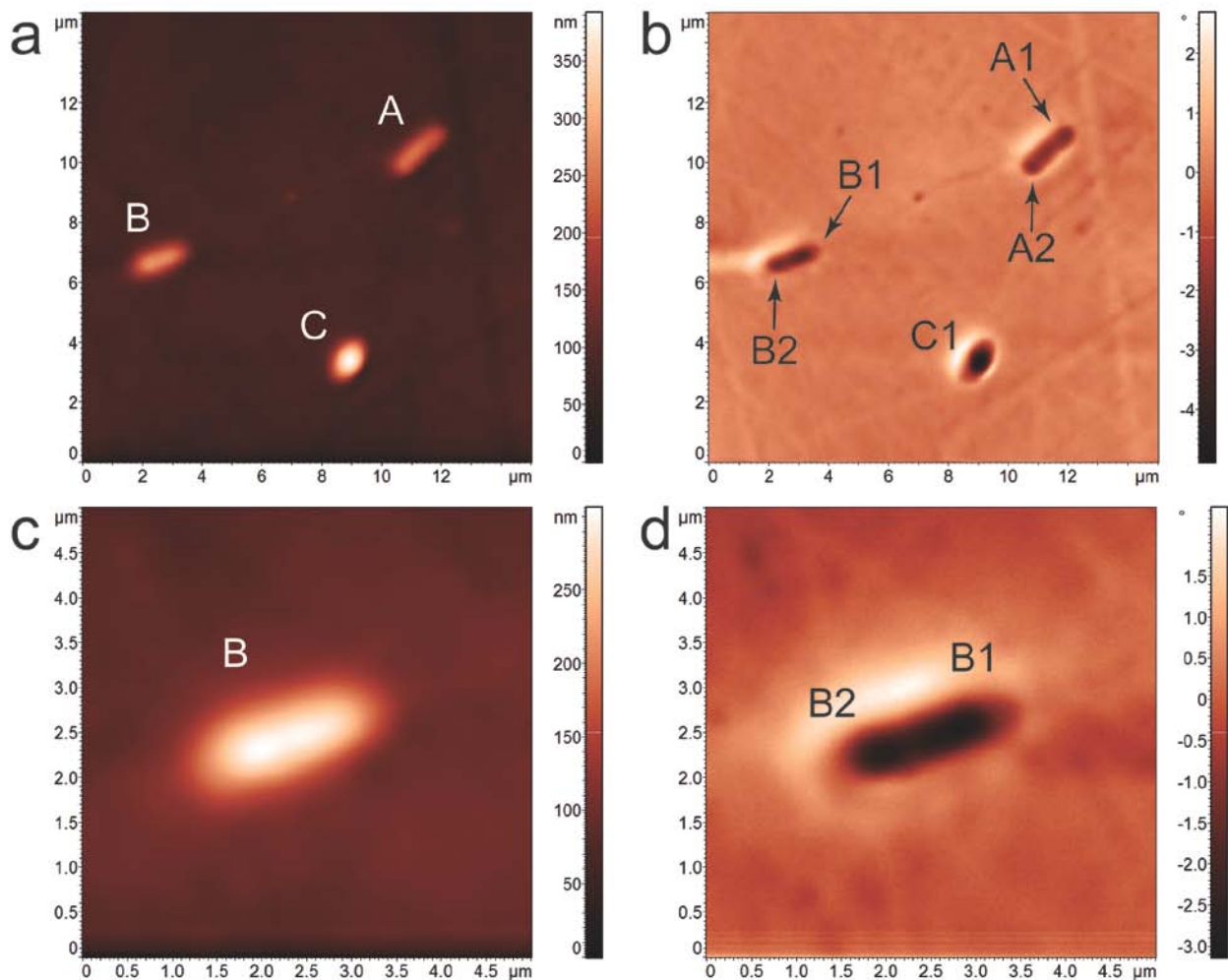


Figure 4.5 AFM topography (a) and corresponding MFM phase shift image (b) of three vesicular systems (labeled with A, B and C, respectively) encapsulating SPIO NPs, two of them composed by two distinct niosomes (labeled with A1, A2, B1, and B2, respectively). AFM topography (c) and MFM phase shift (d) of one of the B vesicular system.

Figure 4.4a shows a typical AFM image of an empty niosome. The size of niosome is about 300 nm, which is in agreement with those visualized using TEM in Figure 4.3. In the corresponding MFM image reported in Figure 4.4b, the vesicle is associated to an almost negligible positive phase shift  $\Delta\phi_v$  of about  $50 \times 10^{-3}$  deg, which could indicate an interaction between the tip and the vesicle slightly less attractive (or more repulsive) than that between the tip and the substrate. Analogous characterization has been performed on niosomes containing MNPs. In some cases, MFM images of vesicles showed positive values  $\Delta\phi_v$  not higher than 0.2 deg analogous to those observed in empty niosomes, thus indicating the presence of empty vesicles in the sample containing MNPs. Conversely, several niosomes have been observed the MFM images of which



show negative values of  $\Delta\phi_v$  as high as some degrees, such a contrast indicating the presence of a significant attractive interaction between tip and vesicles. As an example, Figure 4.5a shows an area of the sample where three aggregates of niosome are visible, marked with A, B and C, respectively. They're not spherical shapes indicate that they result from the coalescence of different adjacent niosomes, induced by the partial dehydration in presence of the substrate. In the corresponding MFM image, reported in Figure 4.5b, a marked phase contrast between the vesicles and the substrate is visible. This reveals a significant increase of tip-sample attractive force in correspondence of the niosomes (negative phase shift) with respect to the substrate, suggesting the presence of MNPs into the vesicles. As an example, the closer view of vesicle B reported in Figure 4.5c (topography) and Figure 4.5d (corresponding MFM phase image) suggests that vesicle B is the result of the coalescence of two separated vesicles (namely, B1 and B2) each containing a significant amount of MNPs. Similar considerations lead to the identification of the two 'original' vesicles forming the system A (namely, A1 and A2). Conversely, vesicle C has a roughly circular shape that may indicate that it is either a singular vesicle or the result of a coalescence process among different vesicles already completed and, therefore, vesicle C is considered in the following as a single vesicle.

Table 4.1 Experimentally determined values of the vesicle height ( $h_v$ ) and the phase shift in the magnetic image ( $\Delta\phi_v$ ) with the corresponding calculated values of effective diameter of the incorporated MNPs ( $d_{NP}^{eff}$ ) for the niosomes visualized in Figure 4.4.

Vesicle	$h_v$ (nm)	$\Delta\phi_v$ (deg)	$d_{NP}^{eff}$ (nm)
A1	142	2.24	$69 \pm 5$
A2	160	2.23	$68 \pm 5$
B1	171	2.92	$89 \pm 6$
B2	193	2.64	$81 \pm 6$
C	318	4.90	$153 \pm 8$

## 4.5 Quantification of MNPs into Niosomes

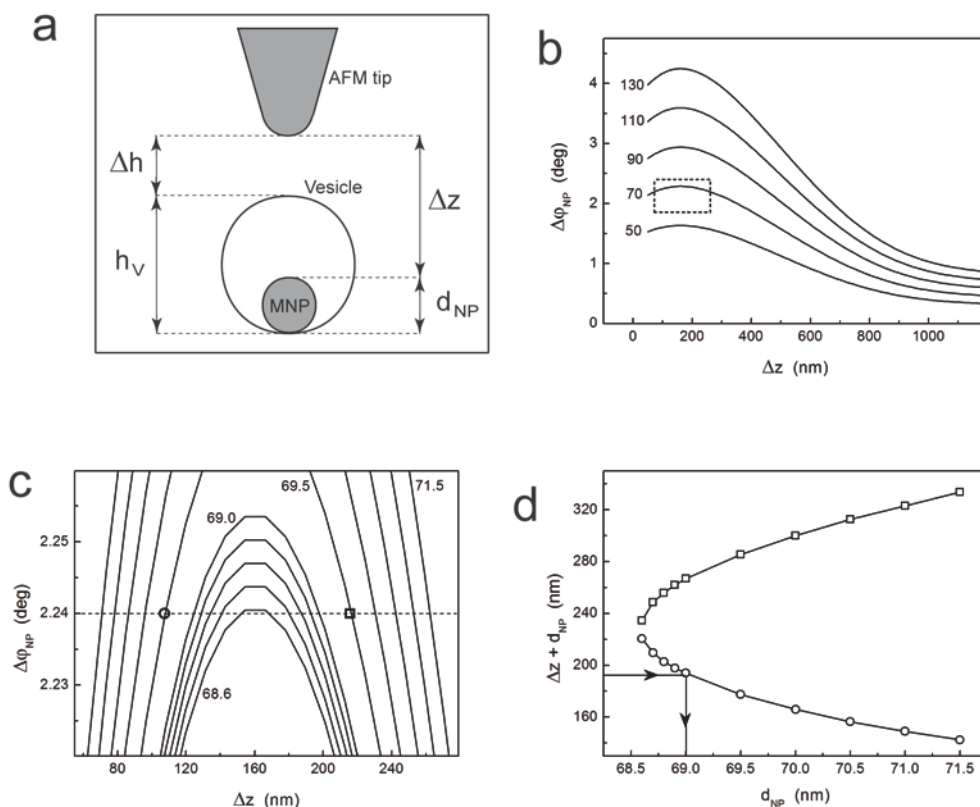


Figure 4.6 (a) Sketch illustrating the proposed model for analyzing MFM data: the magnetic nanoparticle (MNP) with diameter  $d_{NP}$  is at the bottom of the vesicle with height  $h_v$ , the image is acquired at lift height  $\Delta h$  and the distance between the tip apex and the top of the MNP is  $\Delta z$ . (b) Family of curves  $\Delta\phi_{NP}$  versus  $\Delta z$  calculated for values of  $d_{NP}$  ranging from 50 to 130 nm. (c) Detail of the region in the dashed rectangle in (b): in correspondence of the measured value of  $\Delta\phi_{NP}$ , two values are obtained on each curve (open circle and open square, respectively). (d) Values of  $\Delta z + \Delta\phi_{NP} = \Delta h + h_v$  versus  $d_{NP}$  calculated in correspondence of  $\Delta\phi_{NP}$  in (b): the arrows indicate how the diameter of the NP incorporated into the niosome ( $d_{NP}$ ) is inferred from the  $\Delta h + h_v$  measured value.

In order to quantitatively determine the amount of MNPs in the vesicles, AFM/MFM images are analyzed using the calibration curves reported in Figure 4.2. As an example of application of the procedure, the analysis of vesicle A1 is described in details. The height of the vesicle  $h_v$  is evaluated from the topography (Figure 4.5a) and the corresponding phase shift  $\Delta\phi_v$  is evaluated from the magnetic image (Figure 4.5b). These two parameters allow us to evaluate the "equivalent" diameter of the MNPs internalized in the vesicles. Being the density of MNPs higher than that of the water, internalized MNPs are bound to be placed in the bottom of the host niosome, as sketched in Figure 4.6a.

Therefore, the relation  $\Delta h + h_v = \Delta z + d_{NP}$  is valid. Thus, for each pair of values of the parameters ( $h_v, \Delta\phi_v$ ),

$\Delta h + h_v$  is fixed. For example, concerning vesicle A1  $h_v = 142$  nm and  $\Delta\phi_v = 2.24$  deg are measured. Being the magnetic image obtained with  $\Delta h = 50$  nm,  $\Delta h + h_v = 192$  nm for vesicle A1. By multiplying the calibration curve reported in Figure 4.2c for different values of  $d_{NP}$ , a family of curves are obtained such as those reported in Figure 4.6b. In particular, curves are considered that intersect the value  $\Delta\phi_{NP} = \Delta\phi_v$  in (at least) one, like those reported in Figure 4.6c. For each curve obtained for a certain value of  $d_{NP}$ , the values of  $\Delta z$  corresponding to  $\Delta\phi_{NP} = \Delta\phi_v$  are evaluated. Note that, as the calibration curve reported in Figure 4.2c is not monotonic, two values of  $\Delta z$  are obtained, one on the increasing portion of the curve (indicated with an open circle in Figure 4.6c) and one on the decreasing one (indicated with an open square in Figure 4.6c). If monotonic calibration curves were observed, only one value of  $\Delta z$  would be obtained, which would simplify the data analysis. Then, each value of  $\Delta z$  is added to the corresponding value of  $d_{NP}$ . The values of  $\Delta z + d_{NP}$  obtained from Figure 5c in correspondence of  $\Delta\phi_v = 2.24$  deg are plotted as a function of  $d_{NP}$  in Figure 4.6d, which has two branches as a result of the not monotonic calibration curve. Finally, the value of  $\Delta h + h_v = \Delta z + d_{NP}$  is used to deduce the diameter of the MNPs into the vesicle  $d_{NP}$  (actually, it should be considered as an effective diameter  $d_{NP}^{eff}$ ) as illustrated in Figure 4.6d. From  $\Delta h + h_v = 192$  nm the value  $d_{NP}^{eff} = 69$  nm is obtained for vesicle A1. Similar calculation has been performed for all the vesicles in Figure 4.5, obtaining the values of  $d_{NP}^{eff}$  reported in Table 4.1. The results for vesicles A and B indicate that each niosome incorporates from one to a few MNPs. Conversely, the higher value of  $d_{NP}^{eff}$  for vesicle C may indicate either that several MNPs were incorporated in the niosome at its formation or that vesicle C is the result of the coalescence of two-three different niosomes with an amount of internalized MNPs similar to that of vesicles A and B. Overall, considering that empty niosomes were observed in the same sample, our results reveal a not uniform incorporation of MNPs into the vesicles, in agreement with TEM observation above.

As far as the performances of the technique are concerned, Figure 4.6c shows that even small variation in the MNPs diameter produces a relatively high variation in phase shift, which makes the technique virtually extremely sensitive. Nevertheless, the actual sensitivity of the technique is limited by the error in the determination of the phase shift on the MNPs and on the vesicles and by the uncertainty in the fitting

parameters of the calibration curves. In addition, it should be noted that in our calculation the effect of the (small) positive phase shift produced by the empty niosomes was neglected. Nevertheless, a more accurate calculation would require to add this value to the phase shift of niosomes incorporating MNPs. Thus, data reported in Table 4.1 should be considered as an approximation by defect of the effective MNPs diameter. The uncertainty in the height of vesicles and MNPs taken from the topographical images of AFM as well as in the MFM phase contrast can be neglected. The main contribution to the uncertainty in the determination of the NPs diameter arises from that of the calibration curve reported in Figure 4.2c. The corresponding uncertainty is reported in table 4.1.

## **4.6 Conclusion**

In conclusion, the use of a novel technique based on the combination of AFM and MFM imaging that allowed us to quantitatively evaluate the amount of MNPs incorporated in single niosomes. Our approach does not require any complex preparation of the sample to be investigated. Although the number of reported measurements does not allow us to perform any statistical evaluation, we observed a not uniform incorporation of MNPs into niosome that resulted in the simultaneous presence of vesicles either empty or incorporating a significant amount of MNPs. Overall, this is the first work where a quantification of MNPs into single vesicular systems is performed using an AFM/MFM based technique. Such promising technique will be improved in the future to obtain more accurate measurements and extended to the direct observation in liquid.

## Chapter 5

# Magnetic Force Microscopy for Materials of Biological Interest

In this chapter, magnetic force microscopy is used to investigate the materials for biological interest. The synthesis and the structural and morphological characterizations have been carried out by AFM/MFM on magnetoferritin,  $\text{Fe}_3\text{O}_4$  nanoparticles functionalized with APTES, leukocytes labeled with Fe@Au nanoparticles and CCRF-CEM cellular system labeled with  $\text{Fe}_3\text{O}_4$ @Cu@Au nanoparticles to study the feasibility and potentiality of AFM/MFM in detecting magnetically labeled biological systems. Detailed discussion by comparing the topography and corresponding phase contrast images qualitatively and quantitatively is reported. The results have been included in a manuscript presently in preparation.

The study is organized as follows. At first, we give research background and details of the sample preparation, as well as of the techniques employed for the characterization of the samples. Then, morphological properties and the corresponding magnetic response of the studied biological samples are described qualitatively and quantitatively using AFM/MFM measurements. The results and analysis of the magnetic characterization are reported to reveal the potentiality of AFM/MFM to investigate biological systems. The conclusions are drawn at the end.

### 5.1 Introduction

In the past decades, nanoparticles with biomedical application attracted more and more attention in cancer treatments including surgery, radiation, chemotherapy and other therapies, but there are still facing some problems like the ineffective accessibility to the tumors and the lack of selectivity toward tumor cells. Nanoparticles are used for drug delivery system due to their ability to target specific locations in the body, the corresponding reduction of the quantity of drug in the target and reduction of the concentration of the drug at

nontarget sites to minimize severe side effects. Many studies about nanoparticles and cellular system have been reported since nanoparticles not only can be viewed as simple carriers for biomedical applications, but also can play an active role in mediating biological effects.

#### **a) Magnetic nanoparticles for biomedical research**

Magnetic nanoparticles present a higher performance in terms of chemical stability, biocompatibility and large susceptibility [216] for biological applications like magnetohyperthermia treatments, magnetically assisted drug delivery, cell isolation, molecular recognition, biological macromolecules purification, biosensors, and magnetic resonance imaging (MRI) or positron emission tomography (PET) enhancement [217-218]. Not only the nanosize of magnetic nanoparticles is comparable to many biological molecules like protein and gene [217], but also they are capable to be directed and concentrated within the target tissue by means of external magnetic field and to be removed once therapy is completed. Its superparamagnetic phenomenon means no need to keep magnetized after action of magnetic field, thus the risk of particle aggregation will be reduced [219].

Functionalized magnetic nanoparticles have valuable applications due to their ability to bind drugs and/or biological macromolecules [220]. APTES-functionalized surfaces have been shown to be nontoxic to embryonic rat cardiomyocytes *in vitro* [221]. The ligand 3-aminopropyltriethoxysilane (APTES) is a kind of surface modification agent, which is an aminosilane frequently used in the process of silanization, the functionalization of surfaces with alkoxy silane molecules. Molecules bound to the surface of APTES have more functions, since amino groups exterior allow easy coupling with antibodies, proteins and molecules and fluorescent dyes. Gold has been the attractive coating material because of its well-known optical properties and chemical functionability [222]. As well pure Fe core nanoparticles are expected to be superior due to the high saturation magnetization. However, unprotected Fe nanoparticles, being highly reactive in air/aqueous environment, need a protective layer. Thus, Fe@Au magnetic core-shell nanoparticles were prepared studied with a variety of methods such as SEM, TEM, XRD, FTIR, EDX, TGA et al. for physical properties

[223-227], and SQUID for the magnetic property [228]. Gold-coated Fe<sub>3</sub>O<sub>4</sub> magnetic core-shell nanoparticles have been studied also [229-232].

Iron nanoparticles show a reduced cytotoxicity under certain concentration and biocompatibility with appropriate surface coating even at very high concentration [233]. And a single ferritin molecule can sequester up to 4500 iron atoms, thus making it potentially a very effective iron delivery system. Ferritins are a family of proteins found in all domains of life as a ubiquitous and highly conserved iron-binding protein. It consists of a central core of hydrated iron (III) oxide encapsulated with a multisubunit protein shell. Several kinds of nanoparticles have been synthesized in a cage-shaped protein-apoferritin, and delivered to the desired position on a substrate by modifying the outer surface of apoferritin [234]. Over the last years a number of studies demonstrated the ability to use the iron-binding protein ferritin as a novel endogenous reporter gene that allows the detection of gene expression by magnetic resonance imaging (MRI) [235], which would directly change the MR signal, in its expression site, in analogy to fluorescent proteins in optical imaging, without the need to administer additional contrast materials. Initial experiments designed to observe resonant quantum tunneling of the magnetization of horse-spleen ferritin particles were performed at temperatures of approximately 30 mK by measuring the frequency-dependent magnetic noise and magnetic susceptibility of the particles using an integrated dc superconducting quantum interference device (SQUID) microsusceptometer [236].

#### **b) Characterization methods applied to nanoparticles**

The investigation of the interaction between functionalized nanoparticles and biological molecules still presents enormous challenges. Transmission electron microscopy and confocal laser scanning microscopy were used together to elucidate the precise mechanism by which the lung cancer cells uptake the magnetic nanoparticles [237]. Indeed, it is not straightforward to confirm the location of the nanoparticles within the cells using single characterization method.

Fluorescence microscopy has revealed that iron oxide nanoparticles (IONPs)-exposed astrocytes contain

accumulated IONPs in intracellular vesicles, and also extracellularly attached to the cell membrane [238]. However, the nanoparticles need to be initially fluorescence labeled, and the maximum resolution is limited by half of the light wavelength [239]. Two photon microscopy (TPM) has also been used to study magnetic nanoparticles and cell interaction because of its improved resolution and low damage outside the focal volume [240], but the nanoparticles still need to be labeled with two photon dye. Transmission electron microscope (TEM) is one of these label-free detection methods, which can study the cellular uptake of nanoparticles at a nanoscale resolution [241], but the sample preparation is not straightforward and the analysis have to be performed in vacuum. Other label-free imaging methods such as magneto-motive ultrasound and optical coherence tomography (OCT) are generally used in tissue and animal experiments but their use is limited by their relatively low resolution [242-243]. Although resolution of biological samples can be achieved by using the scanning electron microscopy (SEM), these samples have to be frozen, fixed, dried unless environmental SEM.

The invention of the atomic force microscopy (AFM) has opened up a novel approach for studying nanomaterials. It acts as a powerful tool for cell biology research giving ultrahigh resolution even in real time under near physiological conditions. Besides cells, molecular recognition studies with AFM provide insight into the localization of receptor binding sites. However, the AFM tip usually cannot target the nanoparticles under cell membranes, which is very important for drug delivery, especially in the aspect of tumor diagnosis and treatment, to understand the interaction between biological molecules and functionalized nanoparticles. Effect of cellular uptake of uncoated and Pn-coated SPION on cells of human fibroblasts was investigated [244], but AFM only was limited to show the structure of Pn-SPION other than the behavior of cellular system.



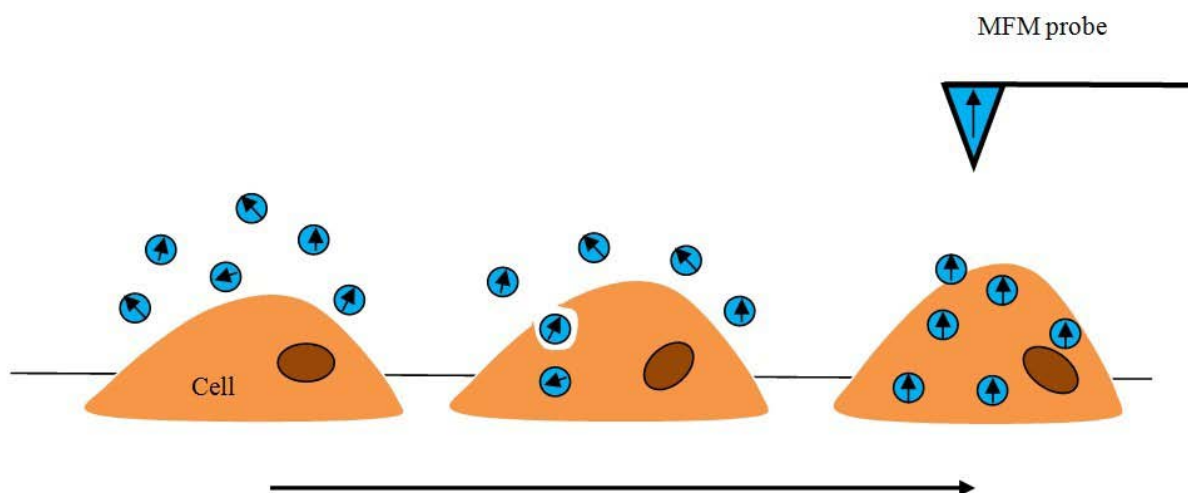


Figure 5.1 Cell incubation with magnetic nanoparticles

### c) Investigation of biological samples by magnetic force microscopy

MFM not only provides the typical nanometer resolution of AFM, but also can detect intercellular environment without extra complicated labeling. Since AFM imaging relies on measurement of the short-range interaction force between tip and the sample surface, correspondingly MFM imaging depends on non-contact long-range interactions.

Cell incubation with magnetic nanoparticles and scanning by MFM probe are shown in Figure 5.1. Interactions between streptavidin molecules attached to a self-assembled monolayer or to a modified glass surface and biotin-coated magnetic nanoparticles were demonstrated using MFM [245-246]. Structural organization and distribution of endothelin receptors with magnetic beads on the surface of smooth muscle cells were investigated with magnetic force microscopy [247] too. MFM was employed to observe antisense oligonucleotides (ASOs)-coupled silica-coated magnetic iron oxide nanoparticles internalized into human leukemia (HL-60) cells [248]. MFM was also applied for the characterization of magnetic iron oxide nanoparticles and their cellular uptake behavior with the MCF7 carcinoma breast epithelial cells [249].

Although MFM is a promising technique for the investigation of magnetic properties of biological samples interacting with MNPs, it has been employed in a relatively small number of works. Moreover, while qualitative magnetic imaging is easy to be obtained, the capability of extracting quantitative information

from MFM images has been only marginally exploited. Here, we demonstrate the potential of MFM for the study of magnetic properties of different nano-biosystems (magnetoferritin, functionalized MNPs, magnetically labeled cells), illustrating our approaches which aim at deducing quantitative information from MFM characterizations. Although such studies should be considered somehow preliminary, we will highlight the potentiality and the limits of MFM.

## **5.2 Investigated Nanomaterials**

In this chapter, there are four typical biomaterials detected with MFM: ferritin molecules loaded with iron atoms; magnetite ( $\text{Fe}_3\text{O}_4$ ) coated with APTES (used for functionalizing biomedical application); leukocytes embedded with Fe@Au nanoparticles; CCRF-CEM cells labeled with  $\text{Fe}_3\text{O}_4$ @Cu@Au nanoparticles.

### **A) Preparation of Magnetoferritin Nanoparticles**

Ferritin and apoferritin production was carried out in our laboratories accordingly to previously reported procedures [250]. In particular, ferritin from *P. furiosus* was overproduced in *E. Coli*, and purified by a heat step. Apoferritin was prepared by reduction with sodium dithionite, chelation with 2,2-bipyridine, and dialysis against MES/NaOH buffer 50 mM, pH 8.5. The prepared solution was deaerated by bubbling nitrogen for 60 min at 60°C. Furthermore, a  $\text{FeSO}_4 \cdot 7\text{H}_2\text{O}$  solution (50 mM) in HCl/water pH=2 was prepared anaerobically.

Small aliquots were slowly added to the apoferritin in order to load up to 1000 Fe atoms in each ferritin. The reaction was maintained under stirring at 60°C for 30 min. The solution was purified via size exclusion chromatography by (PD-10 column, GE Healthcare) in order to exclude the ions not included inside the protein.

### **B) Preparation of $\text{Fe}_3\text{O}_4$ -APTES Nanoparticles**

#### **Preparation of $\text{Fe}_3\text{O}_4$ Nanoparticles**

The synthesis phase of the magnetic cores is obtained through the optimization of the well known process of co-precipitation of ferrous and ferric salts, which has been proposed by Massart. The precipitation of the nanoparticles is obtained by adding to a alkaline solution containing NaOH or NH<sub>4</sub>OH, an aqueous solution containing of Fe<sup>3+</sup> and Fe<sup>2+</sup>. The stoichiometric ratio of 2:1 allows the formation of magnetite (Fe<sub>3</sub>O<sub>4</sub>) in accordance with the reaction  $Fe^{2+} + 2Fe^{3+} + 8OH^- = Fe_3O_4 + 4H_2O$ . The parameters of the process, such as the pH value, ionic strength, temperature, the salts, the concentration ratio Fe(II)/Fe(III), have been extensively studied, demonstrating the influence on the performance of co-precipitation, the diameter, the size distribution and shape of the nanoparticles [251].

### **Coating Fe<sub>3</sub>O<sub>4</sub> with APTES**

The second phase consists in the coating of the magnetite cores. The coating, as previously mentioned, has two functions: the stabilization of the particles of iron oxide, which is of crucial importance in order to obtain a stable ferrofluid in a biological environment, and the functional surface with suitable organic compounds able to bind to specific biological entities. Being Lewis acids, the iron atoms present on the surface bind with the OH groups of dissociated water. These hydroxyl groups can react with acids and bases, making the surface of the magnetite positive or negative as pH changes. The isoelectric point was observed at pH 6.8 [278]. Around this point of zero charge (PZC) the surface charge density is too small and the particles are not stable in water for a long time. So the particles were coated with an organic ligand, 3-aminopropyltriethoxysilane (APTES). It has a hydrolytically stable bond between the silicon and the group [-CH<sub>2</sub>-CH<sub>2</sub>-CH<sub>2</sub>-NH<sub>2</sub>], and three groups [CH<sub>3</sub>-CH<sub>2</sub>-O-] linked to the silicon with a high tendency to hydrolyze and to bind with the particles of Fe<sub>3</sub>O<sub>4</sub>. Such a coating stabilizes the nanoparticles by fencing magnetic dipoles of the nuclei, and at the same time, introducing the columbic repulsive actions agglomeration resistance.

A solution of Fe<sup>2+</sup>/Fe<sup>3+</sup> (0.79976 mg of FeSO<sub>4</sub> amidic and 0.62745 mg of Mohr salt ((NH<sub>4</sub>)<sub>2</sub>Fe(SO<sub>4</sub>)<sub>2</sub>) in 100 ml of water) was dropped into a solution of ammonia of 300 ml (0.7 M) placed in an ice bath and subjected to mechanical agitation. The precipitation of iron hydroxides on the ions formed the crystallites of magnetite, after 15 minutes. The dispersion obtained (dark brown in color) was then centrifuged at 4000 rpm, for 15

minutes by rotor with radius of 7 cm . The solid sample was dissolved in distilled water and dialyzed for one night at room temperature, using a membrane (cutoff: 30 kDa) to remove the excess salt.

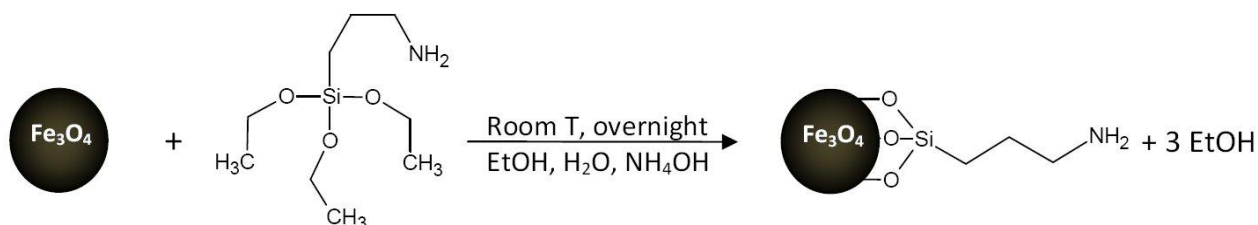


Figure 5.2 Schematic representation of the reaction during APTES coating of magnetite nanoparticles

The hydro-alcoholic alkaline solution contained 140 mg of  $\text{Fe}_3\text{O}_4$  nanoparticles, ethanol and  $\text{H}_2\text{O}$  in molar ratios, as shown below in Table 5.1. 2.34 ml of APTES were subsequently added to this solution under mechanical stirring. Then the hydrolysis reaction proceeded for one night at room temperature.

Table 5.1 Experimental parameters for the reaction of APTES coating

Reactants	$\text{H}_2\text{O}$	$\text{NH}_4\text{OH}$	$\text{CH}_3\text{CH}_2\text{OH}$	APTES
Molar ratio	54.0	0.1	41.0	1.0
Volume Ratio	963.8	1.91	2390.98	234
Volume Used	9.63 mL	19.1 mL	23.91 mL	2.34 mL

The material was then washed with ethanol and water, and magnetically "decanted" using magnets of neodymium, iron and boron ( $\text{Nd}_2\text{Fe}_{14}\text{B}$ ; magnetic field of about 300 mT). The solution obtained was very well dispersed in a stable fluid system due to the presence of magnetic material. The sample was dropped on a silicon substrate for the scanning under MFM.

### C) Preparation of Fe@Au Nanoparticles Incubated with Leukocytes

#### Preparation of Fe@Au Nanoparticles

$\text{Fe}(0)$  nanoparticles were synthesized by thermal decomposition of the complex  $\text{Fe}(\text{II})$ -stearate. To obtain this complex, two solutions were prepared in deoxygenated distilled water,  $\text{FeSO}_4 \cdot 7\text{H}_2\text{O}$  (10 mM) and

sodium stearate (25 mM). 1 g of stearate was dissolved in 30 mL of octyl ether during synthesis. The solution is kept under Argon atmosphere, reflux for two hours and carried between 285°C - 300°C. After the formation of Magnetic NPs of Fe(0), the precipitate was washed repeatedly (first in octane, then in ethanol (both degassed). The Au shell on the magnetic core was prepared by a redox reaction between Fe(0) and Au(III). The coating was made by dissolving 120 mg of Fe NPs in a solution of K<sub>2</sub>CO<sub>3</sub> in ethanol, sonicated for 20 minutes. Then, 190 mg of HAuCl<sub>4</sub> were dissolved in 5 mL methanol and were dripped in the MNPs solution. The reaction was carried out in an inert environment to prevent iron oxidation, using degassed solvent and under argon atmosphere. The mixture was allowed to react for an hour. To increase the thickness of the Au shell, 94 mg of HAuCl<sub>4</sub> in 5 ml of methanol and 85 mg of ascorbic acid in 50 ml of the same solvent were added to the solution ( Ascorbic Acid : Au = 2:1). The Fe@Au nanoparticles were separated by magnetic decantation and washed several times with methanol.

### **Functionalization of Nanoparticles**

The nanoparticles were functionalized with an active ester (NHS-ester) of lipoic acid, and then with the PLL-PEG (a copolymer of 9900 Da).

### **Internalization of MNPs in Human Leukocytes**

*In vitro* experiment involved the use of a family of mixed leukocyte, which were first washed with Phosphate buffered saline (PBS) buffer and separated from erythrocytes by centrifugation. The leukocytes and in particular granulocytes can internalize NPs sizes of < 40-50 nm. During phagocytosis, the colony of mixed leukocytes was incubated with MNPs at 37°C for about eight hours. After the incubation, the engulfed cells were fixed and dehydrated. 2 µL of the cells were suspended on silicon slides for AFM and MFM analysis.

### **D) Preparation of Fe<sub>3</sub>O<sub>4</sub>@Cu@Au Nanoparticles Incubated with CCRF-CEM Cells**

#### **Preparation of Fe<sub>3</sub>O<sub>4</sub> nanoparticles**

Under mechanical stirring and Argon atmosphere, 300 mL of NH<sub>4</sub>OH (0.7 M), 68.451 mg of Mohr salt

$(\text{NH}_4)_2\text{Fe}(\text{SO}_4)_2 \cdot 6\text{H}_2\text{O}$ , 81.735 mg ferric sulphate ( $\text{Fe}_2(\text{SO}_4)_3$ ), and 47.414 mg of PVP dissolved in 100 mL of distilled water, were introduced in a two-necked flask. The solution was left for 30 minutes at room temperature, then heated to 80°C for 30 minutes. After cooling the product was separated by magnetic decantation. The precipitate was washed first with a solution of 2M NaCl, and then several times with double distilled  $\text{H}_2\text{O}$ . The product was dried under vacuum.

### **Cu shell**

The coating of magnetite with copper was performed by reduction of a salt of Cu(II) with ascorbic acid. 173.42 mg of magnetite were dispersed in 100 mL of distilled  $\text{H}_2\text{O}$  and this solution was transferred into a thermostated flask at 47°C, under mechanical stirring. Subsequently, 175.50 mg of ascorbic acid and 120.27 mg of  $(\text{Cu}(\text{NO}_3)_2)$  dissolved in 10 mL of distilled water, then the NPs solution ( $\text{Fe}_3\text{O}_4@\text{Cu}= 1.5:1$ ) were added. After 60 minutes and after cooling, several washings with distilled water were performed by magnetic decantation and the precipitate was separated. The procedure of coating was repeated a second time starting from nanoparticles of  $\text{Fe}_3\text{O}_4@\text{Cu}$  already in solution, but using a smaller amount of cupric nitrate (in a molar ratio 1:4 with the magnetite). The nanoparticles of  $\text{Fe}_3\text{O}_4@\text{Cu}$  were preserved in a solution of ascorbic acid (~30 mg in 100 mL distilled water) in a molar ratio 2:1 with copper.

### **Au shell**

After washing the nanoparticles coated with copper and having separated the precipitate, the coating with gold was proceeded. The precipitate was dispersed in 25 mL of distilled water and sonicated for 15 minutes. Then 118.20 mg of tetrachloroauric acid ( $\text{HAuCl}_4$ ) were dissolved in 5 mL distilled water. In a thermostated flask (60°C) 25 mL of a saturated solution of sodium bicarbonate ( $\text{NaHCO}_3$ ) were set up, then the solution of nanoparticles and the solution of the acid tetrachloroauric. After 45 min the solution was dealt with cooling treatment, several washings with double-distilled water by magnetic decantation were performed and the precipitate was separated. The procedure of coating was repeated a second time starting from nanoparticles of  $\text{Fe}_3\text{O}_4@\text{Cu}@Au$  already in solution, but using a smaller amount of tetrachloroauric acid (50% of the amount used at the first step). For the second coating, it required the presence of a reducing agent such as

ascorbic acid, in a molar ratio 5:1 with the gold. After 90 minutes, the solution is cooled and several washings with ethanol by magnetic decantation were executed. The nanoparticles of  $\text{Fe}_3\text{O}_4@\text{Cu}@\text{Au}$  were dried under vacuum. The functionalization is the same as  $\text{Fe}@\text{Au}$  nanoparticles. But in this case we have functionalized the nanoparticles with an ester of the folic acid.

### **Experiment with Human Sero Albumin (HSA)**

To link the protein to MNPs, 2 mg of HSA were dissolved in 2 mL of PBS buffer at pH 8.2, and added to a solution of 40 mL of PBS dispersing 20 mg of MNPs drop by drop. The reaction was kept for 2.5 hours under mechanical stirring and ice bath. Then the product was magnetically decanted and washed several times with PBS buffer and distilled  $\text{H}_2\text{O}$ . The functionalized MNPs were dialyzed against double distilled  $\text{H}_2\text{O}$  for 12 h using a dialysis membrane with a semi-permeable "Cutoff" of 14 KDa.

### **Incubation of MNPs with CCRF-CEM cells**

To obtain an homogeneous sample of cells, we made a gradient centrifugation and then we suspended the cells in 4 mL of saline solution. A flask containing 7.5 mL of a culture medium were added 2 mL of cell suspension and 0.5 mL of a solution approximately 1 mg/mL of nanoparticles functionalized with folate. It was incubated at  $37^\circ\text{C}$ , 95% humidity and 5%  $\text{CO}_2$ . After 18 hours (a cell cycle) the sample was observed and fixated for MFM. CCRF-CEM cells were fixed for MFM operation. The fixation process maintains, as far as possible, the structural characteristics of the sample for microscopy.

The fixation process requires two solutions: a solution of 1.5% glutaraldehyde in PBS and a solution of 2% osmium tetroxide ( $\text{OsO}_4$ ) in PBS. Cells are dispersed in the first solution for 2-3 hours at  $4^\circ\text{C}$  and then washed 3 times for 5-10 minutes each time. Then the cells were introduced to the second solution, staying for 1-2 hours at room temperature. At the end the cells were washed and kept in solution for the preparation of AFM-MFM samples.

## **5.3 Equipment**

Experiments were performed using AFM apparatus (Solver, NT-MDT, Russia), the accuracy of the calibration of piezoelectric actuator in the z direction having been previously checked using calibration gratings (TGS1, NT-MDT, Russia). The AFM apparatus was equipped with two kind of magnetic tips, standard Si cantilevers with a 40 nm thick CoCr magnetic coating (MESP-RC, Bruker Inc.), with nominal  $k_c$  equal to 5 N/m and first resonance frequency in the range  $\pm 500$  kHz was adopted for  $\text{Fe}_3\text{O}_4$ -APTES nanoparticles and leukocytes cellular system with Fe@Au nanoparticles. After the damaging of this kind of tip another one from the same producer was applied to detect  $\text{Fe}_3\text{O}_4$ @Cu@Au nanoparticles with CCRF-CEM cells, with nominal  $K_C$  about 1 - 5 N/m and first resonance frequency in the range 60 - 100 kHz, as reported by the producer (MESP, Bruker Inc.). The magnetic domains of the tip were vertically oriented by a magnet. In the first pass, topographic images were obtained in standard tapping mode. In the second pass, MFM phase images were obtained for different values of z with the tip oscillating at its first resonance frequency. Experiments were performed in open environment and ambient atmospheric conditions. The scan rate was 0.1–1Hz, depending on the scanned area, with a resolution of 256 pixels per line. MFM experiments were recorded by interleaving the topographic scan with lift mode, for MFM data analysis, the phase contrast was measured for magnetic nanoparticles using the section analysis feature of nanoscope software----NOVA.

## 5.4 Magnetic Force Microscopy Characterizations

### 5.4.1 Study of Magnetoferritin

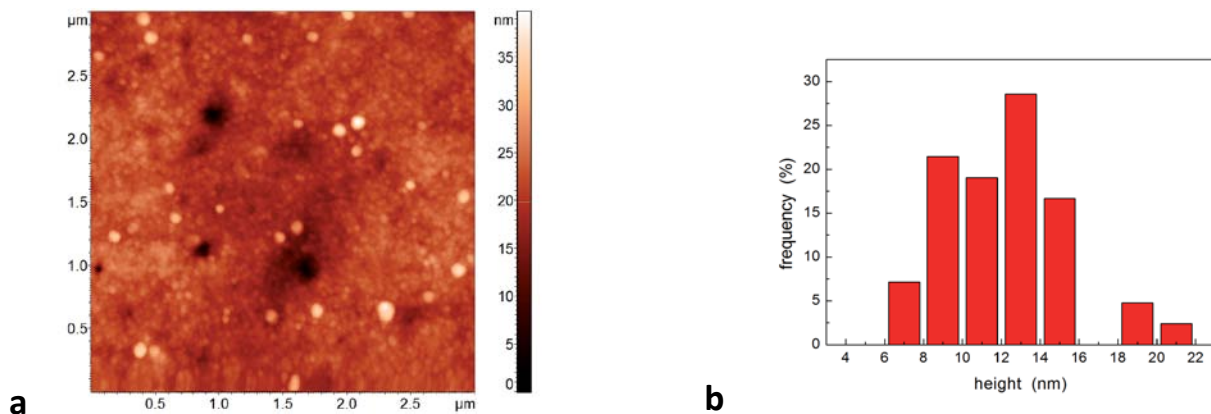


Figure 5.3 AFM detection with magnetoferritin molecules: (a) topographical reconstruction of magnetoferritin



molecules ( $3 \times 3 \mu\text{m}^2$ ); (b) size histogram of magnetoferritin molecules (data extracted from the topographical image).

The topography of an area with size  $3 \times 3 \mu\text{m}^2$  is reported in Figure 5.3a where magnetoferritin molecules (the circular features which appear brighter, i.e., which are higher, than the substrate) are clearly visible. To analyze their dimension, the height of different molecules (corresponding to the molecule diameter) observed on randomly selected areas have been measured, the obtained statistics being reported in Figure 5.3b from which the diameter of magnetoferritin molecules can be evaluated as  $11 \pm 3 \text{ nm}$ . It should be noted that the presence of residuals of  $0.1 \text{ M } (\text{NH}_4)_2\text{Fe}(\text{SO}_4)_2 \cdot \text{H}_2\text{O}$  solution on the substrate prevents one from more accurately evaluating the molecules height. As a result, the bare analysis of the molecules height obtained with standard AFM topographical reconstruction does not allow us to definitely distinguish between magnetoferritin and apoferritin, the diameters of which have been reported as high as  $10 \text{ nm}$  and  $12 \text{ nm}$ , respectively [252].

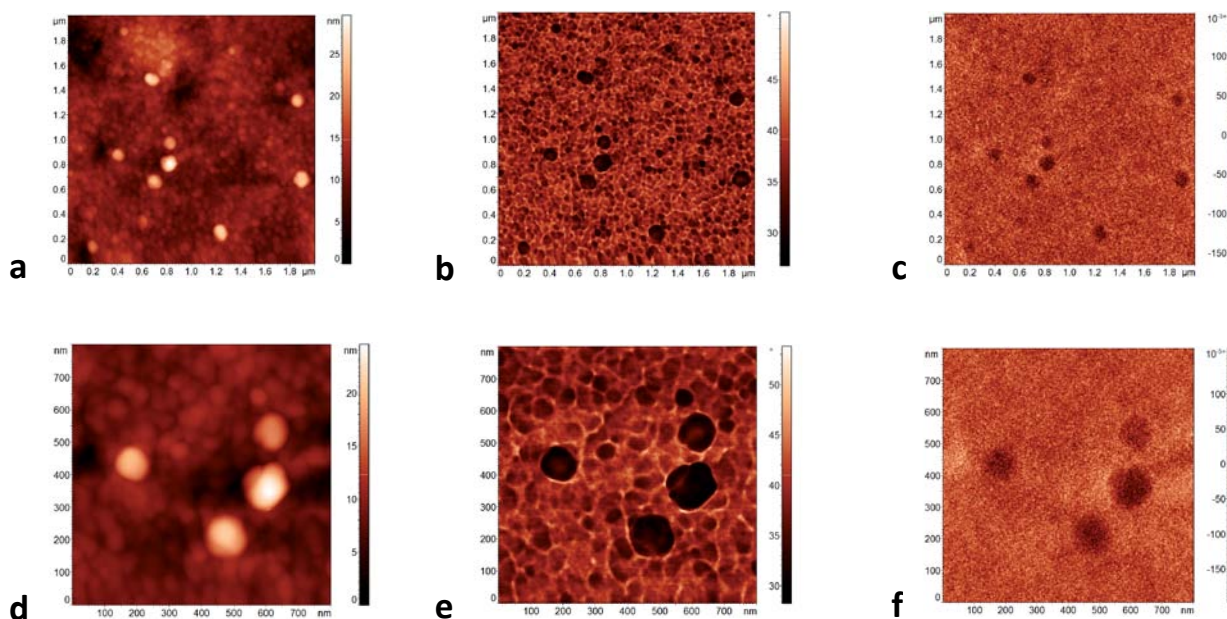
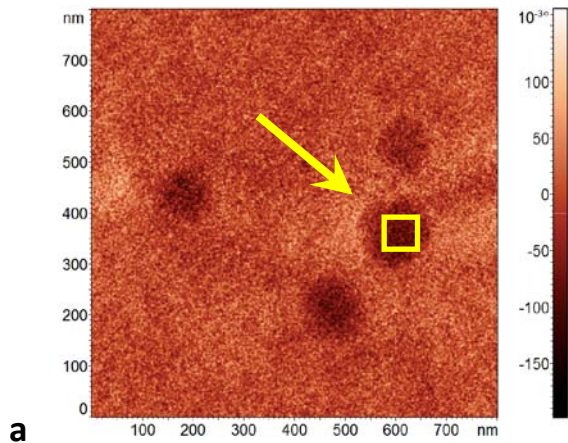


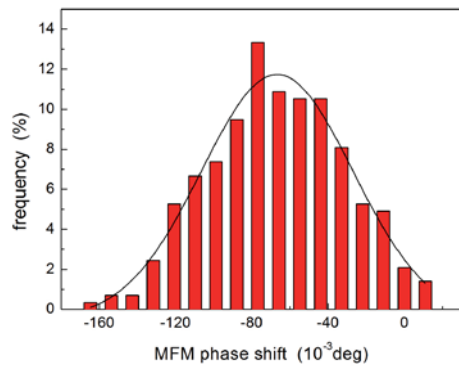
Figure 5.4 AFM topography image (a), standard phase image (b), and MFM phase image (c) of a selected area with certain magnetoferritin molecules ( $2 \times 2 \mu\text{m}^2$ ); corresponding further zoom-in area measured with AFM/MFM, reported as AFM topography image (d), standard phase image (e), and MFM phase image (f).

An example of AFM/MFM characterization of magnetoferritin molecules on a selected area is reported in Figure 5.4, which has been performed by acquiring the topography (Figure 5.4a) and the standard phase

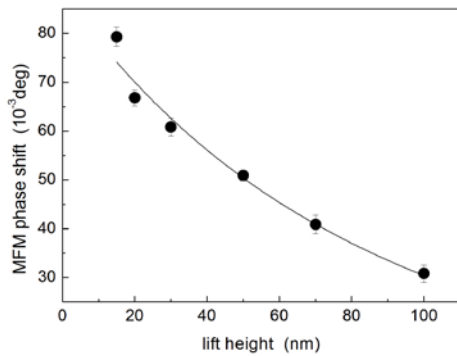
image (Figure 5.4b) during the first pass in tapping mode and the MFM phase image in the second pass (Figure 5.4c). A detail of the area ( $800 \times 800 \text{ nm}^2$ ), where four magnetoferritin molecules are visible, is reported in 5.4d (topography), 5.4e (standard phase image), and 5.4f (MFM phase image). The characterization of the same area has been repeated several times with different values of lift height  $\Delta z$  in the range 15-100 nm. In particular, Figure 5.4a show the topography of an area with size  $2 \times 2 \text{ }\mu\text{m}^2$  where magnetoferritin molecules are visible, the lateral dimensions of which appear wider than they really are due to the convolution effect with the tip shape. Indeed, from Figure 3a the curvature radius of the coated tip (namely,  $R_{ct}$  where  $R_{ct} = R_t + c$  being  $R_t$  the radius of the uncoated AFM tip and  $c$  the thickness of the magnetic coating) can be estimated in the range 110 - 280nm, significantly higher than that reported by the producer for a new tip. In order to confirm such values, scanning electron microscopy (SEM) coupled with energy dispersive X-ray (EDX) spectroscopy and mapping has been used to image the tips we used, revealing values of  $R_{ct}$  as high as a few hundreds of nanometers. Simultaneously to the topographical reconstruction, the standard phase image is acquired which is reported in Figure 5.4b. Despite showing a relevant contrast in correspondence of the magnetoferritin molecules (about 10 deg), standard phase images do not allow one to definitely distinguish between the molecules and the substrate. Indeed, in tapping mode where cantilever oscillation amplitude is maintained constant by the AFM feedback loop, such a contrast reflects variations in the energy dissipation during a cycle of tapping [253-254]. Therefore, the contrast in Figure 5.4b may suggest the presence on the substrate around the molecules of residuals of apoferritin. Conversely, a clear contrast in correspondence of the magnetoferritin molecules is observed in the MFM phase image obtained with  $\Delta z = 15 \text{ nm}$ , which is reported in Figure 5.4c, which unambiguously demonstrates the presence of magnetic material in the core of the molecules. Therefore, MFM phase images confirm that synthetic process resulted in the production of magnetoferritin from apoferritin.



**a**



**b**



**c**

Figure 5.5 MFM images of magnetoferritin molecules for  $\Delta z=15\text{nm}$  (a); histogram of MFM phase shift with Gaussian fit (b); experimental values of the magnetic phase shift for different values of the tip-molecule distance together with the corresponding theoretical fit using Eq. (5.2).

In order to quantitatively analyze MFM measurements, for each magnetoferritin molecule the maximum value of the MFM phase shift was evaluated by selecting a small area in correspondence of the top of the molecule (as illustrated in Figure 5.5a, where the square corresponding to the selected area is actually

enlarged for the sake of clearness) and determining the mean value and the standard deviation of the MFM phase shift from the Gaussian fit of the obtained histogram, as exemplified in Figure 5.5b. Such a procedure has been repeated for each magnetoferritin molecule and for each value of lift height. For each magnetoferritin molecule, the MFM phase shift has been plotted as a function of  $\Delta z$ , as illustrated in Figure 5.5c. In accordance with a relatively well established approach [255-256], MFM phase shift data can be analyzed through the equation

$$\Delta\varphi = \frac{\mu_0}{4\pi} \frac{12\pi Q_c}{k_c} m_s m_{ct} \frac{180}{\pi} \frac{1}{(\Delta z + h_{ts})^5} \quad (5.1)$$

where:  $\mu_0$  is the vacuum magnetic permeability;  $k_c$  and  $Q_c$  are the spring constant and the quality factor of the cantilever, respectively;  $m_s$  and  $m_{ct}$  are the magnetic moments of the nanoparticle and the coated tip, respectively;  $\Delta z + h_{ts}$  is the distance between the magnetic centers of the tip and the sample during the second pass. As an example, if both the sample and the tip can be modeled as spheres,  $h_{ts} = d/2 + s + R_{ct} + \delta$  where  $d$  and  $s$  are the diameter of the magnetic core and the thickness of the nonmagnetic shell of magnetoferritin molecule, respectively, and  $\delta$  is amplitude of the cantilever oscillation in the first pass [255]. As for  $m_{ct}$ , it can be approximated as  $m_{ct} = \frac{4}{3}\pi(R_{ct}^3 - R_t^3)M_c$ , where  $M_c$  is the saturation magnetization of the magnetic coating of the tip [288]. For the sake of simplicity, Eq. (5.4) can be rewritten as

$$\Delta\varphi = \frac{A}{(\Delta z + h_{ts})^5} \quad (5.2)$$

having introduced the parameter  $A$  defined as

$$A = \frac{\mu_0}{4\pi} \frac{12\pi Q_c}{k_c} m_s m_{ct} \frac{180}{\pi} \quad (5.3)$$

For each magnetoferritin molecule, experimental  $\Delta\varphi$  versus  $\Delta z$  data have been analyzed using Eq. (5.2), as exemplified in Figure 5.5 (solid line), thus obtaining the best fitting values of  $h_{ts}$  and  $A$ . As for the former,  $h_{ts} = 210 \pm 15$  nm is obtained, which is coherent with the values of  $R_{ct}$  observed with blind reconstruction and

SEM analysis. As for the latter,  $A = (4 \pm 1) \times 10^{-35} \text{ m}^5 \text{ deg}$  is calculated. For comparison, an approximated theoretical value of  $A$  can be roughly calculated from Eq. (5.3) as follows.  $Q_c/k_c \approx 100$  can be assumed. Being  $m_{ct} \approx 10^{-16} \text{ Am}^2$  reported by the producer for a brand new tip ( $R_{ct} = 35 \text{ nm}$  and  $c = 25 \text{ nm}$  are reasonable values), assuming the same value of  $c$  and the measured values of  $R_{ct}$ , its actual value can be estimated as  $100 \times 10^{-16} \text{ Am}^2$  is case of our tips. If the theoretical value for maghemite is assumed for  $m_s$  [255], the approximated value of  $A \approx 1 \times 10^{-35} \text{ m}^5 \text{ deg}$  is obtained, in good agreement with our experimental data. It is worth mentioning that, if the experimental values of  $m_s$  observed for magnetoferritin are assumed [255],  $A \approx 6 \times 10^{-37} \text{ m}^5 \text{ deg}$  is calculated which is significantly lower than the value we experimentally determined. Really, the main contribution to the uncertainty in MFM quantitative analysis results from that in the magnetic properties of the tip. Therefore, although in recent years MFM has been used to quantitatively study the magnetic properties of ferritin and nanometer sized MNPs [255-258], in order to definitely assess the magnetic properties of magnetoferritin and other molecules at the nanoscale the value of  $m_{ct}$  should be calibrated using a reference sample. Recently, an approach has been proposed in which such a calibration is performed for a fixed value  $\Delta f$  using MNPs with traceably determined magnetization dispersed on a Si surface as a MFM reference sample [260]. Following the approach illustrated in this work, using a suitable MFM reference sample to experimentally determine the parameters  $A$  and  $h_{ts}$  would result in the calibration of  $m_{ct}$  - relatively independently of the used values of lift height - and thus in the capability of MFM of quantitatively measuring the magnetic momentum of single MNPs with nanometrical lateral resolution.

#### 5.4.2 Analysis of Fe<sub>3</sub>O<sub>4</sub>-APTES Nanoparticles

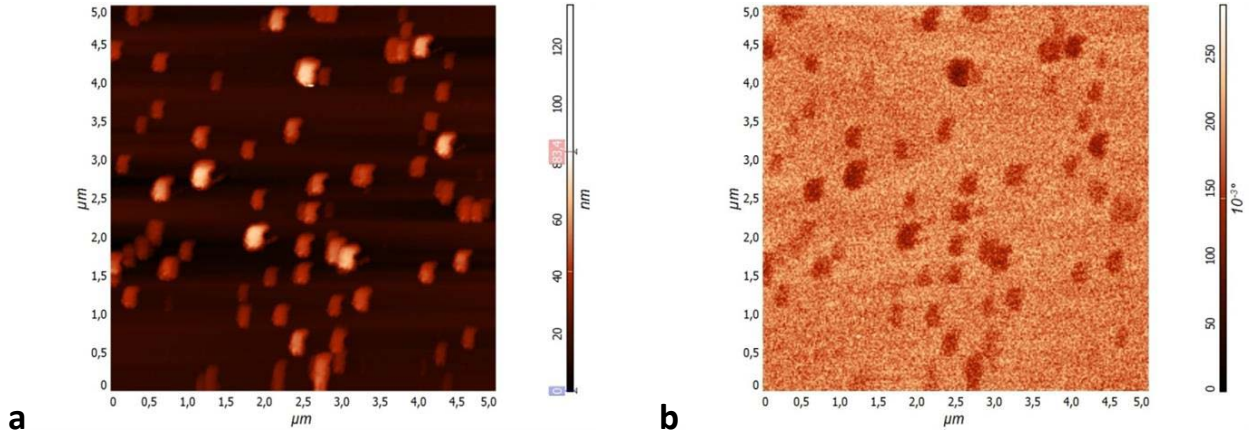


Figure 5.6 Topographical image of  $\text{Fe}_3\text{O}_4$ -APTES nanoparticles on Si substrate (a) and the corresponding phase shift image acquired at  $z = 100.5 \text{ nm}$  (b).

Figure 5.6a shows the topographical reconstruction of an area ( $5 \times 5 \mu\text{m}^2$ ) of such a sample where  $\text{Fe}_3\text{O}_4$ -APTES nanoparticles are clearly visible. Figure 5.6b reports the corresponding phase image acquired at  $\Delta z = 100.5 \text{ nm}$ . From the Figure 5.6, it is evident that the isolated particles produce a magnetic phase contrast (always negative). As discussed in chapter 2, the negative magnetic phase shift is due to attractive interaction between tip and particles. Indeed, the magnetic field produced by the probe in the vicinity of the individual particles induces their magnetization in the same direction of magnetization of the tip, and thus produces an attractive force between tip and sample. Therefore, MFM is demonstrated as a useful technique for the simultaneous imaging of the topography and magnetic properties of superparamagnetic nanoparticles.

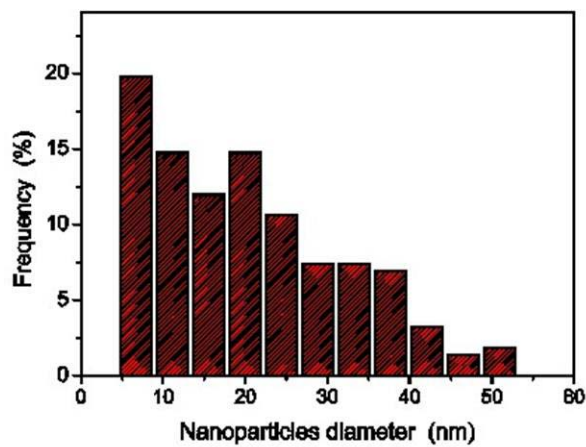
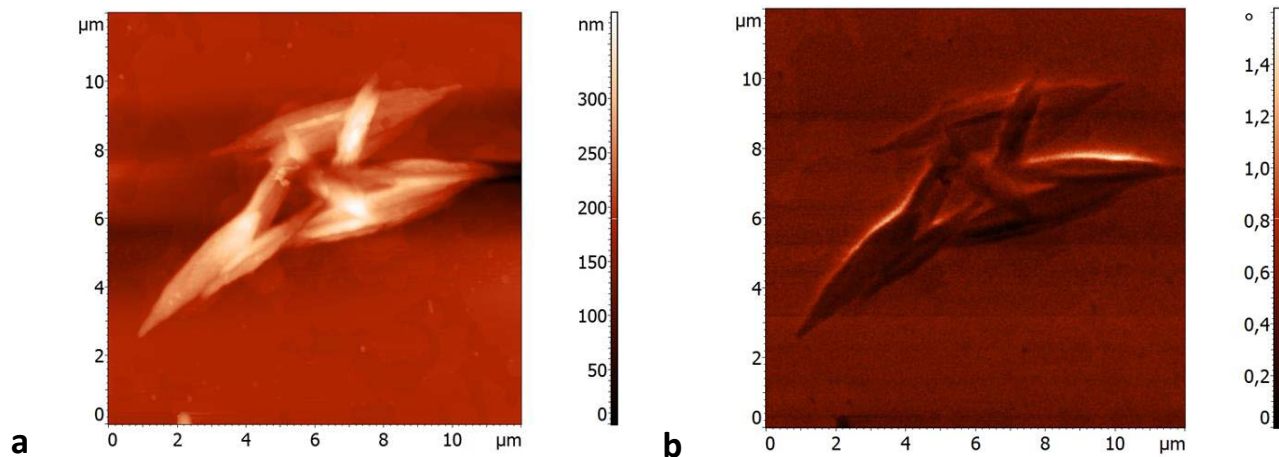


Figure 5.7 Size histogram of  $\text{Fe}_3\text{O}_4$ -APTES nanoparticles

To analyze the dimension of Fe<sub>3</sub>O<sub>4</sub>-APTES nanoparticles, the height of different nanoparticles (corresponding to the nanoparticle diameter) observed on randomly selected areas have been measured, the obtained statistics being reported in Figure 5.7. The diameter of Fe<sub>3</sub>O<sub>4</sub>-APTES nanoparticles can be evaluated as 22 ± 3 nm, smaller than 30 nm. The stray field at the tip is sufficient to induce a detectable magnetic signal of Fe<sub>3</sub>O<sub>4</sub>-APTES without extra magnetic field, which facilitates the analysis of Fe<sub>3</sub>O<sub>4</sub>-APTES nanoparticles in biological samples. This study shows that the magnetic properties of Fe<sub>3</sub>O<sub>4</sub>-APTES nanoparticles could be measured by MFM when they are applied in biological environment as magnetic labeling. The results obtained in this study have been included in a manuscript, which is presently in preparation.

#### 5.4.3 Study of Fe@Au Nanoparticles Incubated with Leukocytes

In order to detect the cellular uptake of MNPs, leukocytes incubated with Fe@Au nanoparticles are investigated by MFM.





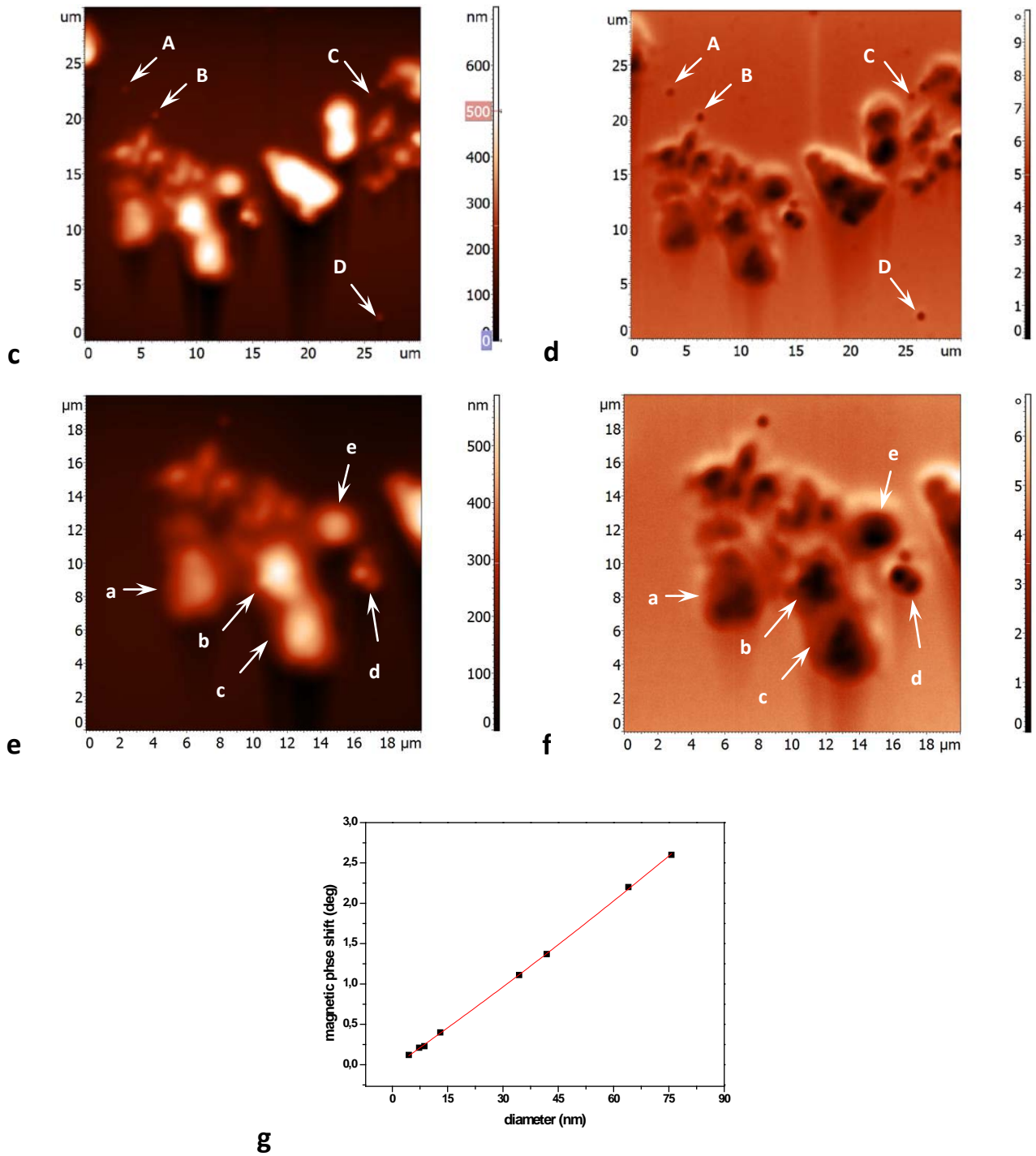


Figure 5.8 topographical image of empty cells (a) corresponding MFM phase shift image of empty cells (b) topographical reconstruction of an area featuring the cells incubated with Fe@Au nanoparticles (c) corresponding magnetic phase shift profile ( $30 \times 30 \mu\text{m}^2$ ), in which the MFM phase shift of the cellular system is evaluated (d) topographical reconstruction of the enlarged area (e) and corresponding magnetic phase shift profile ( $20 \times 20 \mu\text{m}^2$ ) (f) nanoparticles phase shift as a function of the diameter at fixed tip-sample distance  $\Delta z = 100.5 \text{ nm}$  with a linear dependence between them (g).

In Figure 5.8, not incubated cells and cells incubated with magnetic nanoparticles are detected with MFM.



The magnetic phase images are obtained with the lift height of  $\Delta z=100$  nm. As leukocytes are well known to possess an almost spherical shape [261-262], Figure 5.8a and b are bound to show residuals of cells destroyed during the preparations for AFM/MFM analysis. Anyway, the biological material not incubated with MNPs shows a small but detectable positive MFM phase contrast (about 0.2 deg), in analogy with what observed for empty niosomes in chapter 4. The source of such a positive contrast is not well understood, but it may indicate the presence of repulsive electrostatic force between the tip and cells. MFM characterization of leukocytes incubated with Fe@Au nanoparticles is presented in Figure 5.8c-f. Figure 5.8c shows the result of topographical reconstruction of an area featuring the cells, which reveals almost circular features that can be associated to residual of cells. The different shape of residual of leukocytes with and without nanoparticles is likely due to the massive "engulfment" of nanoparticles. This hypothesis is supported by the MFM phase image (Figure 5.8d), which reveals a large magnetic force gradient between tip and sample produced by the presence of large amounts of magnetic nanoparticles into the cells. A detail of the area is presented in Figure 5.8e and f (topography and MFM phase, respectively). It is worth observing that some magnetic nanoparticles not internalized in the cells are visible in Fig. 5.8c and d, four of which are indicated with letters from A to D as an example. The graph of MFM phase shift versus nanoparticles diameter at fixed lift height (Figure 5.8g) shows a pretty linear dependence. As already discussed in chapter 4, the reason of such a deviation from the model in Eq. (5.1) is not clear and further work has to be done to rationalize it. Nevertheless, this result is not an experimental artifact as demonstrated by the lack of relation between MFM phase and height in Figure 5.8e and f (as an example, five s are labeled with letters from a to e). This evidence demonstrates that the MFM phase signal in Figure 5.8d and f is produced by the presence of agglomerates of magnetic nanoparticles into the cells.

#### **5.3.4 Study of CCRF-CEM Cells Labeled with Fe<sub>3</sub>O<sub>4</sub>@Cu@Au Nanoparticles**

Morphology of the cell labeled with magnetic nanoparticles in Figure 5.9 resembles the microscopic images of CCRF-CEM cells modified with FITC-labeled PVA [263]. The ability of MFM to sense the presence of magnetic particles was investigated by lifting the cantilever up to 100.5 nm above the sample surface.

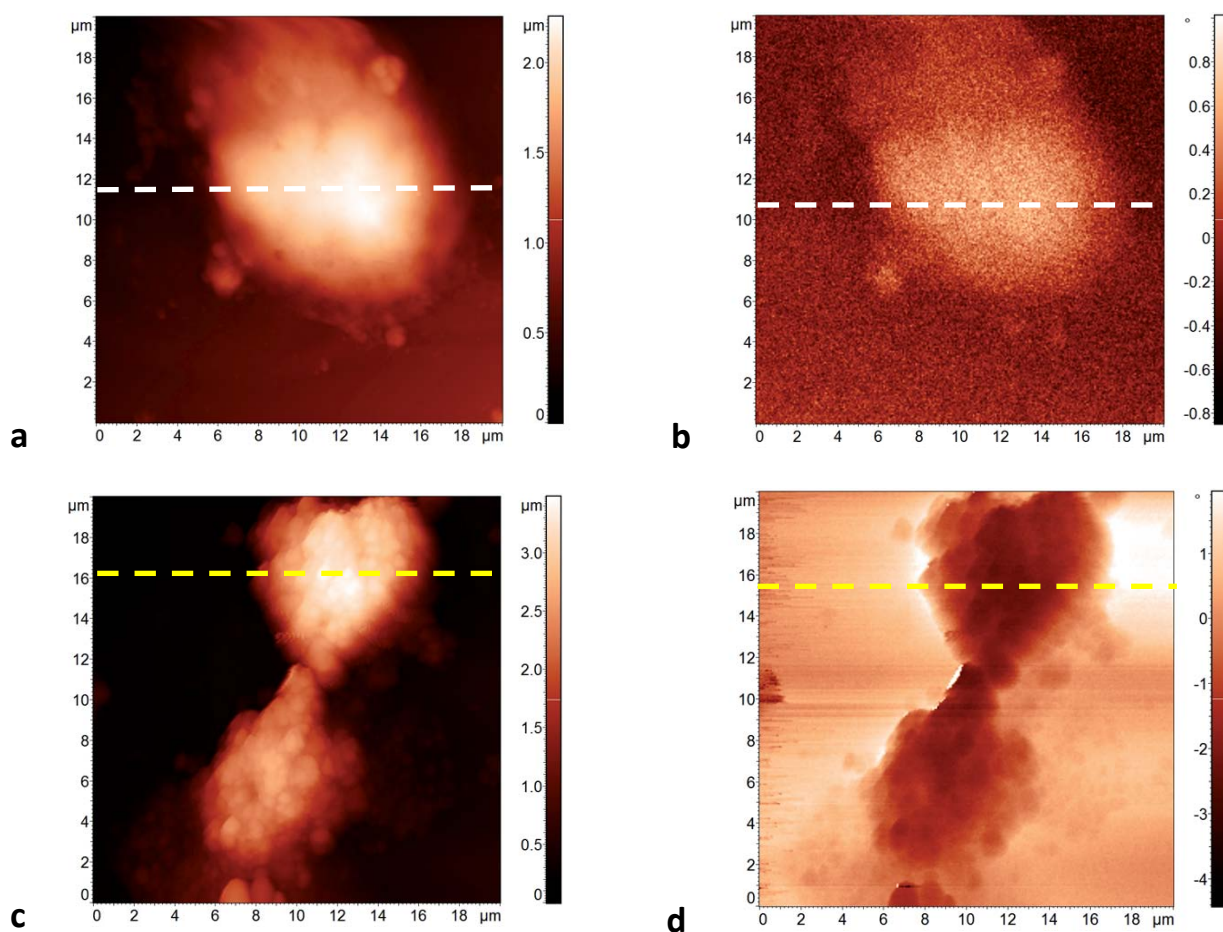


Figure 5.9 AFM topography and the corresponding MFM phase shift image of CCRF-CEM cellular system (a) topographical image of empty cells ( $20 \times 20 \mu\text{m}^2$ ); (b) corresponding MFM phase shift image of empty cells; (c) topographical reconstruction of an area featuring the cells surface modified with  $\text{Fe}_3\text{O}_4@\text{Cu}@\text{Au}$  nanoparticles ( $20 \times 20 \mu\text{m}^2$ ); (d) corresponding magnetic phase shift profile, in which the MFM phase shift of the cellular system is evaluated.

Figure 5.9a shows a typical AFM image of an empty cell. In the corresponding MFM image reported in Figure 5.9b, the cell is associated to an almost negligible positive phase shift of about 0.2 deg, which could indicate the interaction between the tip and the vesicle slightly less attractive (or more repulsive) than that between the tip and the substrate. Analogous characterization has been performed on cells labeled with  $\text{Fe}_3\text{O}_4@\text{Cu}@\text{Au}$  nanoparticles. Figure 5.9c shows an area of the sample where two individual cells are visible. The corresponding MFM image (Figure 5.9d) shows negative values of phase shift as high as some degrees, such a contrast indicating the presence of a significant attractive interaction between tip and cells. It is worth noting that the MFM phase shifts produced by the  $\text{Fe}_3\text{O}_4@\text{Cu}@\text{Au}$  nanoparticles used in this

experiment is are significant lower than those observed in Figure 5.9d.

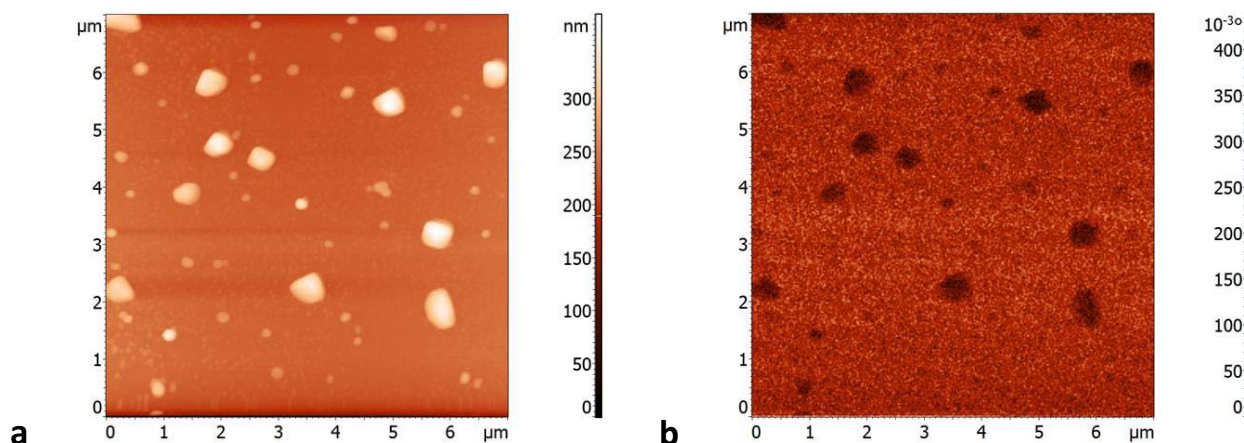


Figure 5.10 AFM/MFM characterization of  $\text{Fe}_3\text{O}_4@\text{Cu}@\text{Au}$  nanoparticles and agglomerates on a Si flat substrate: (a) topographical reconstruction of an area; (b) the corresponding MFM phase image.

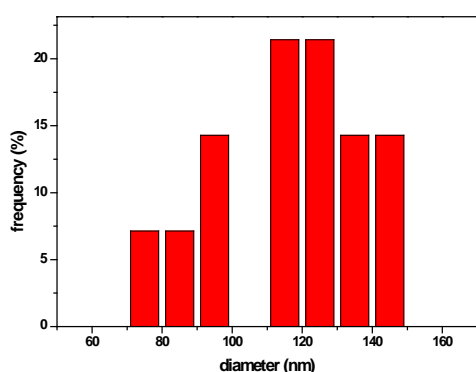


Figure 5.11 Size histogram of  $\text{Fe}_3\text{O}_4@\text{Cu}@\text{Au}$  nanoparticles

Figure 5.10 shows AFM/MFM characterization of  $\text{Fe}_3\text{O}_4@\text{Cu}@\text{Au}$  nanoparticles deposited on a Si flat substrate, the topography of an area with size  $7 \times 7 \mu\text{m}^2$  is reported where magnetic nanoparticles are clearly visible. To analyze their dimension, the height of different nanoparticles (corresponding to the nanoparticle diameter) observed on random selected area have been measured. The obtained statistics are reported in Figure 5.11 from which the diameter of nanoparticles and aggregates in any case is smaller than 150 nm. It has been reported that the size of superparamagnetic iron oxide nanoparticles could affect cell labeling efficiency [263]. In vitro research the dimension of cell labeling nanoparticles always need to be less than 150 nm. The size of nanoparticles in our research is smaller than 150 nm, so that nanoparticles could be

efficient in the cell labeling. Size is also an important factor for superparamagnetic iron oxide nanoparticles in contrast-enhanced magnetic resonance imaging. This effect is size dependent and there is linear relationship between size and magnetic phase contrast values, which is demonstrated by the study of vesicular system in chapter 4. Moreover, the hydrodynamic size of nanoparticles plays a critical role in biological application for preventing the destabilization and aggregation of superparamagnetic iron oxide nanoparticles, and can vary widely depending on the type of coating and surface modification method. This work also contributes to further improvement of the surface modification in order to obtain higher superparamagnetism and stability to generate sufficient signal in magnetic resonance required by long term tracking and imaging.

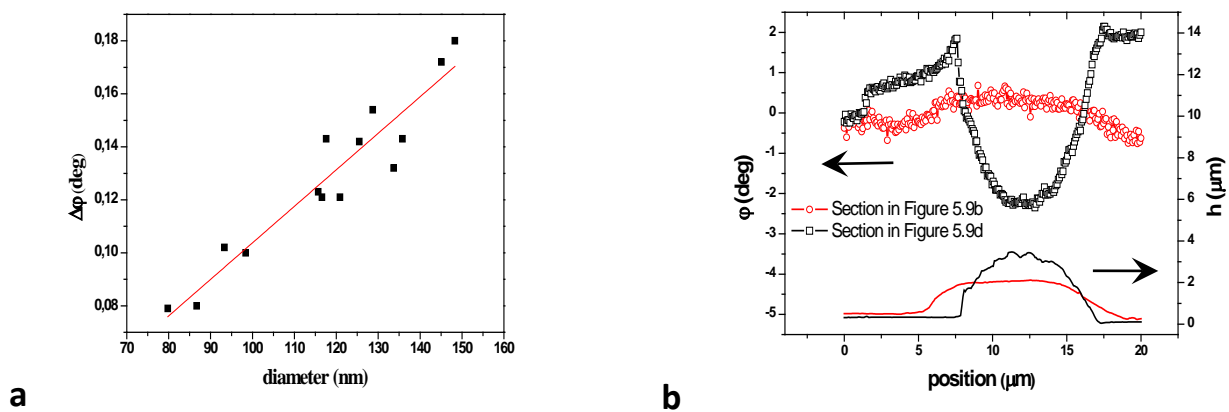


Figure 5.12 (a) nanoparticles phase shift as a function of the diameter at fixed tip-sample distance  $\Delta z = 100.5$  nm with a linear dependence between them; (b) profiles of dash line in Figure 5.9b and 5.9d extracted from the magnetic phase image together with the profile extracted from the corresponding topographic image.

The MFM phase versus diameter relation deduced from Figure 5.10b is reported in Figure 5.12a. From the sections in Figure 5.9 the height of the detected cell is about  $3.5 \mu\text{m}$  and the value of the magnetic phase shift is about 4 deg. Such a value of MFM signal, far higher than that obtained from a single nanoparticle, clearly indicates that the tip-sample interaction results from the magnetization of large agglomerates of nanoparticles. Due to their functionalization, the nanoparticles are attached to the cells surface. From Figure

5.9d, the cells surface is covered with nanoparticles. Assuming that the cell is covered by a 100 nm thick layer of nanoparticles, the measured values of MFM phase shift are compatible with the interaction of the tip with a "magnetized disk" on the cell surface. To magnetize such a large area of the sample, the tip radius should be bigger than expected. This occurrence has been actually verified with SEM analysis and blind reconstruction of the tip shape, both of which characterizations indicated a tip curvature radius as high as some hundreds of nanometers. Such a deviation of the tip geometry from the ideal one is the reason of the increased MFM contrast which nevertheless results in the reduction of spatial resolution. It is noteworthy that the analysis of cellular system, by comparing the height of cells and MFM profiles, can be used to demonstrate the presence of magnetic nanoparticles. Therefore, the use of MFM in addition to topography imaging offers an additional opportunity to distinguish specifically magnetically labeled cells. MFM detection is creating an opportunity for 3D mapping in the submembrane space, which is not possible with AFM alone. Detection of individual nanoparticles into cells still needs to be proceeded by further experiments, yet it still provides technical basis for future development of precise measurement at the physiological environment. It has been demonstrated that subnanometer-scale magnetic imaging is achievable with the use of an atomically sharp magnetic tip [264-265]. Therefore, one can expect that the use of smaller magnetic nanoparticles and a sharper MFM probe in future studies will significantly improve the lateral resolution of this method.

## **5.5 Conclusion**

In this study, MFM is applied to biological systems in air to demonstrate its potential capability to study their interactions with magnetic nanoparticles. After detecting the functionalized  $\text{Fe}_3\text{O}_4$  nanoparticles with APTES using MFM, cellular uptake behavior of Fe@Au core-shell structured magnetic nanoparticles by leukocytes and CCRF-CEM cells labeled with multishell  $\text{Fe}_3\text{O}_4$ @Cu@Au nanoparticles were investigated. Much smaller biological system-magnetoferritin molecules are detected with MFM too. These observations provided a direct evidence for the interaction of magnetic nanoparticles with biological samples, both qualitatively and quantitatively. In summary, the work in this chapter demonstrates that AFM/MFM has the

potential for the studies of biological samples in *vitro* and in *vivo* research with magnetic nanoparticles, especially in the diagnostic and therapeutic applications.

## Conclusion & Outlook

In biology and biomedicine, MFM is a relatively new technique for imaging magnetization patterns with high resolution and minimal sample preparation. The technique is an offspring of AFM and employs a sharp magnetic tip attached to a flexible cantilever. The tip is placed close to the sample surface (from some nanometers to a few micrometers) and interacts with the stray field emanating from the sample. Although a lot of effort has been done in order to get quantitative information, MFM is still predominantly a qualitative characterization technique. Magnetic force microscopy is most effectively utilized to detect and localize magnetic nanoparticles in air as well as in liquids especially in physiological environment. Even though many works have been reported which addressed the study MFM to analyze magnetic nanoparticles on substrates, its use for biological application is still not deeply explored. In this framework, the present work of thesis indicated the potential capabilities of MFM in qualitatively and quantitatively spatially localizing and characterizing nanoscale magnetic structures in biological samples.

The first results presented in this thesis demonstrated a novel MFM based approach for the accurate measurements of the thickness of soft thin films deposited on periodically patterned magnetic substrates. Then, quantification of MNPs into vesicular systems is performed for the first time using an AFM/MFM based technique in ambient environment. Our MFM based approach is a promising technique which will be improved in the future to obtain more accurate measurements and extended to the direct observation in liquids. Finally, detection of biological samples labeled with a variety of magnetic nanoparticles by MFM is presented. The study of magnetoferritin not only confirm that synthetic process resulted in the production of magnetoferritin from apoferritin using MFM phase images, but also indicate a potential improvement to quantitatively measure the magnetic momentum of single MNPs with nanometrical lateral resolution. Cellular systems (leukocytes and CCRF-CEM cells) labeled with core-shell magnetic nanoparticles were studied. Although these studies are still somehow at a preliminary stage, the capability of observing and quantifying magnetic nanoparticles in biological samples will provide useful information for better design of imaging techniques, diagnostic and therapeutic methods, especially for applications using magnetic

properties of nanomaterials, such as magnetic resonance imaging (MRI), hyperthermia, and magnetic field directed drug delivery. Also, MFM has the potential for mapping magnetic nanoparticles in the submembrane space with high lateral resolution. The deeper investigation of MFM, the development of more realistic models for the quantitative data analysis and the extension of these methodologies in liquid environment are expected to have a great potential for cell studies and for further applications of MFM in biological sciences.



# Publications

## **A.1 Thickness measurement of soft thin films on periodically patterned magnetic substrates by phase difference magnetic force microscopy (*Ultramicroscopy*136(2014)96–106)**

In this work we demonstrated an MFM-based technique that allows one to accurately measure the thickness of soft films deposited on periodically patterned magnetic substrates. The thickness is deduced comparing the phase contrast in magnetic phase images acquired on sample surface to those obtained on the substrate for different values of the tip-substrate distance. The use of the contrast in the magnetic phase images is shown to allow one to perform accurate quantitative measurements even when the absolute values of the phase do not show a clear dependence on the tip-sample distance. The accuracy of the technique depends on the spatial period and the uniformity of the magnetic domains so that samples with thickness ranging from (realistically, tens of) nanometers to about 50 microns can be characterized provided that suitable substrates are employed.

## **A.2 Visualization and quantification of magnetic nanoparticles into vesicular systems by combined atomic and magnetic force microscopy (in preparation)**

It is demonstrated that using of a novel technique based on the combination of AFM and MFM imaging that allowed us to quantitatively evaluate the amount of MNPs incorporated in single niosomes. Our approach does not require any complex preparation of the sample to be investigated. Although the number of reported measurements does not allow us to perform any statistical evaluation, we observed a not uniform incorporation of MNPs into niosome that resulted in the simultaneous presence of vesicles either empty or incorporating a significant amount of MNPs. Overall, this is the first work where a quantification of MNPs into single vesicular systems is performed using an AFM/MFM based technique. Such promising technique will be improved in the future to obtain more accurate measurements and extended to the direct observation in liquid.

### **A.3 Magnetic force microscopy for biological samples--quantitative issues (in preparation)**

MFM is applied to biological systems in air to demonstrate its potential capability to study their interactions with magnetic nanoparticles. After detecting the functionalized Fe<sub>3</sub>O<sub>4</sub> nanoparticles with APTES using MFM, cellular uptake behavior of Fe@Au core-shell structured magnetic nanoparticles by leukocytes and CCRF-CEM cells labeled with multishell Fe<sub>3</sub>O<sub>4</sub>@Cu@Au nanoparticles were investigated. Much smaller biological system-magnetoferritin molecules are detected with MFM too. These observations provided a direct evidence for the interaction of magnetic nanoparticles with biological samples, both qualitatively and quantitatively. In summary, the work in this chapter demonstrates that AFM/MFM has the potential for the studies of biological samples in *vitro* and in *vivo* research with magnetic nanoparticles, especially in the diagnostic and therapeutic applications.

### **A.4 Other works still going on**

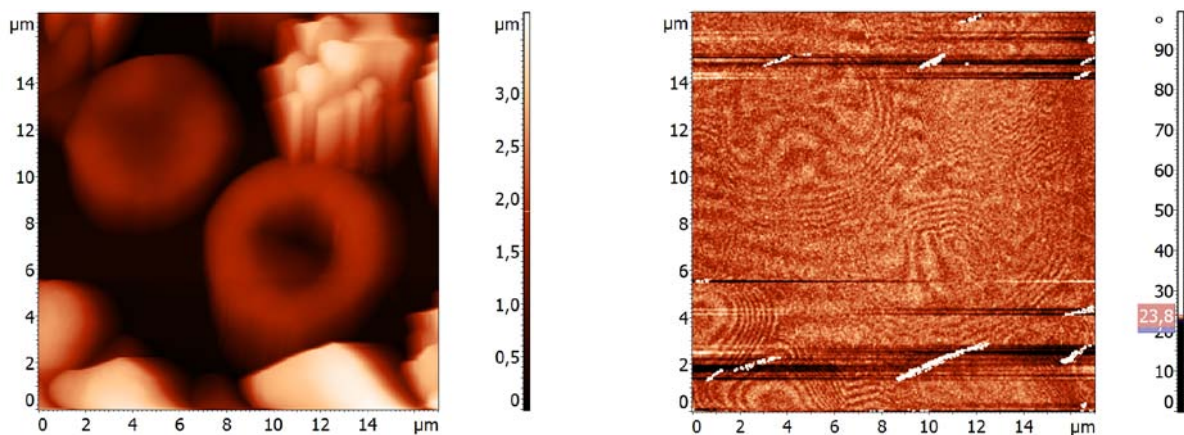
#### **A.4.1 Quantitative characterization of the magnetic properties of individual magnetic nanoparticles**

Depending on the work of chapter 3 to investigate the thickness of thin film with PD-MFM, we foresee that PD-MFM could be used to measure  $\chi_m$  of single superparamagnetic nanoparticles deposited on periodically patterned magnetic substrates as far as  $\chi_m$  is large enough the contribution of the magnetic properties of the particle is detectable with PD-MFM. Since PD-MFM relies on the measurement of the difference between maxima and minima of the MFM phase signal, it needs to search for two similar nanoparticles on the magnetic phase stripe of one maximum and one minimum, respectively. Then, MFM images should be collected at different values of lift height and the calibration curves of phase shift versus tip-sample distance should be obtained. At first, the  $\Delta\phi(\Delta z)$  curve collected on the area free from the nanoparticles can be fitted using Eq. (3.7) with  $h=0$  to determine  $A_d$  and  $\xi_0$ . Then, after measuring the nanoparticles height from topographical reconstruction, the  $\Delta\phi(\Delta z)$  curve of the magnetic nanoparticles can be fitted using the model described in Appendix B to obtain  $\chi_m$ . Additional to the possibility to investigate the magnetic properties of

single particles, a significant advantage of PD-MFM compared with simple MFM for the measurement of  $\chi_m$  of nanoparticles is that the character of the tip is not required. This proposing experiment will be performed in the next work.

#### A.4.2 Further investigation of cellular system labeled with magnetic nanoparticles

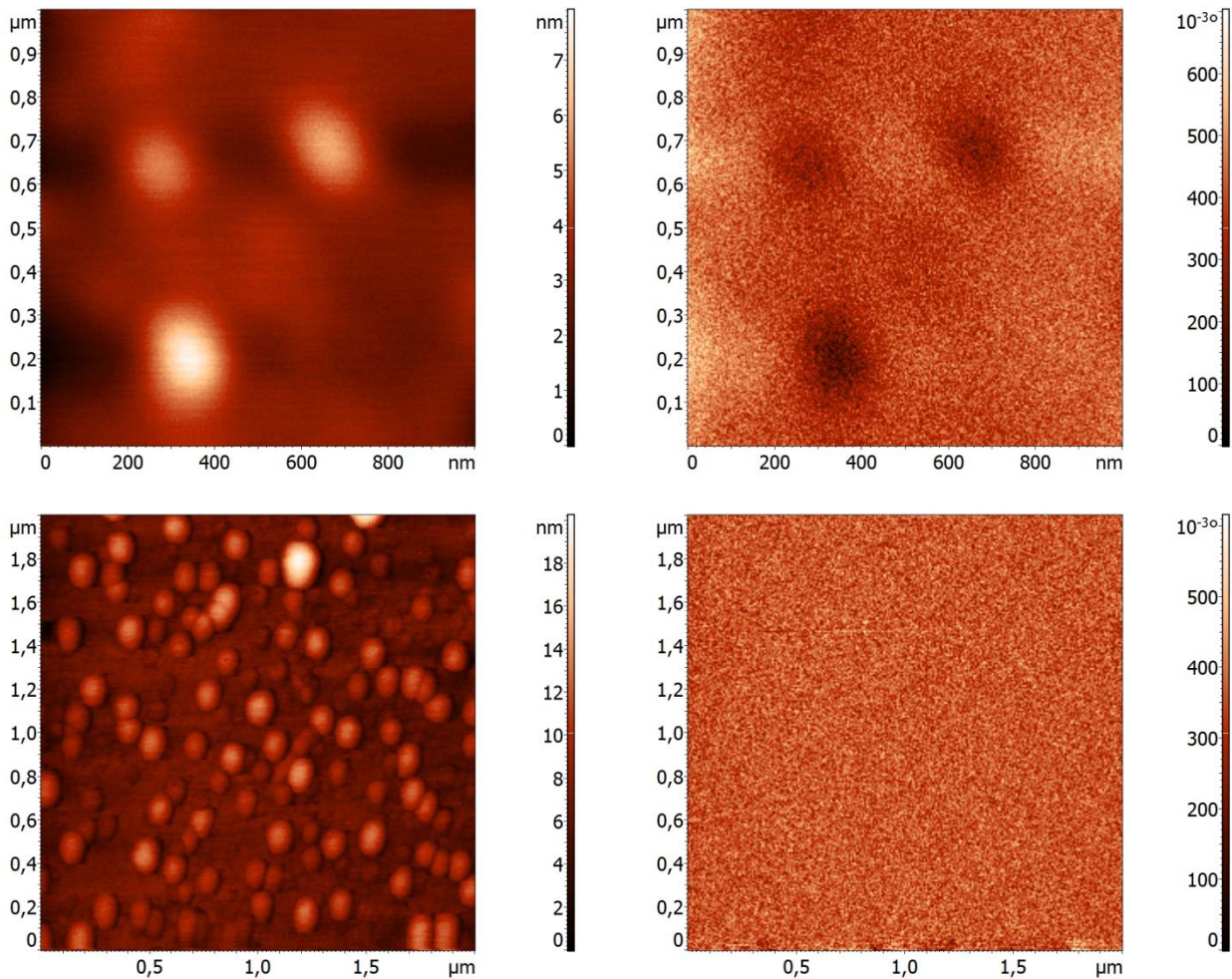
As the work has been shown in chapter 5, the human leukocytes cells labeled with double shell iron oxide nanoparticles will be investigated again depending on the successful sample preparation, since the magnetic recognition has been revealed with MFM characterization. Meanwhile, human red blood cells (RBCs) of different group (B and O) incubated with magnetic nanoparticles will be performed. Up to now, the detection of group O red blood cells has been carried out. From the images presented below, the topography of two individual red blood cells definitely confirms that the measures of red blood cells measured with the AFM are in correspondence to that reported in the literature. Red blood cells are known for their characteristic shape of a biconcave disc that has a thickness of 0.8  $\mu\text{m}$  and 1.9  $\mu\text{m}$  in the center to the periphery. The dimensions are quite variable: on average are around 7.5  $\mu\text{m}$  in diameter, but can be up to 9  $\mu\text{m}$  (becoming macrocytes) and 6  $\mu\text{m}$  (microcytic). Corresponding magnetic image does not show significant magnetic response, which indicates that the weak magnetic interaction between the O type of RBCs and the functionalized magnetic nanoparticles with ligand, in other words, this ligand cannot used as the cell surface receptor of RBCs. The B type of RBCs will be investigated in the further experiments.



#### A.4.3 Characterization of core-shell magnetic nanoparticles labeled with fluorescence

The detection of magnetic nanoparticles coated with TEXAS RED (TR) was performed with MFM. The

images have been shown in the first row.  $\text{Fe}_3\text{O}_4$ +TR nanoparticles with very small diameter about 5 nanometers are present, corresponding magnetic phase contrast is clearly visible. Conversely, images of Fe+TR nanoparticles functionalized with SUR by MFM have been shown in second row, even though bigger size nanoparticles appear in the topography, no visible magnetic contrast is detected from the corresponding magnetic image. The results need to be verified by fluorescent microscopy to reveal the surface ligand effect of SUR. As well  $\text{Fe}_3\text{O}_4$ +TR+SUR and Fe+TR have the need to be characterized with MFM as a comparison. This study will contribute to further improvement of the surface modification in membrane filtration in order to obtain higher superparamagnetism and stability to generate sufficient signal in magnetic resonance required by long term tracking and imaging.



# Appendix

## Appendix A. Correction due to the magnetic field produced by a paramagnetic/diamagnetic infinitely extended film

Consider a periodically magnetized floppy disk, which is modeled as an infinite slab parallel to the  $xy$  plane of thickness  $b$ . We consider, in addition, a diamagnetic film of thickness  $c$  lying on top of the floppy.

### A.1. Magnetic field generated by the floppy disk

Assuming that only first harmonics significantly contribute to the Fourier series of the floppy magnetization, the magnetic field above the disk can be calculated as  $B_0(r) = B_{oy}(r)\hat{y} + B_{oz}(r)\hat{z}$  with

$$B_{oy}(y,z) = -B_1 e^{-kz} \cos(ky + \delta_1)$$

$$B_{oz}(y,z) = B_1 e^{-kz} \sin(ky + \delta_1) \tag{A.1}$$

where  $k = 2\pi/\lambda$  is the wave number associated with the magnetization spatial period  $\lambda$ ,  $\delta_1$  is a phase shift, and the explicit expression for  $B_1$  can be found in Ref. [160]. Here, we have taken the origin of the  $z$ -axis at the boundary between the floppy and the film.

### A.2. Magnetization of the film

We assume that, anywhere within the film, the film magnetization vector  $M$  will align to the external field  $B_0$  (that is the one solely due to the floppy). In other words, we assume that the magnetization of the floppy disk, hence the corresponding field  $B_0$ , is the same as in the absence of the film. Thereby  $M(x, z) = \gamma B_0(x, z)$  for any  $r = (x, y, z)$  such that  $0 \leq z \leq c$ , where we have set  $\gamma = \chi_m/\mu$  with  $\chi_m(\mu)$  being the magnetic susceptibility (permeability) of the film material.

Hence, this and Eq. (A.1) trivially give

$$M_y(y,z) = -\gamma B_1 e^{-kz} \cos(ky + \delta_1)$$

$$M_z(y,z) = \gamma B_1 e^{-kz} \sin(ky + \delta_1) \tag{A.2}$$

where we recall that  $0 \leq z \leq c$  (otherwise  $M$  vanishes).

### A.3. Scalar magnetic potential due to the film

The scalar magnetic potential generated by a magnetic medium is in general given by [160]

$$\Psi(r) = -\frac{\mu_0}{4\pi} \int_V d^3r' \frac{\nabla' \cdot M(r')}{|r-r'|} + \frac{\mu_0}{4\pi} \oint_S d^2r' \frac{M(r') \cdot \hat{n}}{|r-r'|} \quad (\text{A.3})$$

where the first (second) integral is over the volume occupied by the magnetic medium (the external surface) and  $r'$ , as usual, is a generic of the magnetic source. Using Eq. (A.2), it is straight forward to check that  $\nabla' \cdot M(r') = 0$  identically, hence the first integral vanishes and we are left with the surface integral only. The external surface of the film is clearly the union of the planes  $\pi_1$  and  $\pi_2$  defined by  $z' = 0$  and  $z' = c$ , respectively. The corresponding unit vectors are  $\hat{n}_1 = \hat{z}$  and  $\hat{n}_2 = -\hat{z}$ , which thus yield  $M(r') \cdot \hat{n}_1 = M_z(y', 0)$  and  $M(r') \cdot \hat{n}_2 = -M_z(y', c)$ . We are interested in calculating the potential due to the film  $\psi_f(r)$  on a  $P$  having coordinates  $(0,0, z)$ . Using this, the distance of  $P$  from plane  $\pi_1(\pi_2)$  reads

$|r-r'| = \sqrt{x'^2 + y'^2 + z^2}$  ( $|r-r'| = \sqrt{x'^2 + y'^2 + (z-c)^2}$ ). Therefore, with the help of Eq. (A.2), in the present case

$$\Psi_f(z) = -\frac{\mu_0}{4\pi} \int_{-\infty}^{+\infty} dx' \int_{-\infty}^{+\infty} dy' \frac{\gamma \mathcal{B}_1 \sin(ky' + \delta_1)}{\sqrt{x'^2 + y'^2 + z^2}} + \frac{\mu_0}{4\pi} \int_{-\infty}^{+\infty} dx' \int_{-\infty}^{+\infty} dy' \frac{\gamma \mathcal{B}_1 e^{-kc} \sin(ky' + \delta_1)}{\sqrt{x'^2 + y'^2 + (z-c)^2}} \quad (\text{A.4})$$

we thus need to compute the double integral

$$I(z_0) = \int_{-\infty}^{+\infty} dx' \int_{-\infty}^{+\infty} dy' \frac{\sin(ky' + \delta_1)}{\sqrt{x'^2 + y'^2 + (z-z_0)^2}} \quad (\text{A.5})$$

where  $z \geq z_0$ . Setting  $\delta_1 = \pi/2$  (which ensures that the  $P$  lies above the maximum of  $M_z$ ) the integral over  $y'$  is easily computed in terms of a modified Bessel function as

$$I(z_0) = \int_{-\infty}^{+\infty} dx' \int_{-\infty}^{+\infty} dy' \frac{\cos(ky')}{\sqrt{x'^2 + y'^2 + (z-z_0)^2}} = 2 \int_{-\infty}^{+\infty} dx' K_0(k\sqrt{x'^2 + (z-z_0)^2}) = 4 \int_0^{+\infty} dx' K_0(k\sqrt{x'^2 + (z-z_0)^2}),$$

(A.6)

where  $K_0$  is the 0th-order modified Bessel function of the second kind. The remaining integral over  $x'$  can be computed using Eq. (6.596-3) in Ref. [169]

$$\int_0^{+\infty} dx' K_\nu(\alpha\sqrt{x'^2+z^2}) \frac{x'^{2\mu+1}}{\sqrt{(x'^2+z^2)^\nu}} = \frac{2^\mu \Gamma(\mu+1)}{\alpha^{\mu+1} z^{\nu-\mu-1}} K_{\nu-\mu-1}(\alpha z) \quad (\alpha > 0, \text{Re } \mu > -1). \quad (\text{A.7})$$

In our case:  $\mu = -0.5$ ,  $\nu = 0$  and we end up with the simple formula

$$I(z_0) = \frac{2\pi}{k} e^{-k(z-z_0)} \quad (\text{A.8})$$

This together with Eqs. (A.4) and (A.5) yields the magnetic potential as

$$\Psi_f(z) = \frac{\mu_0 \gamma \mathcal{B}_1}{4\pi} [-I(0) + e^{-kc} I(c)] = 0 \quad (\text{A.9})$$

Hence, the contribution to the magnetic field due to the film vanishes on P.

## Appendix B. Correction due to the magnetic field produced by a paramagnetic/diamagnetic sphere

Consider a periodically magnetized floppy disk, which is modeled as an infinite slab parallel to the  $xy$  plane of thickness  $b$ . We consider, in addition, a diamagnetic sphere of radius  $R$  lying on top of the floppy with the center placed in correspondence of a maximum of the component along  $z$  of the magnetic field generated by the floppy. For the calculation, it is useful to define a Cartesian reference frame whose origin is at the center of the sphere. By hypothesis, the sphere radius is far shorter than the floppy magnetization spatial period (this complies with the typical scales in our experiment).

### B.1. Magnetic field generated by the floppy disk

Assuming that only first harmonics significantly contribute to the Fourier series of the floppy magnetization, the magnetic field above the disk can be calculated as  $B_0(r) = B_{oy}(r)\hat{y} + B_{oz}(r)\hat{z}$  with

$$\begin{aligned} B_{oy}(y, z) &= -B'_1 e^{-kz} \cos(ky + \delta_1) \\ B_{oz}(y, z) &= B'_1 e^{-kz} \sin(ky + \delta_1) \end{aligned} \quad (\text{B.1})$$

where  $k = 2\pi/\lambda$  is the wave number associated with the magnetization spatial period  $\lambda$ ,  $\delta_1$  is a phase shift, and  $B'_1 = B_1 e^{-kR}$  the explicit expression for  $B_1$  can be found in Ref. [160].

### B.2. Magnetization of the sphere

We assume that, anywhere within the sphere, the sphere magnetization vector  $M$  will align to the floppy-disk field  $B_0$  (that is the one solely due to the floppy). In other words, we assume that the magnetization of the floppy disk, hence the corresponding field  $B_0$ , is the same as in the absence of the diamagnetic sphere. Thereby

$$M(x, z) = \gamma B_0(x, z) \quad (\text{B.2})$$

for any  $r = (x, y, z)$  such that  $x^2 + y^2 + z^2 \leq R^2$ , where we have set  $\gamma = \chi_m/\mu$  with  $\chi_m(\mu)$  being the magnetic susceptibility (permeability) of the sphere material. Hence, this and Eq.(B.1) trivially give



$$M_y(y,z) = -\gamma B_1 e^{-kz} \cos(ky + \delta_1)$$

$$M_z(y,z) = \gamma B_1 e^{-kz} \sin(ky + \delta_1) \quad (\text{B.3})$$

however, using now that  $R/\lambda \ll 1$  and observing that  $\lambda$  is the characteristic length entering both  $e^{-kz}$  and the sinusoidal functions,  $M_y$  and  $M_z$  are well approximated by the respective Taylor expansions up to second order in  $y$  and  $z$ . This together with  $\delta_1 = \pi/2$ , which ensures that the sphere is centered on the maximum value of  $M_z$  according to Eq. (B.3), yields

$$M_y(y, z) \approx \gamma B_1 k y (1 - kz)$$

$$M_z(y, z) \approx \gamma B_1 (2 - k^2 y^2) [kz(kz - 2) + 2] / 4 \quad (\text{B.4})$$

We will use these approximated expressions to evaluate the surface integral in the next section.

### B.3. Scalar magnetic potential due to the sphere

In the light of Eq. (A.3), just like the case tackled in A.1, the volume integral vanishes due to  $\nabla' \cdot \mathbf{M}(r') = 0$  and we are left with surface integral only [second term in Eq. (A.3)]. To compute this, it is convenient to refer to spherical coordinates in such a way that a generic point on the surface of the sphere has coordinates

$$x' = R \sin \theta \cos \phi, \quad y' = R \sin \theta \sin \phi, \quad z' = R \cos \theta \quad (\text{B.5})$$

where  $0 \leq \theta \leq \pi$  and  $0 \leq \phi \leq 2\pi$  while the unit vector normal to the surface clearly reads

$$\hat{n} = \hat{n}(\theta, \phi) = (\sin \theta \cos \phi, \sin \theta \sin \phi, \cos \theta) \quad (\text{B.6})$$

We are interested in calculating the potential  $\psi_s(r)$  on a point  $P$  lying above the sphere along its symmetry axis, i.e., having coordinates  $r = (0, 0, z)$  with  $z \geq R$ . It is easily checked then that for a given point  $r' \leftrightarrow (\theta, \phi)$  on the spherical surface, the distance of this from  $P$  is given by

$$|r - r'| = \sqrt{(R \sin \theta)^2 + (z - R \cos \theta)^2} \quad (\text{B.7})$$

Using all the above along with  $d^2 r' = R^2 \sin \theta \, d\theta \, d\phi$ , the second term in Eq. (A.3) in our case reads

$$\Psi_S(z) = \frac{\mu_0}{4\pi} \int_0^\pi \int_0^{2\pi} d\theta d\phi R^2 \sin^2 \theta \frac{M_y(y', z')n_y + M_z(y', z')n_z}{\sqrt{(R \sin \theta)^2 + (z - R \cos \theta)^2}} \quad (\text{B.8})$$

Replacing now the approximated expressions for  $M_y$  and  $M_z$  [see Eq. (B.4)], the double integral can be calculated exactly and we thus end up with

$$\Psi_S(z) \approx \gamma B'_1 \mu_0 R^3 \frac{k^3(-4R^6 + 3R^4 z^2 + 21R^2 z^4) + 45k^2 R^4 z - 126kR^2 z^2 + 210z^3}{630z^5} \quad (\text{B.9})$$

where we have neglected terms proportional to  $(kR)^n$  with  $n > 2$ .

#### B.4. Magnetic-field deviation due to the sphere

Since  $B_{sz}(z) = -\partial \Psi_S(z) / \partial z$ , we therefore conclude

$$\varphi_S \propto -\frac{d\Psi_S}{dz^3} = \gamma B'_1 \mu_0 R^3 \frac{[k^3(-140R^6 + 30R^4 z^2 + 21R^2 z^4) + 900k^2 R^4 z - 1260kR^2 z^2 + 840z^3]}{105z^8} \quad (\text{B.10})$$

where  $\varphi_S$ , as is known, quantifies the measured MFM signal due to the sphere. To estimate the correction to the overall magnetic field due to the sphere, we have to compare  $\varphi_S$  with  $\varphi_0 \propto d^2 B_{0z} / dz^2 = k^2 B_{0z}(0, z)$  [Eq. (B.1)]. The absolute value of the ratio thus reads

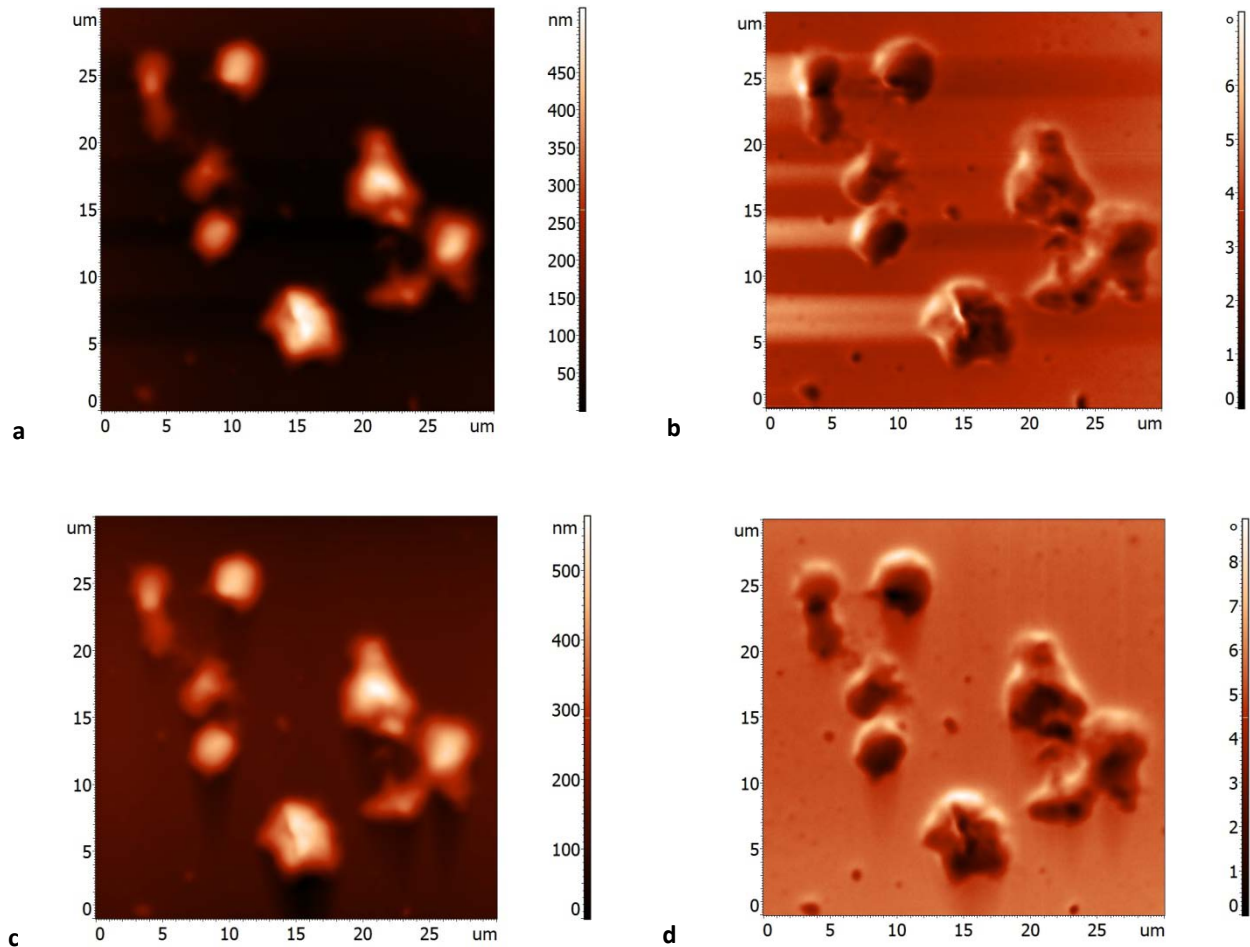
$$\left| \frac{\varphi_S}{\varphi_0} \right| = (1 - \mu_r) e^{kz} R^3 \frac{|-900k^2 z R^4 + 1260kz^2 R^2 - 840z^3 + k^3(140R^6 - 30z^2 R^4 - 21z^4 R^2)|}{105k^2 z^8} \quad (\text{B.11})$$

where  $\mu_r = \mu / \mu_0$  is the relative permeability of the medium. In a paradigmatic situation ( $R = 100 \text{ nm}$ ,  $\lambda = 2\pi/k = 1 \text{ } \mu\text{m}$ ,  $\mu_r = \mu_{\text{water}} = 0.999992$ ) we see that the ratio monotonically decreases with  $z$ . In the worst case, namely the (unrealistic) circumstance where  $\Delta z = 0$  (top of the sphere), it thus turns out that the relative correction to the overall MFM signal due to the sphere is about  $1.4 \times 10^{-4}$ . This witnesses that such a correction can be taken as negligible for all practical purpose.

## Appendix C

During the measurement of MFM unexpected results caused by scanning effects were discovered. Different scanning direction of MFM performance and the damage of the apex of tip will result in distinguish images.

### A Effect of scanning direction of MFM



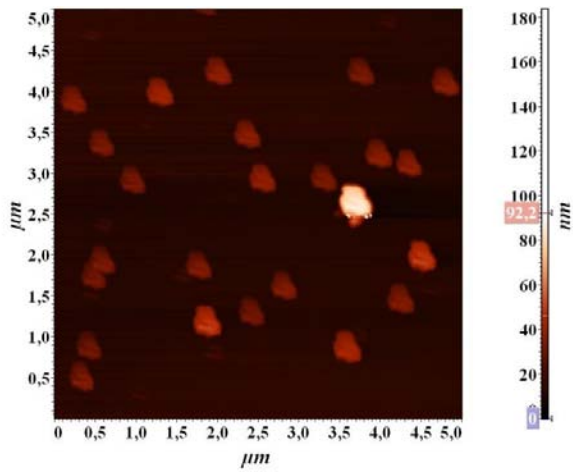
Effects of imaging at different scan direction, a) and b) is the horizontal scanning image for topography and magnetic phase, respectively; c) and d) is the vertical scanning image for topographical reconstruction and magnetic phase imaging, respectively.

Figure above shows the images with stripe appearance of different scan direction. Figure a-b are the images at horizontal scanning direction from bottom to top for topographical reconstruction and magnetic phase imaging, respectively; conversely, Figure c-d are the images at vertical scanning direction from left to right. In these images, when the scanning direction is horizontal, there appears some strips followed the cells during the scanning, while this

phenomenon disappeared during vertical scanning. Previous study shows that stripe noise could occur using tapping mode of atomic force microscopy [266]. These stripes change subjectively to a variety of factors, such as sample preparation conditions and the constituents on the substrate. In particular, sharp and irregular boundaries or protuberances in the object distribution usually produce stripes across the image. Noise reduction from striped images by frequency-based algorithm simulation method for removing stripe noises mainly in atomic force microscopy images was reported [267], enhancing more precise features in the topographic measurements. As well we have to make more efforts to construct magnetic figures for MFM. Meanwhile, it has been discovered that the edge effect of the cells appears in the magnetic phase images while scanning. The magnetic phase images show certain edge effects at the very border of cells during scanning, which is very similar as the effects of MFM scanning in Figure 5.8. The evolution of magnetic contrast between the empty cells and the non-magnetic substrate is well visible in Figure 5.8. Specifically, the inner area of the cells becomes darker, while the border brighter. The bright border indicates an evidence of the inversion of the stray-field flux lines in proximity of the border of the cells, which is similar with the study of Shen et al in 2009 [248]. The edge effect usually appears during the technique proceeding, which leads to the presence of domains at the edge of cells and provides a reverse domain from which to switch easily the magnetization of the rest of cells. Theoretically, any abrupt increase of the force between samples and the tip would make a dramatic change in the tip vibration, thus the noise cannot stay constant during the scanning; moreover these noise errors cannot be averaged off. However, no matter what the scanning direction is, the correct topographical and phase contrast data can be collected.

## **B Artifact of the tip**

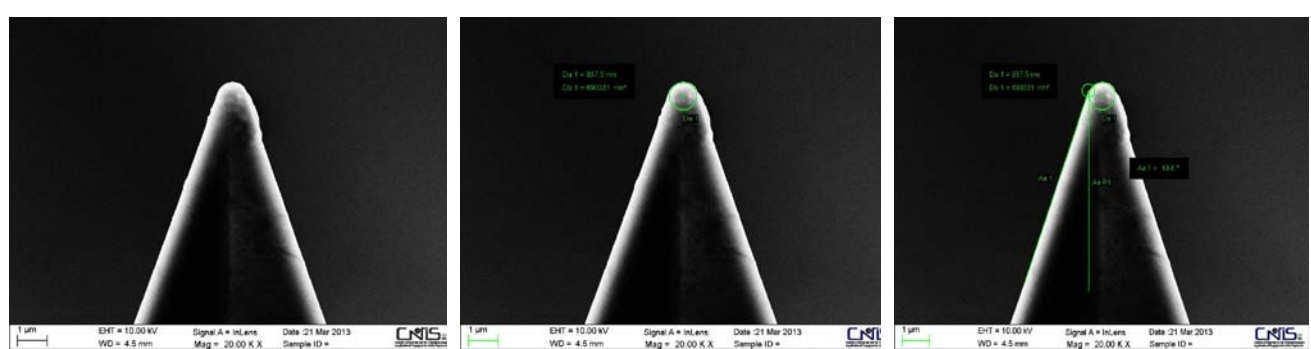
During the study in chapter 5, magnetic tip often encounters artifacts due to damage to the apex of the tip, which implies the presence of all specimen with the same morphology in the images.

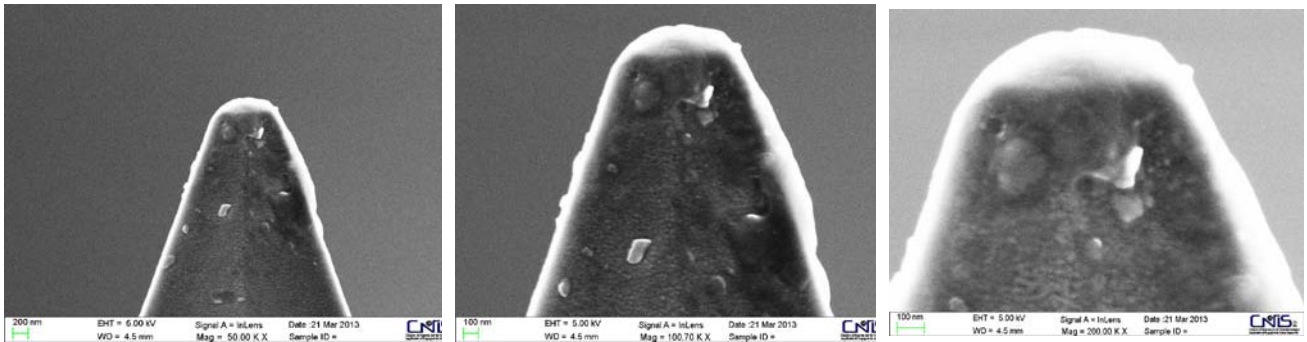


Sample image of topography affected by an artifact due to the damage of the tip apex.

Figure above shows sample image of topography affected by an artifact due to the damage of the tip apex. Similar problem happens in Figure 5.3. This shows that the tip becomes worn or if debris attaches itself to the end of the tip. What is really being imaged is the worn sharp of the tip or the shape of the debris, not the morphology of the surface features.

The structures that appear as the same shape of particles are generally in the same image or images realized in a short time, having very similar conformations from each other. This type of artifact could be attributed to: a) damage to the tip, as shown below; b) accesion on the tip, probably due to magnetic effect of small particles (and, given the "globular" structures observed, this seems to be the most plausible hypothesis). To support this hypothesis, however, we should make more additional measurements.





### Scanning electron microscopy images of a destroyed magnetic tip

The tip with a bad configure situation during the measurements is shown in the figure above, with the tip not figured well for detecting nanoscale samples. The radius of the tip is supposed to be no more than 50nm, but here according to SEM results, this value has reached 937.5 nm, which exceeds the standard parameter largely, and will directly lead to dissatisfied results. This indicates the resolution achieved with MFM is partially determined by the effective probe size, as its geometry and composition play a critical role in generating MFM images of samples. Tip-imaging artifacts or convolution may occur if the scanning tip is less sharp than the profile of the object at that . When the scanning tip is sharper than the feature on the sample, the true profile of the feature could be obtained. However, the use of very sharp tips would more likely results in cell damage.

# References

- [1] Neves, CS., Quaresma, P., Baptista, PV., Carvalho, PA., Pedro, AJ., Pereira, E., Eaton, P., "New insights into the use of magnetic force microscopy to discriminate between magnetic and nonmagnetic nanoparticles." *Nanotechnology*, 21(30), 305 (2010).
- [2] Giepmans, B. N., S. R. Adams, ., R. Y. Tsien, "The fluorescent toolbox for assessing protein location and function." *Science*. 312:217–224 (2006).
- [3] Bertorelle F., Wilhelm C., Roger J., Gazeau F., Menager C. & Cabuil V, "Fluorescence-modified superparamagnetic nanoparticles: Intracellular uptake and use in cellular imaging" *Langmuir*, 22, 5385–5391 (2006).
- [4] Sun, S.H. & Zeng, H., "Size-controlled synthesis of magnetite nanoparticles" *Journal of the American Chemical Society*, 124(28), 8204–8205 (2002).
- [5] Bergey, E.J., Levy, L., Wang, X.P., Krebs, L.J., Lal, M., Kim, K.S., Pakatchi, S., Liebow, C. & Prasad, P.N., "DC magnetic field induced magnetocytolysis of cancer cells targeted by LH-RH magnetic nanoparticles in vitro" *Biomedical Microdevices*, 4(4), 293–299 (2002).
- [6] A. Hopt and E. Neher, "Highly nonlinear photodamage in two-photon fluorescence microscopy" *Biophysical Journal* 80(4), 2029-2036 (2001).
- [7] S Schreiber, M Savla, DV Pelekhov, DF Iscru, "Magnetic Force Microscopy of Superparamagnetic Nanoparticles" *small*, 4, 2, 270–278 (2008).
- [8] A.-H. Lu, E.L. Salabas, F. Schüth, "Magnetic Nanoparticles: Synthesis, Protection, Functionalization and Application" *Angew. Chem. Int. Ed.* 46, 1222-1244 (2007).
- [9] R.M. Cornell, U. Schwertmann, "The Iron Oxides: Structure, Properties, Reactions, Occurrences and Uses" 2nd ed.; Wiley-VCH: Weinheim, (2003).
- [10] G Fang, Y Si, C Tian, G Zhang, D Zhou, "Degradation of 2,4-D in soils by Fe<sub>3</sub>O<sub>4</sub> nanoparticles combined with stimulating indigenous microbes" *Environmental Science and Pollution Research* 19:784–793 (2012).
- [11] Jianshuai Mu, Yan Wang, "Intrinsic peroxidase-like activity and catalase-like activity of Co<sub>3</sub>O<sub>4</sub> nanoparticles" *Chem. Commun.*, 48, 2540-2542 (2012).
- [12] Jingjing Yuan, Junwu Zhu, "Graphene-based 3D composite hydrogel by anchoring Co<sub>3</sub>O<sub>4</sub> nanoparticles with enhanced electrochemical properties" *Phys. Chem. Chem. Phys.*, 15, 12940-12945 (2013).
- [13] Eric C. Tyo, Chunrong Yin, "Oxidative Dehydrogenation of Cyclohexane on Cobalt Oxide (Co<sub>3</sub>O<sub>4</sub>) Nanoparticles: The Effect of Particle Size on Activity and Selectivity" *ACS Catal.*, 2(11), 2409–2423 (2012).
- [14] X. Meng, H. Li, J. Chen, L. Mei, K. Wang, X. Li, "Mössbauer study of cobalt ferrite nanocrystals substituted with rare-earth Y<sup>3+</sup> ions" *J. Magn. Magn. Mater.* 321, 1155 (2009).
- [15] Z. Zi, Y. Sun, X. Zhu, Z. Yang, J. Dai, W. Song, "Synthesis and magnetic properties of CoFe<sub>2</sub>O<sub>4</sub> ferrite nanoparticles" *J. Magn. Magn. Mater.* 321, 1251 (2009).
- [16] L.X. Phua, F. Xu, Y.G. Ma, C.K. Ong, "Structure and magnetic characterizations of cobalt ferrite films prepared by spray pyrolysis" *Thin Solid Films*. 517, 5858 (2009).
- [17] Bronislav E. Kashevsky, V.E. Agabekov, S.B. Kashevsky, K.A. Kekalo, E.Y. Manina, I.V. Prokhorov,

V.S. Ulashchik, "Study of cobalt ferrite nanosuspensions for low-frequency ferromagnetic hyperthermia" *Particuology* 6, 322 (2008).

[18] CI Olariu, HHP Yiu, L Bouffier, T Nedjadi, "Multifunctional Fe<sub>3</sub>O<sub>4</sub> nanoparticles for targeted bi-modal imaging of pancreatic cancer" *J. Mater. Chem.*, 21, 12650-12659 (2011).

[19] J Zhou, X Qiao, BP Binks, K Sun, M Bai, Y Li, Y Liu, "Magnetic Pickering Emulsions Stabilized by Fe<sub>3</sub>O<sub>4</sub> Nanoparticles" *Langmuir*, 27 (7), 3308–3316 (2011).

[20] Kang, E., Jung, Y. S., Cavanagh, A. S., Kim, G.-H., George, S. M., Dillon, A. C., Kim, J. K. and Lee, J., "Fe<sub>3</sub>O<sub>4</sub> Nanoparticles Confined in Mesocellular Carbon Foam for High Performance Anode Materials for Lithium-Ion Batteries" *Adv. Funct. Mater.*, 21, 2430–2438 (2011).

[21] Y.F. Shen, J. Tang, Z. H. Nie, "Preparation and application of magnetic Fe<sub>3</sub>O<sub>4</sub> nanoparticles for wastewater purification" *Separation and Purification Technology* 68, 312–319 (2009).

[22] U Tamer, Y Gündoğdu, İH Boyacı, K Pekmez, "Synthesis of magnetic core-shell Fe<sub>3</sub>O<sub>4</sub>-Au nanoparticle for biomolecule immobilization and detection" *Journal of Nanoparticle Research*, 12, Issue 4, 1187-1196 (2010).

[23] Hafsa Khurshid, Sayan Chandra, "Synthesis and magnetic properties of core/shell FeO/Fe<sub>3</sub>O<sub>4</sub> nano-octopods" *J. Appl. Phys.* 113, 17B, 508 (2013).

[24] Hye-Young Park, Mark J. Schadt, "Fabrication of Magnetic Core@Shell Fe Oxide@Au Nanoparticles for Interfacial Bioactivity and Bio-separation" *Langmuir*, 23, 9050-9056 (2007).

[25] Hemei Chen, Chunhui Deng, "Synthesis of Fe<sub>3</sub>O<sub>4</sub>@SiO<sub>2</sub>@PMMA Core-Shell-Shell Magnetic Microspheres for Highly Efficient Enrichment of Peptides and Proteins for MALDI-ToF MS Analysis" *Angew. Chem. Int. Ed.*, 49, 607–611(2010).

[26] Carmen Vogt, Muhammet S. Toprak, "High quality and tuneable silica shell-magnetic core nanoparticles" *Journal of Nanoparticle Research*, 12, 4, 1137-1147, (2010).

[27] Tea-Jong Yoon, Kyeong Nam Yu, Specific Targeting, "Cell Sorting, and Bioimaging with Smart Magnetic Silica Core-Shell Nanomaterials," *Small* 2, 2, 209–215, (2006).

[28] CL Wu, H He, HJ Gao, G Liu, RJ Ma, YL An, "Synthesis of Fe<sub>3</sub>O<sub>4</sub>@SiO<sub>2</sub>@polymer nanoparticles for controlled drug release" *Science China Chemistry*, 53, 3, 514-518, (2010).

[29] FH Chen, LM Zhang, QT Chen, Y Zhang, ZJ Zhang, "Synthesis of a novel magnetic drug delivery system composed of doxorubicin-conjugated Fe<sub>3</sub>O<sub>4</sub> nanoparticle cores and a PEG-functionalized porous silica shell" *Chem. Commun.*, 46, 8633-8635 (2010).

[30] Dianping Tang, Ruo Yuan, "Magnetic Core-Shell Fe<sub>3</sub>O<sub>4</sub>@Ag Nanoparticles Coated Carbon Paste Interface for Studies of Carcinoembryonic Antigen in Clinical Immunoassay" *J. Phys. Chem. B*, 110 (24), 11640–11646 (2006).

[31] Carly S. Levin, Cristina Hofmann, "Magnetic-Plasmonic Core-Shell Nanoparticles" *ACS Nano*, 2009, 3 (6), 1379–1388.

[32] Xiong Wen Lou, Chongli Yuan, "Double-Walled SnO<sub>2</sub> Nano-Cocoons with Movable Magnetic Cores" *Adv. Mater.* 0000, 00, 1–6.

[33] Dianping Tang, Ruo Yuan, "Magnetic Core-Shell Fe<sub>3</sub>O<sub>4</sub>@Ag Nanoparticles Coated Carbon Paste Interface for Studies of Carcinoembryonic Antigen in Clinical Immunoassay" *J. Phys. Chem. B*, 110 (24),



11640–11646 (2006).

[34] Jennifer L. Lyon, David A. Fleming, "Synthesis of Fe Oxide Core/Au Shell Nanoparticles by Iterative Hydroxylamine Seeding" *Nano Lett.*, 4 (4), 719–723 (2004).

[35] Hong-Mei Xiao, Xian-Ming Liu, "Synthesis, magnetic and microwave absorbing properties of core-shell structured  $\text{MnFe}_2\text{O}_4/\text{TiO}_2$  nanocomposites" *Composites Science and Technology* 66 2003–2008 (2006).

[36] Mohammad Reza Ganjali, Morteza Hosseini, "A novel europium-sensitive fluorescent nano-chemosensor based on new functionalized magnetic core-shell  $\text{Fe}_3\text{O}_4@\text{SiO}_2$  nanoparticles" *Talanta* 115, 271-276 (2013).

[37] Xiaohong Peng, Yujiao Wang, "Functionalized magnetic core-shell  $\text{Fe}_3\text{O}_4@\text{SiO}_2$  nanoparticles as selectivity-enhanced chemosensor for Hg(II)" *Dyes and Pigments* 91, 26-32 (2011).

[38] Uğur Tamer, Yusuf Gündoğdu, "Synthesis of magnetic core-shell  $\text{Fe}_3\text{O}_4$ -Au nanoparticle for biomolecule immobilization and detection" *Journal of Nanoparticle Research* 12, 4, 1187-119 (2010).

[39] Zhen Fan, Melanie Shelton, "Multifunctional Plasmonic Shell-Magnetic Core Nanoparticles for Targeted Diagnostics, Isolation, and Photothermal Destruction of Tumor Cells" *ACS Nano*, 6(2), 1065–1073 (2012).

[40] H He, C Gao, "Supraparamagnetic, Conductive, and Processable Multifunctional Graphene Nanosheets Coated with High-Density  $\text{Fe}_3\text{O}_4$  Nanoparticles" *ACS Appl. Mater. Interfaces* 2(11), 3201–3210 (2010).

[41] ZS Wu, S Yang, Y Sun, K Parvez, X Feng . 3D Nitrogen-Doped Graphene Aerogel-Supported  $\text{Fe}_3\text{O}_4$  Nanoparticles as Efficient Electrocatalysts for the Oxygen Reduction Reaction, *J. Am. Chem. Soc.*, 134 (22), 9082–9085 (2012).

[42] Lee, Y., Garcia, M., Frey Huls, Natalie A. and Sun, S., "Synthetic Tuning of the Catalytic Properties of Au- $\text{Fe}_3\text{O}_4$  Nanoparticles" *Angew. Chem.*, 122, 1293–1296 (2010).

[43] C Xu, B Wang, S Sun. "Dumbbell-like Au- $\text{Fe}_3\text{O}_4$  Nanoparticles for Target-Specific Platin Delivery" *J. Am. Chem. Soc.*, 131 (12), 4216–4217 (2009).

[44] Chih-Cheh Lo, Chun-Chao Huang, "Magnetic properties of electroless-deposited Ni and Ni-NiO core-shell nano-arrays" *Journal of Magnetism and Magnetic Materials* 323 1950–1953 (2011).

[45] Jun-Min Yan, Xin-Bo Zhang, "One-Step Seeding Growth of Magnetically Recyclable Au@Co Core-Shell Nanoparticles: Highly Efficient Catalyst for Hydrolytic Dehydrogenation of Ammonia Borane" *J. Am. Chem. Soc.*, 132 (15), 5326–5327 (2010).

[46] Zhichuan Xu, Yanglong Hou, and Shouheng Sun, "Magnetic Core/Shell  $\text{Fe}_3\text{O}_4/\text{Au}$  and  $\text{Fe}_3\text{O}_4/\text{Au}/\text{Ag}$  Nanoparticles with Tunable" *J. AM. CHEM. SOC.* 129, 8698-8699 (2007).

[47] Hye-Young Park, Mark J. Schadt, "Fabrication of Magnetic Core@Shell Fe Oxide@Au Nanoparticles for Interfacial Bioactivity and Bio-separation" *Langmuir*, 23, 9050-9056 (2007).

[48] U Tamer, Y Gündoğdu, İH Boyacı, K Pekmez, "Synthesis of magnetic core-shell  $\text{Fe}_3\text{O}_4$ -Au nanoparticle for biomolecule immobilization and detection" *Journal of Nanoparticle Research*, 12, 4, 1187-1196 (2010).

[49] Bumajdad, A., Ali, S., Mathew A., "Characterization of iron hydroxide/oxide nanoparticles prepared in microemulsions stabilized with cationic/non-ionic surfactant mixtures" *J. Colloid Interface Sci.*, 355, 282-292 (2011).

- [50] José S Garitaonandia, Maite Insausti, Eider Goikolea et al. "Chemically induced permanent magnetism in Au, Ag, and Cu nanoparticles: localization of the magnetism by element selective techniques" *Nano Letters*, 8 (2), 661-667 (2008).
- [51] M Mahmoudi, S Sant, B Wang, S Laurent, "Superparamagnetic iron oxide nanoparticles (SPIONs): Development, surface modification and applications in chemotherapy" *Advanced Drug Delivery Reviews* 63, 24-46 (2011).
- [52] A Bumb, MW Brechbiel, PL Choyke, L Fugger, "Synthesis and characterization of ultra-small superparamagnetic iron oxide nanoparticles thinly coated with silica" *Nanotechnology* 19, 335601 (6pp) (2008).
- [53] PA Liberti, CG Rao, LWMM Terstappen, "Optimization of ferrofluids and protocols for the enrichment of breast tumor cells in blood" *Journal of Magnetism and Magnetic Materials* 225, 301-307 (2001).
- [54] Ying Jing, Lee R. Moore, P. Stephen Williams, "Blood Progenitor Cell Separation From Clinical Leukapheresis Product by Magnetic Nanoparticle Binding and Magnetophoresis" *Biotechnol. Bioeng.* 96: 1139-1154 (2007).
- [55] GF Goya, V Grazu, MR Ibarra, *Magnetic Nanoparticles for Cancer Therapy*, *Current Nanoscience*, 4(1), 1-16(16) (2008).
- [56] QA Pankhurst, NTK Thanh, SK Jones, "Progress in applications of magnetic nanoparticles in biomedicine" *J. Phys. D: Appl. Phys.* 42, 224001 (15pp) (2009).
- [57] DE Owens III, NA Peppas, "Opsonization, biodistribution, and pharmacokinetics of polymeric nanoparticles" *International Journal of Pharmaceutics* 307, 93-102 (2006).
- [58] Laurent, S., Forge, D., Port, M., Roch, A., Robic, C., Vander Elst, L., Muller, RN. "Magnetic Iron Oxide Nanoparticles: Synthesis, Stabilization, Vectorization, Physicochemical Characterizations, and Biological Applications" *Chemical Reviews*, 108(6), 2064-2110 (2007).
- [59] BB Pultrum, EJ Van der Jagt, HL Van Westreenen, "Detection of lymph node metastases with ultrasmall superparamagnetic iron oxide (USPIO)-enhanced magnetic resonance imaging in oesophageal cancer: a feasibility study" *Cancer Imaging*. 9(1), 19-28 (2009).
- [60] CW Lai, YH Wang, CH Lai, MJ Yang, CY Chen, "Iridium-Complex-Functionalized Fe<sub>3</sub>O<sub>4</sub>/SiO<sub>2</sub> Core/Shell Nanoparticles: A Facile Three-in-One System in Magnetic Resonance Imaging, Luminescence Imaging, and Photodynamic Therapy" *small* 4(2), 218 - 224 (2008).
- [61] J Yang, SB Park, HG Yoon, YM Huh, S Haam, "Preparation of poly ε-caprolactone nanoparticles containing magnetite for magnetic drug carrier" *International Journal of Pharmaceutics* 324, 185-190 (2006).
- [62] M Muthana, SD Scott, N Farrow, F Morrow, C Murdoch, "A novel magnetic approach to enhance the efficacy of cell-based gene therapies" *Gene Therapy* 15, 902-910 (2008).
- [63] Martin, Y., C. C. Williams, and H. Kumar Wickramasinghe. "Atomic force microscope-force mapping and profiling on a sub 100 Å scale." *Journal of Applied Physics* 61, (10), 4723-4729 (1987).
- [64] Hartmann, U., "Magnetic force microscopy" *Annual Review of Materials Science*, 29, 53- 87 (1999).
- [65] M. Roseman and P. Grütter, "Cryogenic magnetic force microscope" *Rev. Sci. Instrum.* 71, 3782 (2000).
- [66] M. Liebmann et al, "Domain nucleation and growth of La<sub>0.7</sub>Ca<sub>0.3</sub>MnO<sub>3-δ</sub>/LaAlO<sub>3</sub> films studied by low

- temperature magnetic force microscopy" *J. Appl. Phys.* 93, 8319 (2003).
- [67] H. J. Mamin, R. Budakian, B. W. Chui and D. Rugar, "Detection and Manipulation of Statistical Polarization in Small Spin Ensembles" *Phys. Rev. Lett.* 91, 207604 (2003).
- [68] M.D. Chabot and J. Moreland, "Micrometer-scale magnetometry of thin Ni<sub>80</sub>Fe<sub>20</sub> films using ultrasensitive microcantilevers" *J. Appl. Phys.* 93, 7897 (2003).
- [69] C. Lupien, B. Ellman, P. Grütter, and L. Taillefer, "Piezoresistive torque magnetometry below 1 K" *Appl. Phys. Lett.* 74, 451 (1999).
- [70] X. Zhu, P. Grütter, V. Metlushko, and B. Ilic, "Magnetization reversal and configurational anisotropy of dense permalloy dot arrays" *Appl. Phys. Lett.* 80, 4789 (2002).
- [71] C.A. Ross et al, "Fabrication of patterned media for high density magnetic storage" *J.Vac. Sci. Technol.*, B17, 3168 (1999).
- [72] R.P. Cowburn, "Property variation with shape in magnetic nanoelements" *J. Phys. D: Appl. Phys.* 33, R1 (2000).
- [73] S.A. Wolf et al, "Spintronics: A Spin-Based Electronics Vision for the Future" *Science* 294, 1488 (2001).
- [74] M.C.B. Parish and M. Forshaw, "Physical constraints on magnetic quantum cellular automata" *Appl. Phys. Lett.* 83, 2046 (2003).
- [75] Michael E. Frohbergh, Anna Katsman, Gregory P. Botta, Phillip Lazarovici, Caroline L. Schauer, Ulrike G.K. Wegst, Peter I. Lelkes, "Electrospun hydroxyapatite-containing chitosan nanofibers crosslinked with genipin for bone tissue engineering" *Biomaterials* 33(36), 9167–9178 (2012)
- [76] Marion L. Hodgdon, "Mathematical theory and calculations of magnetic hysteresis curves" *TRANSACTIONS ON MAGNETICS*, 24, 6, (1988).
- [77] Bruno Torre, Giovanni Bertoni et al., "Magnetic Force Microscopy and Energy Loss Imaging of Superparamagnetic Iron Oxide Nanoparticles" *Scientific Report* 1, Article number: 202.
- [78] DL Atherton, JR Beattie, "A mean field Stoner-Wohlfarth hysteresis model" *TRANSACTIONS ON MAGNETICS*, 26, 6, (1990).
- [79] W Luo, SR Nagel, TF Rosenbaum, "Dipole interactions with random anisotropy in a frozen ferrofluid" *Phys. Rev. Lett.* 67, 2721–2724 (1991).
- [80] Geraldo Antônio Guerrera Cidade, Gilberto Weissmüller and Paulo Mascarello Bisch. "A microcontroller-based system for piezoscaner nonlinearity correction: Atomic force microscope" *Rev. Sci. Instrum.* 69, 3593 (1998).
- [81] Szuchi Tien, Qingze Zou, Devasia, S., "Iterative control of dynamics-coupling-caused errors in piezoscaners during high-speed AFM operation" *Control Systems Technology, IEEE Transactions on* 6 (13), 921-931 (2005).
- [82] I V Yaminsky, A M. Tishin, "Magnetic force microscopy" *Russian Chemical Reviews* 68 (3) 165-170 (1999).
- [83] G N Philips, T Suzuki, "Quantitative analysis of written bit transitions in 5 Gbit/in<sup>2</sup> media by magnetic force microscopy" *J. Magn. Mater.* 175 115 (1997).
- [84] Juergen Heidmann and Dieter Weller, "Quantitative magneto-optic field imaging of recording heads

(abstract)" J. Appl. Phys. 81, 4522 (1997).

[85] T Homma, Y Kurokawa, T Nakamura, T Osaka, I Otsuka, "Magnetic force microscopy analysis of the micromagnetization mode of double layered perpendicular magnetic recording media" J. Vac. Sci. Technol., B 14 1184 (1996).

[86] R B Proksch et al, "Magnetic force microscopy of the submicron magnetic assembly in a magnetotactic bacterium" Appl. Phys. Lett. 66 2582 (1995).

[87] Pacifico J et al, "Field gradient imaging of nanoparticle systems: analysis of geometry and surface coating effects" Nanotechnology. 2009 Mar 4;20(9):095708.

[88] Sharon Schreiber et al, "Magnetic Force Microscopy of Superparamagnetic Nanoparticles" Small 4(2), 270–278 (2008).

[89] A. A. Bukharaev et al, "Investigation of micromagnetism and magnetic reversal of Ni nanoparticles using a magnetic force microscope, Physics of the Solid State, 40(7), 1163-1168 (1998).

[90] Patel, Rajen; Owens, Frank J, "Ferromagnetic resonance and magnetic force microscopy evidence for above room temperature ferromagnetism in Mn doped Si made by a solid state sintering process" Solid State Communications, 152(7), 603-605 (2012).

[91] Y. J. Chen et al, "Magnetic domain structures of  $\text{Co}_{22}\text{Ag}_{78}$  granular films observed by magnetic force microscopy" Appl. Phys. Lett. 72, 2472 (1998).

[92] Zhang, Jingjing et al., "Magnetic force microscopy study of heat-treated  $\text{Fe}_{81}\text{Ga}_{19}$  with different cooling rates" Physica B: Physics of Condensed Matter, Volume 405, Issue 15, p. 3129-3134.

[93] Ghidini, M. et al, "Growth rate dependence of the extrinsic magnetic properties of electrodeposited CoPt films" Journal of Magnetism and Magnetic Materials, 322, 9-12, 1576-1580 (2010).

[94] Fang, Yi-Kun et al, "Magnetic microstructures of a high coercivity Nd–Fe–B sintered magnet in remanent and incomplete thermal demagnetization states" Journal of Magnetism and Magnetic Materials, 322(22), 3720-3723 (2010).

[95] Jalli, Jeevan et al, "MFM studies of magnetic domain patterns in bulk barium ferrite ( $\text{BaFe}_{12}\text{O}_{19}$ ) single crystals" Journal of Magnetism and Magnetic Materials, 323(21), 2627-2631 (2011).

[96] Szmaja, W. et al, "Study of the morphological and magnetic structures of nanocrystalline cobalt films obtained by electrodeposition" Materials Chemistry and Physics, 132, 2-3, 1060-1064 (2012).

[97] Zhang, W. Y. et al, "Origin of perpendicular magnetic anisotropy and evolution of magnetic domain structure of amorphous Pr–TM–B (TM=Fe, Co) films" Journal of Magnetism and Magnetic Materials, 322, 8, 900-908 (2010).

[98] Anett Diestel et al, "Magnetic domain structure of epitaxial Ni–Mn–Ga films" Scripta Materialia 67 423–426 (2012).

[99] F.A. Ferri et al, "The composition, structure and optical properties of weakly magnetic Co-containing amorphous Si and Ge films" Materials Chemistry and Physics, 134, 153– 157 (2012).

[100] Mudivarthi, Chaitanya et al, "Magnetic domain observations in Fe–Ga alloys" J. Magn. Magn. Mat. 322, 14, 2023-2026 (2010).

[101] Witold Szmaja et al, "Magnetic force microscopy investigation of the domain structure of nanocomposite  $\text{Nd}_2\text{Fe}_{14}\text{B}/\text{Fe}_3\text{B}$  magnets" Acta Materialia 59, 531–536 (2011).

- [102] García Ignacio et al, "Magnetic force microscopy characterization of heat and current treated Fe<sub>40</sub>Ni<sub>38</sub>Mo<sub>4</sub>B<sub>18</sub> amorphous ribbons" *J. Magn. Magn. Mat.* 322(13), 1822-1827 (2010).
- [103] Park, J.W., Yoo, I.S., Chang, W.S., Lee, E.C., Ju, H., Chung, B.H. & Kim, B.S., "Magnetic moment measurement of magnetic nanoparticles using atomic force microscopy" *Measurement Science and Technology*, 19(1), 017005 (2008).
- [104] Dobson, J., "Nanoscale biogenic iron oxides and neurodegenerative disease" *FEBS Letters*, 496(1), 1–5 (2001).
- [105] Diebel, C.E., Proksch, R., Green, C.R., Neilson, P. & Walker, M.M., "Magnetite defines a vertebrate magnetoreceptor" *Nature*, 406, 299–302 (2000).
- [106] Rasa, M., Kuipers, B.W.M. & Philipse A.P., "Atomic force microscopy and magnetic force microscopy study of model colloids" *Journal of Colloid and Interface Science*, 250(2), 303–315 (2002).
- [107] Bryan R. Smith, Johannes Heverhagen et al., "Localization to atherosclerotic plaque and biodistribution of biochemically derivatized superparamagnetic iron oxide nanoparticles (SPIONs) contrast particles for magnetic resonance imaging (MRI)" *Biomedical Microdevices*, 9(5), 719-727 (2007).
- [108] Zhang, Y., Yang, M., Ozkan, M. and Ozkan, C. S., "Magnetic force microscopy of iron oxide nanoparticles and their cellular uptake" *Biotechnol Progress*, 25: 923–928 (2009).
- [109] Dias, A.; Andrade, M.S. et al., "Atomic force and magnetic force microscopies applied to duplex stainless steels" *Applied Surface Science*, 161, 1-2, 109-114 (2000).
- [110] F. Wolny et al, "Magnetic force microscopy measurements in external magnetic fields—comparison between coated probes and an iron filled carbon nanotube probe" *J. Appl. Phys.* 108, 013908 (2010).
- [111] Cambel, V. et al, "Magnetic elements for switching magnetization magnetic force microscopy tips" *Journal of Magnetism and Magnetic Materials*, 322(18), 2715-2721 (2010).
- [112] Gong, J. & Wei, D., "Comparison of micromagnetic and probe model in magnetic force microscope simulation" *IEEE Transactions on Magnetism*, 43(10) 3821–3825 (2007).
- [113] Hans J. Hug et al, "Quantitative magnetic force microscopy on perpendicularly magnetized samples" *J. Appl. Phys.* 83, 5609 (1998).
- [114] Victor L. Mironov et al, "Magnetic Force Microscope Contrast Simulation for Low-Coercive Ferromagnetic and Superparamagnetic Nanoparticles in an External Magnetic Field" *IEEE TRANSACTIONS ON MAGNETICS*, 43(11), (2007).
- [115] G. Ozaydin-Ince, A. M. Coclite, K. K. Gleason, "CVD of polymeric thin films: applications in sensors, biotechnology, microelectronics/organic electronics, microfluidics, MEMS, composites and membranes" *Reports on Progress in Physics* 75016501 (2012).
- [116] I. Tokarev, S. Minko, "Stimuli-responsive hydrogel thin films", *Soft Matter* 5 511–524 (2009).
- [117] O. K. C. Tsui, T. P. Russell, "Polymer Thin Films" World Scientific, 2008.
- [118] V. K. Vendra, L. Wu, S. Krishnan, "Polymer Thin Films for Biomedical Applications" *Nanomaterials for the Life Sciences*, vol.5, Wiley-VCH Verlag GmbH & Co. KGaA 1–54 (2010).
- [119] B. Adhikari, S. Majumdar, "Polymers in sensor applications" *Progress in Polymer Science* 29, 699–766 (2004).
- [120] H. Bai, G. Shi, "Gas sensors based on conducting polymers" *Sensors* 7, 267–307 (2007).

- [121] P. Herrasti, P. Ocón, A. Ibáñez, E. Fatás, "Electroactive polymer films for stainless steel corrosion protection" *Journal of Applied Electrochemistry* 33, 533–540 (2003).
- [122] M.L. Chabinyk, Y. L. Loo, "Semiconducting polymers for thin-film electronics" *Journal of Macromolecular Science Polymer Reviews*, 46, 1–5 (2006).
- [123] A. N. Zelikin, "Drug releasing polymer thin films: new era of surface-mediated drug delivery" *ACS Nano* 4(2010)2494–2509.
- [124] J.W. Costerton, P.S. Stewart, E. P. Greenberg, "Bacterial biofilms: a common cause of persistent infections" *Science* 284, 1318–1322 (1999).
- [125] C. Nicolella, M. C. M. van Loosdrecht, J. J. Heijnen, "Waste water treatment with particulate biofilm reactors" *Journal of Biotechnology* 80, 1–33 (2000).
- [126] R. Singh, D. Paul, R. K. Jain, "Biofilms: implication in bioremediation" *Trends in Microbiology*, 14, 389–397 (2006).
- [127] B. Halan, K. Buehler, A. Schmid, "Biofilms as living catalysts in continuous chemical syntheses" *Trends in Biotechnology*, 30, 453–465 (2012).
- [128] D. , M. Rossi, E. Tamburri, M. L. Terranova, "Mechanical characterization of polymeric thin films by atomic force microscopy based techniques" *Analytical and Bioanalytical Chemistry*, 405, 1463–1478 (2013).
- [129] L. Reséndiz, M. Estrada, A. Cerdeira, B. Iniguez, M. J. Deen, "Effect of active layer thickness on the electrical characteristics of polymer thin film transistors" *Organic Electronics*, 11, 1920–1927 (2010).
- [130] P. S. Stewart, "Diffusion in biofilms" *Journal of Bacteriology*, 185, 1485–1491 (2003).
- [131] P. A. Flournoy, R. W. McClure, G. Wyntjes, "White-light interferometric thickness gauge" *Applied Optics*, 11, 1907–1915 (1972).
- [132] S. W. Kim, G. H. Kim, "Thickness-profile measurement of transparent thin-film layers by white-light scanning interferometry" *Applied Optics*, 38, 5968–5973 (1999).
- [133] H.G. Tompkins, T. Tiwald, C. Bungay, A. E. Hooper, "Measuring the thickness of organic/polymer/biological films on glass substrates using spectroscopic ellipsometry" *Journal of Vacuum Science & Technology*, A24, 1605–1609 (2006).
- [134] W. J. Okkerse, S. P. Ottengraf, B. Osinga-Kuipers, "Biofilm thickness variability investigated with a laser triangulation sensor" *Biotechnology and Bioengineering*, 70, 619–629 (2000).
- [135] W. F. C. Kools, S. Konagurthu, A. R. Greenberg, L. J. Bond, W. B. Krantz, T. Vanden Boomgaard, H. Strathmann, "Use of ultrasonic time-domain reflectometry for real-time measurement of thickness changes during evaporative casting of polymeric films" *Journal of Applied Polymer Science* 69, 2013–2019 (1998).
- [136] A. O. Kivioja, A. S. Jä. skelänen, V. Ahtee, T. Vuorinen, "Thickness measurement of thin polymer films by total internal reflection Raman and attenuated total reflection infrared spectroscopy" *Vibrational Spectroscopy*, 61, 1–9 (2012).
- [137] T. R. Tuladhar, W. R. Paterson, N. Macleod, D. I. Wilson, "Development of a novel non-contact proximity gauge for thickness measurement of soft deposits and its application in fouling studies" *Canadian Journal of Chemical Engineering*, 78, 935–947 (2000).
- [138] J. Y. Kim, Y. S. Choi, Y. J. Park, K. Song, S. H. Jung, E. M. A. Hussein, "Thickness measurement of organic films using Compton scattering of characteristic X-rays" *Applied Radiation and Isotopes*, 69,

1241–1245 (2011).

[139] A. Hassanzadeh, S. Armstrong, S. J. Dixon, S. Mittler, "Multimode wave guide evanescent field fluorescence microscopy: measurement of cell-substratum separation distance" *Applied Physics Letters* 94, 033503 (2009).

[140] M. Campione, M. Cartotti, E. Pinotti, A. Sassella, A. Borghesi, "Thickness measurements by quartz microbalance during thin-film growth by organic molecular-beam deposition" *Journal of Vacuum Science & Technology A* 22, 482–486 (2004).

[141] E. Paramonova, E. D. deJong, B. P. Krom, H. C. vanderMei, H. J. Busscher, P. K. Sharma, "Low-load compression testing: a novel way of measuring biofilm thickness" *Applied and Environmental Microbiology*, 73, 7023–7028 (2007).

[142] V. Körstgens, H. C. Flemming, J. Wingender, W. Borchard, "Uniaxial compression measurement device for investigation of the mechanical stability of biofilms" *Journal of Microbiological Methods*, 46, 9–17 (2001).

[143] R. F. M. Lobo, M. A. Pereira-da-Silva, M. Raposo, R. M. Faria, O. N. Oliveira Jr., "In situ thickness measurements of ultra-thin multilayer polymer films by atomic force microscopy" *Nanotechnology* 10, 389–393 (1999).

[144] T. A. Mykhaylyk, N. L. Dmitruk, S. D. Evans, I.W.Hamley, J. R. Henderson, "Comparative characterization by atomic force microscopy and ellipsometry of soft and solid thin films" *Surface and Interface Analysis*, 39, 575–581 (2007).

[145] P. G. Hartley, H. Thissen, T. Vaithianathan, H. J. Griesser, "A surface masking technique for the determination of plasma polymer film thickness by AFM" *Plasmas and Polymers* 5, 47–60 (2000).

[146] X. Hong, Y. Gan, Y. Wang, "Facile measurement of polymer film thickness ranging from nanometer to micrometer scale using atomic force microscopy" *Surface and Interface Analysis* 43, 1299–1303 (2011).

[147] G. Legay, L. Markey, R. Meunier-Prest, E. Finot, "Measurements of thickness dispersion in bilayers by scanning force microscopy and comparison with spectroscopic ellipsometry analysis" *Ultramicroscopy*, 107, 1111–1117 (2007).

[148] I. Caruso, L. Fumagalli, G. Gomila, E. Pedrós, "Non destructive thickness measurement of biological layers at the nanoscale by simultaneous topography and capacitance imaging" *Applied Physics Letters* 91, 063111 (2007).

[149] D. W. Abraham, C. C. Williams, H. K. Wickramasinghe, "Measurement of in-plane magnetization by force microscopy" *Applied Physics Letters* 53, 1446–1448 (1988).

[150] D. Rugar, H. J. Mamin, P. Guethner, S. E. Lambert, J. E. Stern, I. Mc Fadyen, T. Yogi, "Magnetic force microscopy: general principles and application to longitudinal recording media" *Journal of Applied Physics* 68, 1169–1183 (1990).

[151] F.Krause, F.Kaisinger, H.Starke, G.Persch, U.Hartmann, "The influence of experimental parameters on contrast formation in magnetic force microscopy" *Thin Solid Films*, 264, 141–147 (1995).

[152] K. Ishikawa, R. Taguchi, E. Miyashita, J. Numazawa, H. Ohshima, "Magnetic force microscopy image of Co–Cr–Ta layer in perpendicular magnetic tape at high linear recording density" *Journal of Applied Physics*, 81, 4390–4392 (1997).

- [153] S. Porthun, L. Abelmann, C. Lodder, "Magnetic force microscopy applied in magnetic data storage technology" *Journal of Magnetism and Magnetic Materials*, 182, 238–273 (1998).
- [154] K. Aso, T. Sato, M. Ishibashi, "Magnetic force microscopic study of magnetic tapes recorded at MHz frequencies" *Journal of Magnetism and Magnetic Materials*, 193, 430–433 (1999).
- [155] U. Hartmann, "Magnetic force microscopy" *Annual Review of Materials Science*. 29, 53–87 (1999).
- [156] M. Savla, R. P. Pandian, P. Kuppusamy, G. Agarwal, Magnetic force microscopy of an oxygen-sensing spin-probe, *Israel Journal of Chemistry* 48(2008)33–38.
- [157] V.L. Mironov, D. S. Nikitushkin, C. Bins, A. B. Shubin, P. A. Zhdan, "Magnetic force microscope contrast simulation for low-coercive ferromagnetic and superparamagnetic nanoparticles in an external magnetic field" *IEEE Transactions on Magnetics* 43, 3961–3963 (2007).
- [158] V.L. Mironov, D. S. Nikitushkin, D. S. Petrov, A. B. Shubin, P.A.Zhdan, "Simulation of the mfm contrast from small low-coercive ferromagnetic nanoparticles in an external field" *Journal of Surface Investigation X-ray Synchrotron and Neutron Techniques*, 1, 348–351 (2007).
- [159] C. Dietz, E. T. Herruzo, J. R. Lozano, R. Garcia, "Nanomechanical coupling enables detection and imaging of 5nm superparamagnetic particles in liquid" *Nanotechnology* 22, 125708 (2011).
- [160] I.G. Hughes, P. A. Barton, T. M. Roach, E. A. Hinds, "Atom optics with magnetic surfaces. II. Microscopic analysis of the 'floppy disk' mirror" *Journal of Physics B: Atomic, Molecular and Optical Physics*, 30, 2119–2132 (1997).
- [161] F. Pantanella, F. Berlutti, D. , D. Sordi, A. Frioni, T. Natalizi, M.L. Terranova, M. Rossi, P. Valenti, "Quantitative evaluation of bacteria adherent and in biofilm on single wall carbon nano-tube coated surface" *Interdisciplinary Perspectives on Infectious Diseases*, 29, 1513 (2011).
- [162] C.S. Neves, P. Quaresma, P. V. Baptista, P. A. Carvalho, J. P. Araújo, E. Pereira, P. Eaton, New insights into the use of magnetic force microscopy to discriminate between magnetic and nonmagnetic nanoparticles, *Nanotechnology*, 21, 305706 (2010).
- [163] R. Giles, J. P. Cleveland, S. Manne, P. K. Hansma, B. Drake, P. Maivalds, C. Boles, J. Gurley, V. Elings, "Noncontact force microscopy in liquids" *Applied Physics Letters* 63, 617–618 (1993).
- [164] M. A. Lantz, S. J. O'Shea, M. E. Welland, "Force microscopy imaging in liquids using ac techniques" *Applied Physics Letters* 65, 409–411 (1994).
- [165] J. Vergara, V. Madurga, P. Eames, E. DanDahlberg, "Magnetic force microscopy observations of co nanoparticles grown on annealing Co<sub>10</sub>Cu<sub>90</sub> melt spun ribbons" *Journal of Applied Physics* 99, 053910 (2006).
- [166] S. Schreiber, M. Savla, D. V. Pelekhov, D.F. Iscru, C. Selcu, P. C. Hammel, G. Agarwal, "Magnetic force microscopy of superparamagnetic nanoparticles" *Small* 4, 270–278 (2008).
- [167] T. M. Nocera, J. Chen, C. B. Murray, G. Agarwal, "Magnetic anisotropy considerations in magnetic force microscopy studies of single superparamagnetic nanoparticles" *Nanotechnology* 23, 495704 (2012).
- [168] S. Sievers, K. F. Braun, D. Eberbeck, S. Gustafsson, E. Olsson, H. W. Schumacher, U. Siegner, "Quantitative measurement of the magnetic moment of individual magnetic nanoparticles by magnetic force microscopy" *Small* 8, 2675–2679 (2012).
- [169] I. S. Gradshteyn, I. M. Ryzhik, "Tables of Integrals, Series and Products" Academic Press, (1980).



- [170] Peer, Dan, Jeffrey M. Karp, Seungpyo Hong, Omid C. Farokhzad, Rimona Margalit, and Robert Langer. "Nanocarriers as an emerging platform for cancer therapy" *Nature nanotechnology* 2, 12: 751-760 (2007).
- [171] Kim, Jaeyun, Yuanzhe Piao, and Taeghwan Hyeon, "Multifunctional nanostructured materials for multimodal imaging, and simultaneous imaging and therapy" *Chemical Society Reviews* 38, 2: 372-390 (2009).
- [172] Reddy, L. Harivardhan, José L. Arias, Julien Nicolas, and Patrick Couvreur, "Magnetic nanoparticles: design and characterization, toxicity and biocompatibility, pharmaceutical and biomedical applications" *Chemical reviews* 112, 11: 5818-5878 (2012).
- [173] Anand, Preetha, Ajaikumar B. Kunnumakkara, Robert A. Newman, and Bharat B. Aggarwal. "Bioavailability of curcumin: problems and promises" *Molecular pharmaceutics* 4, 6: 807-818 (2007).
- [174] Gregoriadis, Gregory, and Brenda E. Ryman, "Lysosomal localization of beta-fructofuranosidase-containing liposomes injected into rats. Some implications in the treatment of genetic disorders" *Biochem. J* 129: 123-133 (1972).
- [175] Alsarra, Ibrahim A., Ahmed A. Bosela, Sayed M. Ahmed, and G. M. Mahrous, "Proniosomes as a drug carrier for transdermal delivery of ketorolac" *European journal of pharmaceutics and biopharmaceutics* 59, 3: 485-490 (2005).
- [176] Pardakhty Abbas, Jaleh Varshosaz, and Abdolhossein Rouholamini, "In vitro study of polyoxyethylene alkyl ether niosomes for delivery of insulin" *International journal of pharmaceutics* 328, 2: 130-141 (2007).
- [177] Šentjerc, M., K. Vrhovnik, and J. Kristl, "Liposomes as a topical delivery system: the role of size on transport studied by the EPR imaging method" *Journal of controlled release* 59, 1: 87-97 (1999).
- [178] Choi, M. J., and H. I. Maibach, "Liposomes and niosomes as topical drug delivery systems" *Skin pharmacology and physiology* 18, 5: 209-219 (2005).
- [179] Lu, Jian, Shuli Ma, Jiayu Sun, Chunchao Xia, Chen Liu, Zhiyong Wang, Xuna Zhao et al., "Manganese ferrite nanoparticle micellar nanocomposites as MRI contrast agent for liver imaging" *Biomaterials* 30, 15: 2919-2928 (2009).
- [180] Ai Hua, "Layer-by-layer capsules for magnetic resonance imaging and drug delivery" *Advanced drug delivery reviews* 63, 9: 772-788 (2011).
- [181] Lee, Ji Eun, Nohyun Lee, Hyoungsu Kim, Jaeyun Kim, Seung Hong Choi, Jeong Hyun Kim, Taeho Kim et al., "Uniform mesoporous dye-doped silica nanoparticles decorated with multiple magnetite nanocrystals for simultaneous enhanced magnetic resonance imaging, fluorescence imaging, and drug delivery" *Journal of the American Chemical Society* 132, 2: 552-557 (2009).
- [182] Berret Jean-François, Nicolas Schonbeck, Florence Gazeau, Delphine El Kharrat, Olivier Sandre, Annie Vacher, and Marc Airiau, "Controlled clustering of superparamagnetic nanoparticles using block copolymers: design of new contrast agents for magnetic resonance imaging" *Journal of the American Chemical Society* 128, 5: 1755-1761 (2006).
- [183] Jun, Young-wook, Yong-Min Huh, Jin-sil Choi, Jae-Hyun Lee, Ho-Taek Song, Sungjun Kim, Sungjun Kim et al. "Nanoscale size effect of magnetic nanocrystals and their utilization for cancer diagnosis via magnetic resonance imaging." *Journal of the American Chemical Society* 127, 16: 5732-5733 (2005).

- [184] Xie, Jin, Gang Liu, Henry S. Eden, Hua Ai, and Xiaoyuan Chen, "Surface-engineered magnetic nanoparticle platforms for cancer imaging and therapy" *Accounts of chemical research* 44, 10: 883-892 (2011).
- [185] Zeng, Q., I. Baker, J. A. Loudis, Y. Liao, P. J. Hoopes, and J. B. Weaver. "Fe/Fe oxide nanocomposite particles with large specific absorption rate for hyperthermia." *Applied physics letters* 90, 23: 233112, (2007).
- [186] Mornet, Stéphane, Sébastien Vasseur, Fabien Grasset, and Etienne Duguet. "Magnetic nanoparticle design for medical diagnosis and therapy." *Journal of Materials Chemistry* 14, 14: 2161-2175 (2004).
- [187] Uchida, Masaki, Michelle L. Flenniken, Mark Allen, Deborah A. Willits, Bridgid E. Crowley, Susan Brumfield, Ann F. Willis et al., "Targeting of cancer cells with ferrimagnetic ferritin cage nanoparticles." *Journal of the American Chemical Society* 128, 51: 16626-16633 (2006).
- [188] Sun, Conroy, Jerry SH Lee, and Miqin Zhang, "Magnetic nanoparticles in MR imaging and drug delivery" *Advanced drug delivery reviews* 60, 11: 1252-1265 (2008).
- [189] Chen, Shu, Ying Li, Chen Guo, Jing Wang, Junhe Ma, Xiangfeng Liang, Liang-Rong Yang, and Hui-Zhou Liu, "Temperature-responsive magnetite/PEO-PPO-PEO block copolymer nanoparticles for controlled drug targeting delivery" *Langmuir* 23, 25: 12669-12676 (2007).
- [190] Xu Zhenhe, Chunxia Li, Xiaojiao Kang, Dongmei Yang, Piaoping Yang, Zhiyao Hou, and Jun Lin, "Synthesis of a multifunctional nanocomposite with magnetic, mesoporous, and near-IR absorption properties" *The Journal of Physical Chemistry C* 114, 39: 16343-16350 (2010).
- [191] Namdeo, Mini, Sutanjay Saxena, Rasika Tankhiwale, M. Bajpai, Y. M. Mohan, and S. K. Bajpai. "Magnetic nanoparticles for drug delivery applications" *Journal of Nanoscience and Nanotechnology* 8, 7: 3247-3271 (2008).
- [192] Freiberg, S., and X. X. Zhu, "Polymer microspheres for controlled drug release" *International Journal of Pharmaceutics* 282, 1: 1-18 (2004).
- [193] M Gaumet, A Vargas, R Gurny, F Delie, "Nanoparticles for drug delivery: The need for precision in reporting particle size parameters" *European Journal of Pharmaceutics and Biopharmaceutics* 69, 1–9 (2008).
- [194] Xinglu Huang, Linlin Li, Tianlong Liu, Nanjing Hao, Huiyu Liu, Dong Chen, and Fangqiong Tang, "The Shape Effect of Mesoporous Silica Nanoparticles on Biodistribution, Clearance, and Biocompatibility in Vivo" *ACS Nano*, 5 (7), 5390–5399 (2011).
- [195] Ayrault, S., C. Loos-Neskovic, M. Fedoroff, E. Garnier, and D. J. Jones, "Compositions and structures of copper hexacyanoferrates (II) and (III): experimental results" *Talanta* 42, 11: 1581-1593 (1995).
- [196] Lacor, Pascale N., Dennis R. Grayson, James Auta, Ikuko Sugaya, Erminio Costa, and Alessandro Guidotti, "Reelin secretion from glutamatergic neurons in culture is independent from neurotransmitter regulation" *Proceedings of the National Academy of Sciences* 97, 7: 3556-3561 (2000).
- [197] Jiang, J., Gu, H., Shao, H., Devlin, E., Papaefthymiou, G. C. and Ying, J. Y., "Bifunctional Fe<sub>3</sub>O<sub>4</sub>-Ag Heterodimer Nanoparticles for Two-Photon Fluorescence Imaging and Magnetic Manipulation" *Adv. Mater.*, 20: 4403–4407 (2008).
- [198] Von White II G., Chen Y., Roder-Hanna J., Bothun, G. D., Kitchens C.L., "Structural and thermal analysis of lipid encapsulating hydrophobic gold nanoparticles" *ACS Nano*, 6, 4678–4685 (2012).

- [199] Jaskiewicz K., Larsen A., Schaeffel D., Koynov K., Lieberwirth I., Fytas G., Landfester K., Kroeger A., "Incorporation of nanoparticles into polymersomes: size and concentration effects" *ACS Nano*, 6, 7254–7262 (2012).
- [200] Khosravi-Darani K., Pardakhty A., Honarpisheh H., Rao V. S., Mozafari M. R. "The role of high-resolution imaging in the evaluation of nanosystems for bioactive encapsulation and targeted nanotherapy" *Micron*, 38, 804-818 (2007).
- [201] Ruozi B., Belletti D., Tombesi A., Tosi G., Bondioli L., Forni F., Vandelli M. A., "AFM, ESEM, TEM, and CLSM in liposomal characterization: a comparative study" *Int. J. Nanomedicine*, 6, 557–563 (2011).
- [202] Ruozi B., Tosi G., Leo E., Vandelli M. A., "Application of atomic force microscopy to characterize liposomes as drug and gene carriers" *Talanta*, 73, 12–22 (2007).
- [203] Reviakine I., Brisson A., "Formation of supported phospholipid bilayers from unilamellar vesicles investigated by atomic force microscopy" *Langmuir*, 16, 1806–1815 (2000).
- [204] Schönherr H., Rozkiewicz D. I., Vancso G. J., "Atomic force microscopy assisted immobilization of lipid vesicles" *Langmuir*, 20, 7308–7312 (2004).
- [205] Schönherr H., Johnson J. M., Lenz P., Frank C.W., Boxer S. G., "Vesicle adsorption and lipid bilayer formation on glass studied by atomic force microscopy" *Langmuir*, 20, 11600–11606 (2004).
- [206] Cortesi R., Esposito E., Corradini F., Sivieri E., Drechsler M., Rossi A., Scatturin A., Menegatti E., "Non-phospholipid vesicles as carriers for peptides and proteins: Production, characterization and stability studies" *Int. J. Pharmaceut.*, 339, 52–60 (2007).
- [207] Augustynska D., Jemioła-Rzeminska M., Burda K., Strzałka K., "Atomic force microscopy studies of the adhesive properties of DPPC vesicles containing  $\beta$ -carotene" *Acta Biochim. Pol.*, 59, 125–128 (2012).
- [208] Kanno T., Yamada T., Iwabuki H., Tanaka, H., Kuroda S., Tanizawa K., Kawai T., "Size distribution measurement of vesicles by atomic force microscopy" *Anal. Biochem.*, 309, 196–199 (2002).
- [209] Liang X., Mao G., Ng K. Y. S., "Probing small unilamellar EggPC vesicles on mica surface by atomic force microscopy" *Colloids Surf. B Biointerfaces*, 34, 41–51 (2004).
- [210] Jin A. J., Prasad K., Smith P. D., Lafer E. M., Nossal R., "Measuring the elasticity of clathrin-coated vesicles via atomic force microscopy" *Biophys. J.*, 90, 3333–3344 (2006).
- [211] Kumar S., Hoh J. H., "Direct visualization of vesicle-bilayer complexes by atomic force microscopy" *Langmuir*, 16, 9936–9940 (2000).
- [212] Jaskiewicz K., Makowski M., Kappl M., Landfester K., Kroeger A., "Mechanical properties of poly(dimethylsiloxane)-block-poly(2-methylloxazoline) polymersomes probed by atomic force microscopy" *Langmuir*, 28, 12629–12636 (2012).
- [213] Moskalenko A. V., Yarova P. L., Gordeev S. N., Smirnov S. V., "Single protein molecule mapping with magnetic atomic force microscopy" *Biophys. J.*, 98, 478–487 (2010).
- [214] Vallet C. E., White C. W., Withrow S. P., Budai J. D., Boatner L. A., Sorge K. D., Thompson J. R., Beaty K. S., Meldrum A., "Magnetic force microscopy of ferromagnetic nanoparticles formed in  $\text{Al}_2\text{O}_3$  and  $\text{SiO}_2$  by ion implantation" *J. Appl. Phys.*, 92, 6200–6204 (2002).
- [215] D. Passeri, C. Dong, L. Angeloni, F. Pantanella, T. Natalizi, F. Berlutti, C. Marianecchi, F. Ciccarello,

- M. Rossi, "Thickness measurement of soft thin films on periodically patterned magnetic substrates by phase difference magnetic force microscopy" *Ultramicroscopy* 136, 96–106 (2014).
- [216] Lu, S., Cheng, G. and Pang, X., "Preparation of molecularly imprinted Fe<sub>3</sub>O<sub>4</sub>/P(St-DVB) composite beads with magnetic susceptibility and their characteristics of molecular recognition for amino acid" *J. Appl. Polym. Sci.*, 89: 3790–3796 (2003).
- [217] Pedro Tartaj, María del Puerto Morales, Sabino Veintemillas-Verdaguer, Teresita González-Carreño and Carlos J Serna, "The preparation of magnetic nanoparticles for applications in biomedicine" *J. Phys. D: Appl. Phys.* 36 R182 (2003).
- [218] LANDFESTER K., RAMIREZ L.P., "Encapsulated magnetite particles for biomedical application" *J. Phys. Condens. Mat.*, 15, S1345–S1361 (2003).
- [219] E. Ruiz-Hernández, A. López-Noriega, D. Arcos, and M. Vallet-Regí, "Mesoporous magnetic microspheres for drug targeting" *Solid State Sciences*, vol. 10, no. 4, pp. 421–426 (2008).
- [220] Xie J, Chen K, Huang J, Lee S, Wang J, Gao J. et al. "PET/NIRF/MRI triple functional iron oxide nanoparticles" *Biomaterials*. 31:3016–22 (2010).
- [221] Natarajan, "Growth and Electrophysiological Properties of Rat Embryonic Cardiomyocytes on Hydroxyl- and Carboxyl-Modified Surfaces" *J Biomater Sci Polym Ed* (2010).
- [222] Taton T. A., Mirkin C. A., Letsinger R. L., "Scanometric DNA Array Detection with Nanoparticle Probes" *Science*, 289, 1757 (2000).
- [223] Ya-Na Wu, Li-Xing Yang, Xuan-Yu Shi, The selective growth inhibition of oral cancer by iron core-gold shell nanoparticles through mitochondria-mediated autophagy, *Biomaterials* 32, 4565-4573 (2011).
- [224] Kayal, Sibnath; Ramanujan, Raju Vijayaraghavan, "Anti-Cancer Drug Loaded Iron-Gold Core-Shell Nanoparticles (Fe@Au) for Magnetic Drug Targeting" *Journal of Nanoscience and Nanotechnology*, 10(9), , 5527-5539 (2010).
- [225] T. Jafari, A. Simchi, N. Khakpash, "Synthesis and cytotoxicity assessment of superparamagnetic iron–gold core–shell nanoparticles coated with polyglycerol" *Journal of Colloid and Interface Science* 345, 64–71 (2010).
- [226] Jin Zhang, Michael Post, Teodor Veres, "Laser-Assisted Synthesis of Superparamagnetic Fe@Au Core-Shell Nanoparticles" *J. Phys. Chem. B*, 110, 7122-7128 (2006).
- [227] Zhihui Ban, Yuri A. Barnakov, Feng Li, "The synthesis of core–shell iron@gold nanoparticles and their characterization" *J. Mater. Chem.*, 15, 4660-4662 (2005).
- [228] Tuan Anh Pham, Nanjundan Ashok Kumar, Yeon Tae Jeong, "Covalent functionalization of graphene oxide with polyglycerol and their use as templates for anchoring magnetic nanoparticles" *Synthetic Metals* 160, 2028–2036 (2010).
- [229] Uğur Tamer, Yusuf Gündoğdu, İsmail Hakkı Boyacı, Kadir Pekmez, "Synthesis of magnetic core–shell Fe<sub>3</sub>O<sub>4</sub>–Au nanoparticle for biomolecule immobilization and detection" *Journal of Nanoparticle Research*, 12(4), 1187-1196 (2010).
- [230] Jianding Qiu, Huaping Peng, Ruping Liang, Xinghua Xia, "Facile preparation of magnetic core-shell Fe<sub>3</sub>O<sub>4</sub>@Au nanoparticle/myoglobin biofilm for direct electrochemistry" *Biosensors and Bioelectronics*, 25(6): 1447-1453 (2010).

- [231] Xi Zhou, Wenlong Xu, Yan Wang, "Fabrication of Cluster/Shell Fe<sub>3</sub>O<sub>4</sub>/Au Nanoparticles and Application in Protein Detection via a SERS Method" *J. Phys. Chem. C*, 114 (46), 19607–19613 (2010).
- [232] Jinfeng Ren, Shun Shen, Zhiqing Pang, "Facile synthesis of superparamagnetic Fe<sub>3</sub>O<sub>4</sub>@Au nanoparticles for photothermal destruction of cancer cells" *Chem. Commun.*, 47, 11692–11694 (2011).
- [233] Wan SR, Huang JS, Guo M, Zhang HK, Cao YJ, Yan HS, Liu KL., "Biocompatible superparamagnetic iron oxide nanoparticle dispersions stabilized with poly (ethylene glycol) oligo (aspartic acid) hybrids" *J Biomed Mater Res A.*;80A:946–954 (2007).
- [234] T. Harada and H. Yoshimura, "Ferritin protein encapsulated photoluminescent rare earth nanoparticle" *Journal of Applied Physics* 114, 044309 (2013).
- [235] Cohen B., Ziv K., Plaks V., Harmelin A. and Neeman M., "Ferritin nanoparticles as magnetic resonance reporter gene" *WIREs Nanomed Nanobiotechnol*, 1: 181–188 (2009).
- [236] D.D. Awschalom, D.P. Di Vincenzo, and J.F. Smyth, "Macroscopic Quantum Effects in Nanometer-Scale Magnets" *Science* 258, 414 (1992).
- [237] Jun-Sung Kim, Tae-Jong Yoon et al., "Cellular uptake of magnetic nanoparticle is mediated through energy-dependent endocytosis in A549 cells" *J. Vet. Sci.*, 7(4), 321–326 (2006).
- [238] Geppert M, Hohnholt MC, Thiel K, Nürnberger S, Grunwald I, Rezwani K, et al., "Uptake of dimercaptosuccinate-coated magnetic iron oxide nanoparticles by cultured brain astrocytes" *Nanotechnology*, 22:145101 (2011).
- [239] Bertorelle F, Wilhelm C, Roger J, Gazeau F, Menager C, Cabuil V., "Fluorescence-modified superparamagnetic nanoparticles: intracellular uptake and use in cellular imaging" *Langmuir*, 22:5385–5391 (2006).
- [240] Bergey EJ, Levy L, Wang XP, Krebs LJ, Lal M, Kim KS, Pakatchi S, Liebow C, Prasad PN., "DC magnetic field induced magnetocytotoxicity of cancer cells targeted by LH-RH magnetic nanoparticles in vitro" *Biomed Microdevices*, 4:293–299 (2002).
- [241] Gupta AK, Gupta M., "Cytotoxicity suppression and cellular uptake enhancement of surface modified magnetic nanoparticles" *Biomaterials*, 26:1565–1573 (2005).
- [242] Mehrmohammadi M, Oh J, Ma L, Yantsen E, Larson T, Mallidi S, Park S, Johnston KP, Sokolov K, Milner T, Emelianov SI., "Imaging of iron oxide nanoparticles using magneto-motive ultrasound" *Proc IEEE Ultrason Symp.*, 652–655 (2007).
- [243] Oldenburg AL, Crecea V, Rinne SA, Boppart SA., "Phase-resolved magnetomotive OCT for imaging nanomolar concentrations of magnetic nanoparticles in tissues" *Opt Express*, 16:11525–11539 (2008).
- [244] Ajay Kumar Gupta et al., "Cytotoxicity suppression and cellular uptake enhancement of surface modified magnetic nanoparticles" *Biomaterials* 26, 1565–1573 (2005).
- [245] Arakaki A., S. Hideshima, T. Osaka, "Detection of biomolecular interaction between biotin and streptavidin on a self-assembled monolayer using magnetic nanoparticles" *Biotechnol. Bioeng.* 88: 543–546 (2004).
- [246] Amemiya, Y., T. Tanaka, T. Matsunaga, "Novel detection system for biomolecules using nano-sized bacterial magnetic particles and magnetic force microscopy" *J. Biotechnol.* 120:308–314 (2005).
- [247] Andriy V. Moskalenko, Polina L. Yarova, Sergey N. Gordeev, "Single Protein Molecule Mapping with

- Magnetic Atomic Force Microscopy" *Biophysical Journal* 98, 478–487 (2010).
- [248] He-bai Shen, De-hong Long et al., "Magnetic force microscopy analysis of apoptosis of HL-60 cells induced by complex of antisense oligonucleotides and magnetic nanoparticles" *Biophysical Chemistry* 122 1–4 (2006).
- [249] Zhang, Y., Yang, M., Ozkan, M. and Ozkan, C. S., "Magnetic force microscopy of iron oxide nanoparticles and their cellular uptake" *Biotechnol Progress*, 25: 923–928 (2009).
- [250] Honarmand Ebrahimi K, Hagedoorn P-L, Jongejan J, Hagen W, "Catalysis of iron core formation in *Pyrococcus furiosus* ferritin" *J Biol Inorg Chem.*, 14: 1265–1274 (2009).
- [251] Laurent S., Forge D., Port M., Roch A., Robic C., Van der Elst L., Muller R N., "Oxide nanoparticles: synthesis, stabilization, vectorialization, physicochemical characterization, and biological applications" *Iron*, M. 108, Chemical Reviews, 2064-110 (2008).
- [252] Martínez-Pérez MJ, de Miguel R, Carbonera C, Martínez-Júlvez M, Lostao A, Piquer C, Gómez-Moreno C, Bartolomé J, Luis F., "Size-dependent properties of magnetoferritin" *Nanotechnology*, 21:465707 (2010).
- [253] San Paulo A, García R., "Tip-surface forces, amplitude, and energy dissipation in amplitude-modulation (tapping mode) force microscopy" *Phys Rev B*, 64:193411 (2001).
- [254] San Paulo A, García R., "Unifying theory of tapping-mode atomic-force microscopy" *Phys Rev B*, 66:041406 (2002).
- [255] Schreiber S, Savla M, Pelekhov DV, Iscru DF, Selcu C, Hammel PC, Agarwal G., "Magnetic force microscopy of superparamagnetic nanoparticles" *Small*, 4:270–278 (2008).
- [256] Kim D, Chung NK, Allen S, Tandler SJB, Park JW., "Ferritin-based new magnetic force microscopic probe detecting 10 nm sized magnetic nanoparticles" *ACS Nano*, 6:241–248 (2012).
- [257] Hsieh CW, Zheng B, Hsieh S., "Ferritin protein imaging and detection by magnetic force microscopy" *Chem Commun.*, 46:1655–1657 (2010).
- [258] Dietz C, Herruzo ET, Lozano JR, Garcia R., "Nanomechanical coupling enables detection and imaging of 5 nm superparamagnetic particles in liquid" *Nanotechnology*, 22:125708 (2011).
- [260] Sievers S, Braun KF, Eberbeck D, Gustafsson S, Olsson E, Schumacher HW, Siegner U., "Quantitative measurement of the magnetic moment of individual magnetic nanoparticles by magnetic force microscopy" *Small*, 8:2675–2679 (2012).
- [261] Simona Picchietti, Anna Maria Fausto, Elisa Randelli, "Early treatment with *Lactobacillus delbrueckii* strain induces an increase in intestinal T-cells and granulocytes and modulates immune-related genes of larval *Dicentrarchus labrax* (L.)" *Fish & Shellfish Immunology* 26, 368–376 (2009).
- [262] Csaba I. Tima, Ákos M. Lőrincz, "Antibacterial effect of microvesicles released from human neutrophilic granulocytes" *Blood*, 121(3):510-518 (2013).
- [263] Yuji Teramura, Yoshihiro Kaneda, Hiroo Iwata, "Islet-encapsulation in ultra-thin layer-by-layer membranes of poly(vinyl alcohol) anchored to poly(ethylene glycol)–lipids in the cell membrane" *Biomaterials* 28, 4818–4825 (2007).
- [264] Schreiber S., M. Savla, G. Agarwal, "Magnetic force microscopy of superparamagnetic nanoparticles" *Small*, 4:270–278 (2008).

- [265] Kaiser, U., A. Schwarz, and R. Wiesendanger, "Magnetic exchange force microscopy with atomic resolution" *Nature*, 446:522–525 (2007).
- [266] Zhong Q, Inniss D, Kjoller K, Elings V., "Fractured polymer/silica fiber surface studied by tapping mode atomic force microscopy" *Surf Sci Lett.*, 290:L688-L692 (1993).
- [267] Shu-wen W Chen, Jean-Luc Pellequer, "DeStripe: frequency-based algorithm for removing stripe noises from AFM images" *BMC Structural Biology*, 11:7 (2011).

# Acknowledgment

I would like to thank to my PhD supervisors, Professors Marco Rossi and Dr. Daniele Passeri, for supporting me during my study. Dr. Passeri is someone you will instantly love and never forget once you meet him. He's the kindest advisor and one of the smartest people I know. He is my primary resource for getting my science questions answered and was instrumental in helping me crank out this thesis, all in one month. I hope that I could be as lively, enthusiastic, energetic and humorous as Daniele and to someday be able to command an audience as well as he can. Prof. Rossi has been supportive and has given me the freedom to pursue various projects without objection. He has also provided insightful discussions about the research. I am also very grateful for his scientific advice and knowledge and many insightful discussions and suggestions. I will also thank our PhD program coordinator, Professor Enzo Marinari, and Professor Massimo Testa, for his help and great attention while I was the graduate student in Sapienza University.

A good support system is important to surviving and staying sane in grad school. I was lucky to be granted the scholarship from Erasmus Mundus project, which assure me to get a good education career in Europe, and this will change my life definitely, whatever my family life and my research direction.

As a part of our group Daniele Passeri, Stella Corsetti, Livia Angeloni, we've all been there for one another and have taught ourselves and each other many tools and issues of microscopies. I know that I could always ask them for advice and opinions on lab related issues. Livia is a wonderful and generous friend who has been through a lot and I admire her positive outlook and her ability to smile despite the situation. I remember first meeting Livia at the beginning of my studying two years ago and we managed to keep in touch during the year that she was working. I'll never forget the many wonderful lunches and fun activities we've done together. In addition to my husband, Daniele was the one who was there for me during the thesis writing hell to help me quickly proof read and give suggestions. I know that when we are old, he will still be there as a supportive and caring friend, his humor is best impressive and will be my direction of my life.

Stella and Melania are someone you won't forget. They care about and will look out for their people. I know



I can count on them to always provide helpful suggestions and help with instrumentation and general lab questions. I will miss our silliness and childish sessions like that time with coffee. I still get a laugh when I reminisce about the time we spent together. They are all a fun bunch with lots of enthusiasm and optimism and remind me of how I used to be when I first got to Sapienza. I haven't gotten a chance to get to really know them since I've been in a hole this past year but they've all been so friendly and personable to me. I wish these younger students the best of luck and hopefully their time in graduate school won't turn them into bitter old farts like me.

I also thank people who were not part of our group but helped me out, including Professor Mario Barteri from Chemistry department, Professor Fabrizio Pantanella (lots of help with samples preparation and information), Fabrizio Pantanella Forte (a wonderful person with great capability who was nice to help me during my first year) here. Each person listed has played some kind of role in my time here. I also thank the wonderful staff in the Chemistry Department as well as in other departments for always being so helpful and friendly. People here are genuinely nice and want to help you out and I'm glad to have interacted with many. If I have forgotten anyone, I apologize.

I especially thank my mom, dad, and sister. I love them so much, and I would not have made it this far without them. My sister as another PhD student has been my best friend all my life and I love her dearly and thank her for all her reasonable advice and support. I know I always have my family to count on when times are rough. Special thanks to the newest additions to my family, Dr. Mizhang Xiao, my husband as well as his wonderful family who all have been supportive and caring. Dr. Xiao is the only person who can appreciate my idea and sense of humor. There are no words to convey how much I love him. Dr. Xiao has been a true and great supporter and has unconditionally loved me during my good and bad times. He has been non-judgmental of me and instrumental in instilling confidence. He has faith in me and my intellect even when I felt like digging hole and crawling into one because I didn't have faith in myself. These past several years have not been an easy ride, both academically and personally. I truly thank Dr. Xiao for sticking by my side, even when I was irritable and depressed. I feel that what we both learned a lot about life and

strengthened our commitment and determination to each other and to live life to the fullest. The last and very sweet thanks will be given to my son, Dongdao Xiao, as a four-year boy, his words, gestures even a sentence from the eyes, give me the biggest strength to go on, you are not only my boy, but also my good friend and teacher, help me to make my life more meaningful.

*I dedicate this thesis to  
my family, my husband, and my beloved son  
for their constant support and unconditional love.  
I love you all dearly.*